THESIS

MICHIGAN STATE UNIVERSITY LIBRARIES
3 1293 00885 7116

This is to certify that the

dissertation entitled

Deformation Behavior and Microstructure of TaC, and Processing of C-TaC Composites

presented by

Chulsoo Kim

has been accepted towards fulfillment
of the requirements for

Ph.D. degree in Materials Science

Major professor

Date February 19, 1991

MSU is an Affirmative Action/Equal Opportunity Institution

O-12771

LIBRARY
Michigan State
University

PLACE IN RETURN BOX to remove this checkout from your record.
TO AVOID FINES return on or before date due.

DATE DUE	DATE DUE	DATE DUE

MSU Is An Affirmative Action/Equal Opportunity Institution
c:\circ\datedue.pm3-p.1

DEFORMATION BEHAVIOR AND MICROSTRUCTURE OF TaC, AND PROCESSING OF C-TaC COMPOSITES

By

Chulsoo Kim

A THESIS

Submitted to

Michigan State University

in partial fulfillment of the requirements

for the degree of

DOCTOR OF PHILOSOPHY

Department of Metallurgy, Mechanics and Materials Science

1991

ABSTRACT

DEFORMATION BEHAVIOR AND MICROSTRUCTURE OF TaC, AND PROCESSING OF C-TaC COMPOSITES

By

Chulsoo Kim

Deformation behavior of $TaC_{0.99}$ at room temperature was studied by means of a combination of microindentation techniques and transmission electron microscopy. Extensive local plastic deformation was observed in the vicinity of microindentations. Plastic deformation of $TaC_{0.99}$ at room temperature was mainly accomplished by the motion of edge dislocations. Long screw dislocations and the wavy character of screw dislocations suggest the existence of a high Peierls stress for screw dislocation motion at room temperature. Annealing of the indentation-deformed $TaC_{0.99}$ results in strongly recovered microstructures and recrystallization, comparable to metals with high stacking fault energy.

Deformation behavior of $TaC_{0.99}$ polycrystals at elevated temperatures was investigated by compressive creep tests. From the results on creep tests at intermediate temperatures (1400 -1500 °C) and

stresses (105 - 170 MPa), the values of the stress exponent (n) and activation energy (Q_c) for power-law creep of $TaC_{0.99}$ were found to be $n \approx 1.8$ and $Q_c \approx 150$ KJ/mol. The low activation energy and the low stress exponent suggest that the creep of $TaC_{0.99}$ at intermediate temperatures is mainly controlled by grain boundary sliding. This is further supported by observation of void formation. The observation of dislocation interaction in the crystal interior suggests that dislocation glide may act as a minor contributing mechanism during creep. TEM investigation also revealed the formation of subboundaries and dislocation networks. Most dislocations formed during creep of $TaC_{0.99}$ have no preferential orientation, in contrast to dislocations formed at low temperatures.

The fabrication of C-fiber reinforced TaC composites was studied using combinations of powder metallurgy techniques such as cold pressing, slurry infiltration, sintering, and hot isostatic pressing (HIP). The characteristics of the interface between carbon fibers and TaC were investigated by optical microscopy, scanning electron microscopy and auger electron spectroscopy. No chemical reaction occurred at the interface between carbon fibers and a stoichiometric TaC matrix. Carbon fibers suffered damage by indentation from tantalum carbide particles during cold compaction and HIP. A tantalum carbide coating of C-fibers prevented this indentation damage.

ACKNOWLEDGEMENTS

I would like to thank my parents and other members of my family for their love, patience and continuous support. Also, I wish to thank Professor Günter Gottstein under whose direction this research was performed, for his thoughtful guidance, inspiration and support over the entire course of my graduate studies. Additionally, special thanks to Professor David Grummon whose scientific interest in my research provided a generous amount of support and encouragement. Many thanks are extended to the other members of my guidance committee: Dr. Iwona Jasiuk and Dr. Jack Bass for their valuable comments given on my thesis. Thanks are also given to Dr. Martin Crimp for helpful discussions concerning the transmission electron microscopic studies.

Without the help of technical expertise, my research would not have been successfully completed. Therefore, I wish to express my sincere appreciation to Dr. Karen Klomparens, Dr. Stanley Flegler and Mr. Vivion Shull of the Center for Electron Optics for generously allowing me to use their facilities. Also, thanks go to Mr. Tom Palazzolo and other members of the Physics Machine Shop for their help and friendship. I appreciate Dr. Ibrahim Sekercioglu at Howmet Turbine Component Corporation for his valuable comments and help in using the company's facilities. Thanks are given to Mr. Richard Schalek and Mr. Karl Tebeau for proofing drafts of my thesis. Finally, I would like to acknowledge the financial support received from the Composite Materials and Structures Center at Michigan State University for studying the processing of C-TaC composites.

TABLE OF CONTENTS

Page

LIST OF TABLES ---------- vii

LIST OF FIGURES ---------- viii

CHAPTER

1. INTRODUCTION ---------- 1

2. LITERATURE REVIEW ---------- 5
2.1 PHYSICAL PROPERTIES OF TaC ---------- 5
2.2 MECHANICAL PROPERTIES OF TRANSITION METAL MONOCARBIDES ---------- 10
2.2.1 Microhardness ---------- 10
2.2.2 Mechanical behavior of group IV carbides ---------- 14
2.2.3 Mechanical behavior of group V carbides ---------- 20
2.3 FUNDAMENTALS OF CREEP IN CRYSTALLINE SOLIDS ---------- 24
2.3.1 Creep curves ---------- 24
2.3.2 Steady-state creep ---------- 27
2.3.3 Mechanisms of creep ---------- 29

3. ROOM TEMPERATURE DEFORMATION & ANNEALING OF TaC ---------- 35
3.1 INTRODUCTION ---------- 35
3.2 EXPERIMENTAL PROCEDURE ---------- 38
3.2.1 Processing and characterization of tantalum carbide specimens ---------- 38
3.2.2 Indentation deformation and TEM specimen preparation ---------- 41
3.3 EXPERIMENTAL RESULTS ---------- 45
3.4 DISCUSSION ---------- 64
3.5 SUMMARY ---------- 73

4. INTERMEDIATE-TEMPERATURE CREEP OF TaC ---------- 74
4.1 INTRODUCTION ---------- 74
4.2 EXPERIMENTAL PROCEDURE ---------- 79
4.2.1 Creep specimen preparation ---------- 79

4.2.2 Creep test apparatus ---------- 80
4.2.3 Creep tests ---------- 82
4.3 EXPERIMENTAL RESULTS ---------- 86
4.4 DISCUSSION ---------- 110
4.5 SUMMARY ---------- 115

5. PROCESSING OF C-TaC COMPOSITES ---------- 116
5.1 INTRODUCTION ---------- 116
5.2 EXPERIMENTAL PROCEDURE ---------- 123
5.2.1 Characteristics of starting materials ---------- 123
5.2.2 Fabrication of C-TaC composites ---------- 126
5.3 EXPERIMENTAL RESULTS ---------- 138
5.4 DISCUSSION ---------- 153
5.5 SUMMARY ---------- 156

6. SUMMARY AND CONCLUSIONS ---------- 157

LIST OF REFERENCES ---------- 160

LIST OF TABLES

Table

Page

1. Slip planes in the transition metal carbides. (From Ref. [30]). ---------- 13
2. The chemical composition of as-received TaC specimen. ---------- 39
3. Some characteristics of TaC specimens. ---------- 39
4. Dislocation contrast of single set of dislocations. ---------- 51
5. Dislocation contrast of two sets of dislocations. ---------- 53
6. Dislocation contrast of dislocations in hexagonal networks. ---------- 61
7. Quasi steady-state creep rate data of $TaC_{0.99}$ polycrystals. ---------- 90
8. Dislocation contrast of individual dislocations. ---------- 101
9. Dislocation contrast of dislocations in hexagonal networks. ---------- 104
10. Dislocation contrast of dislocations in networks. ---------- 108
11. Characteristics of as-received TaC powder and C-fiber. ---------- 124

LIST OF FIGURES

Figure Page

1. Phase diagram of the Ta-TaC system (From Ref.[2]). ---------- 7
2. Variation of the effective resolved shear stress on (001) surface with {110}<1$\bar{1}$0> and {111}<1$\bar{1}$0> slip (From Ref. [30]). ---------- 13
3. Schematic diagram of the {111} plane in cubic carbides showing possible slip path (From Ref. [30]). ---------- 15
4. Schematic drawing of typical creep curve observed under a constant tensile stress (From Ref. [52]). ---------- 25
5. Optical micrographs of as-received and HIP processed $TaC_{0.99}$ specimen: (a), (b); as-received specimen, (c), (d); HIP processed specimen. ---------- 46
6. Transmission electron micrographs of undeformed $TaC_{0.99}$ specimen: (a) Near grain boundary region, (b) Triple grain boundary point. ---------- 47
7. Transmission electron micrographs and the diffraction pattern of indentation deformed $TaC_{0.99}$ specimen: (a) Dislocation structures near the indentation, (b) Selective area diffraction pattern corresponding to $[111]_{B1}$ zone, (c) Low magnification image of the indented TEM foil. ---------- 49
8. Burgers vector analysis of single set of dislocations: B; beam direction, g; diffraction vector. ---------- 50
9. Transmission electron micrograph of two sets of dislocations. ---------- 52
10. Burgers vector analysis of dislocations of type1 and 2: B; beam direction,

11. Tra

(a).

an

12. Tra

rec

13. Tr

he

14. Tr

ce

15. Bu

16. Tr

(a

(c

(b

B

17. Sc

18. Sc

fr

e

19. A

2

6

9

20. C

a

Page

11. Transmission electron micrographs of the indented and annealed $TaC_{0.99}$:
(a), (b); High and low magnification images near the indentation area of
an annealed specimen. ---------- 55

12. Transmission electron micrograph showing the region near the
recrystallized grain. ---------- 57

13. Transmission electron micrograph showing the subboundaries and
hexagonal networks. ---------- 58

14. Transmission electron micrograph showing some of subgrains and
cell structure. ---------- 59

15. Burgers vector analysis of the hexagonal networks. ---------- 60

16. The Kikuchi pattern analysis of the misorientation angle between two subgrains:
(a), (d); bright field images of two subgrains labeled 1 and 2.
(c), (f) and (h); the corresponding Kikuchi patterns of subgrain 1.
(b), (e) and (g); the corresponding Kikuchi patterns of subgrain 2.
B; beam direction. ---------- 62

17. Schematic of the slip configuration near the indenter. ---------- 67

18. Schematic of the possible formation of long screw dislocation segments
from the dislocation half-loop: (a) initial stage, (b) after glide,
e; edge dislocation, s; screw dislocation, **b**; Burgers vector. ---------- 69

19. A schematic drawing of specimen set-up for creep tests: 1.TZM push rod,
2. W-pin, 3. Al_2O_3 platen, 4.TZM compression block, 5. SiC platen,
6. $TaC_{0.99}$ specimen, 7. Thermocouple, 8. Al_2O_3 extension rod,
9. Extensometer. ---------- 83

20. Creep curve of $TaC_{0.99}$ obtained under the conditions of 105 MPa
and 1400 °C. ---------- 87

Page

21. Creep curves of $TaC_{0.99}$ under the conditions of 105 MPa and 170 MPa at 1500 °C: ●; 105 MPa, ▲; 170 MPa. ---------- 88

22. Strain rate as a function of strain: ■; 105 MPa/1400 °C, ●; 105 MPa/1500 °C, ▲; 170 MPa/1500 °C. ---------- 89

23. TEM micrograph of $TaC_{0.99}$ crept at 1300 °C and 300 MPa. ---------- 92

24. Optical micrographs of $TaC_{0.99}$ crept at 1500 °C and 60 MPa: (a) low magnification image, (b) high magnification image. ---------- 93

25. TEM micrograph of $TaC_{0.99}$ crept at 1500 °C and 60 MPa: B; beam direction, g; diffraction vector. ---------- 95

26. High magnification micrograph of the subboundary shown in Figure 25: B; beam direction, g; diffraction vector. ---------- 96

27. TEM micrograph of crept $TaC_{0.99}$ showing a subboundary and individual dislocations: B; beam direction, g; diffraction vector. ---------- 97

28. High magnification micrograph of the subboundary shown in Figure 27. ---------- 98

29. TEM micrograph of crept $TaC_{0.99}$ showing a twist boundary: B; beam direction, g; diffraction vector. ---------- 99

30. High magnification micrograph of the twist boundary shown in Figure 29: B; beam direction, g; diffraction vector. ---------- 100

31. TEM micrograph of crept $TaC_{0.99}$ showing individual dislocations: B; beam direction, g; diffraction vector. ---------- 102

32. Burgers vector analysis of dislocations of type 1,2 and 3: B; beam direction, g; diffraction vector. ---------- 103

33. TEM micrographs of crept $TaC_{0.99}$: (a) a subboundary and hexagonal networks, (b) higher magnification image of the subboundary. B; beam direction, g; diffraction vector. ---------- 105

34.

35.

36.

37.

38

39

40

41

42

45

44

45

B; beam direction, g; diffraction vector. ---------- 105

Page

34. Burgers vector analysis of the hexagonal networks:

B; beam direction, g; diffraction vector. ---------- 106

35. Burgers vector analysis of the dislocation networks:

B; beam direction, g; diffraction vector. ---------- 107

36. TEM micrograph of crept $TaC_{0.99}$ showing a subboundary

and a grain boundary. ---------- 109

37. Scanning electron micrographs of as-received TaC powders and

carbon fibers: (a) Type A powder, (b) APOLLO™ 55 fiber,

(c)Type B powder, (d) AS-4 fiber. ---------- 125

38. The block diagrams of two C-TaC composite processing routes. ---------- 127

39. Photographs of Ta HIP containers: (a) some parts of a HIP container

(a Ta can, top lid, top and bottom spacer), (b) a vacuum-sealed container

before HIP, (c) HIP processed containers (left; a properly processed

container, right; a leaked container). ---------- 129

40. Time, temperature, and pressure profiles of HIP process. ---------- 131

41. Schematic of slurry infiltration process. ---------- 133

42. Photographs of niobium HIP containers: (a), (b) a side and front view

of a Nb container before HIP, (c), (d) a side and front view

of a Nb container after HIP respectively. ---------- 135

43. Optical and SEM micrographs of C-TaC composite:

(a), (b) optical and SEM micrographs showing the matrix(M), interface(I)

and fiber(F) region, (c) a SEM micrograph of damaged carbon fibers. ---------- 139

44. Auger electron spectroscopic survey of C-TaC composite. ---------- 140

45. Tantalum line scans across the interface of C-TaC composite:

Page

46. SEM micrographs of damaged C-fibers during cold compaction. ---------- 143

47. SEM micrographs of slurry infiltrated carbon fibers:

(a) perpendicular to the fibers, (b), (c) parallel to the fibers. ---------- 144

48. SEM micrographs of C-TaC composites produced by the processing route #2:

(a) transverse direction to the fibers, (b) longitudinal direction to the fibers. ------ 145

49. High magnification SEM micrographs of the specimen in Figure 12:

(a) transverse direction to the fibers, (b) longitudinal direction to the fibers. ------ 146

50. The SEM micrographs of the sintered and fractured pre-preg composite tape. ---- 148

51. The SEM micrographs of a coated carbon fiber:

(a) transverse direction to the fiber, (b) longitudinal direction to the fiber. -------- 149

52. Ta and C line scans of the coated carbon fiber:

(a) Ta and C line scan, (b) Ta line scan. ---------- 150

53. The SEM micrographs and a Ta line scan of sintered C-TaC composite

after coating the fiber. ---------- 152

CHAPTER 1

INTRODUCTION

The monocarbides of the group IV and V transition metal such as TiC, ZrC, HfC, VC, NbC and TaC have B1 structure in which carbon atoms are occupying the octahedral interstitial sites of the face centered cubic (FCC) metal lattice. These materials belong to the group of Hägg compounds and are also named as cubic carbides due to their cubic crystal structure. Transition metal monocarbides (TMMC) exhibit a combination of properties of three primary types of bonding in solids. For example, their crystal structure is ionic NaCl type, their electrical and magnetic properties are metallic, and their high elastic modulus and high melting point are associated with covalent bonding.

One interesting property of TMMC is that these materials exist over a wide range of stoichiometry due to structural vacancies on carbon atom sites. The chemical formula of TMMC is often written as MC_x where M represents transition metal species and x represents carbon-to-metal ratio. In the transition metal monocarbides, the ideal stoichiometry is generally not found and deviations from stoichiometric composition are far more common. It has been reported that a vacancy concentration of up to 50% can exist on carbon lattice sites and that the vacancies tend to exhibit ordering when their concentration is high. It has been found that all types of properties e.g. mechanical, thermal, electrical, magnetic etc.

dep

"ce

of

par

fol

Hc

dif

th

me

re

re

ch

ac

av

th

T

us

m

it

o

depend significantly upon the carbon-to-metal ratio and ordering [1].

In commercial applications, these carbides are used extensively in "cemented carbides" cutting tools, wear-resistant parts and dies because of their great hardness. In addition to these applications, TMMC are of particular interest for high-temperature structural applications for the following reasons:

i) TMMC include materials with the highest melting points.

ii) TMMC are mechanically extremely strong.

iii) Above the brittle-to-ductile transition temperature, TMMC can be plastically deformed similar to ductile fcc metals.

However, their high notch-sensitivity, poor oxidation resistance, difficulty of fabrication and lack of reliable property data have limited their full acceptance. A number of books and review articles on transition metal monocarbides have been published [1-5]. The results of early research on the mechanical properties of TMMC were proved to be less reliable due to the fact that samples used usually lacked proper characterization. As high-temperature technologies advance, more accurate properties of well-characterized carbide samples are becoming available.

Among transition metal monocarbides, titanium carbide has been the most frequently selected for investigation of deformation behavior. This is probably due to its high strength-to-density ratio and its wide usage in cemented carbides. The other Group IV and Group V transition metal carbides have been less frequently studied in different degrees. So it seems to be necessary to study their mechanical behaviors in detail in order to fully understand and utilize these interesting materials.

A

polycry

the foll

i)

ii

iii

T

tantalu

below:

I

anneal

microi

(TEM)

disloc

microi

disloc

i.e. at

invest

mecha

deforr

studie

was s

and T

Among the various TMMC, stoichiometric tantalum carbide polycrystals have been chosen for the current investigation because of the following reasons:

i) TaC has the highest melting point among all solid materials.

ii) TaC is more metallic in nature than the other transition metal carbides.

iii) TaC has good potential for low temperature ductility.

The current work consists of three related topics on stoichiometric tantalum carbide. The characteristics of each topic can be described as below:

First, room temperature deformation and high temperature annealing behavior of TaC were studied by means of a combination of microindentation techniques and transmission electron microscopy (TEM). The main aim of this study is to investigate details of the dislocation structure and the deformation process resulting from the microindentation at room temperature, and also the changes in dislocation structure after annealing.

Second, the creep behavior of TaC at intermediate temperatures, i.e. at temperatures below 0.5 T_m, where T_m is the melting point, was investigated in order to obtain information about its elevated temperature mechanical properties, in particular the mechanisms and kinetics of creep deformation. The microstructure development during creep tests was also studied by TEM.

Third, the processing of carbon fiber reinforced TaC composites was studied. The characteristics of the interface between carbon fibers and TaC were investigated by optical microscopy, scanning electron

micros

the pro

the pro

previo

tantal

fundar

three

these

experi

of the

obtair

nicroscopy (SEM) and auger electron spectroscopy (AES). In particular, he problems encountered during processing and the possible solutions of he problems were addressed.

The following chapter presents a literature survey of relevant ›revious research on TMMC which include: (a) physical properties of antalum carbide, (b) mechanical properties of TMMC and (c) 'undamentals of creep in crystalline solids. The experimental studies on hree aforementioned topics are presented in separate chapters. Each of hese chapters is composed of sections which include introduction, :xperimental procedure, experimental results, discussion and a summary ›f the chapter. The final chapter consists of the summary and conclusions ›btained from the current study.

2.1 PE

carbo

transi

high

struct

octah

found

antity

struc

the o

TaC

atom

octah

carbi

gene

ratio

from

CHAPTER 2

LITERATURE REVIEW

2.1 PHYSICAL PROPERTIES OF TANTALUM CARBIDE

Tantalum, a BCC transition metal, forms two compounds with carbon: Ta_2C and TaC. Ta_2C has two allotropic phases with an $\alpha-\beta$ transition at about 2180 °C. The crystal structure of $\beta-Ta_2C$, the stable high temperature form of Ta_2C, belongs to the hexagonal L_3' type structure, with carbon atoms statistically distributed in one-half of the octahedral sites. Bowman et. al. [6], after a neutron diffraction study, found that the crystal structure of α-Ta_2C is a C6 cadmium iodide antitype structure, due to ordering of the carbon atoms.

TaC, a monocarbide phase, crystallizes in the B1(NaCl-type) structure. Ta atoms occupy the FCC sublattice, while the C atoms occupy the octahedral interstitial sites. The stacking sequence of {111} planes of TaC can be designated as $A\gamma B\alpha C\beta A\gamma B\alpha C\beta A\gamma$, where A B C represent Ta atoms and α β γ represent the carbon atoms in the corresponding octahedral sites. Like the other transition metal monocarbides, tantalum carbide has a wide range of carbon deficient compositions and is generally represented as TaC_x, where x is the carbon-to-tantalum atomic ratio. Typically, the values of x for tantalum monocarbide phase range from 0.74 to 0.99. The melting point goes through a maximum at about

3983 °C for the $TaC_{\sim 0.89}$ composition. A phase diagram of the Ta-TaC system [2] is shown in Figure1.

For lower carbon content the existence of an additional phase, the so called zeta(ζ)-phase, has been reported [7,8]. The composition of the ζ-phase is known to be close to $TaC_{0.75}$. Yvon and Parthe [9] have investigated the crystal structure of the ζ-phase in VC, NbC and TaC, and have proposed that the metal atoms in the ζ-phase arrange in the trigonal structure consisting of 12 close packed metal atom layers with a stacking sequence of ABABCACABCBC. The exact arrangement of carbon atoms between the metal layers was not determined in their X-ray work. Rowcliffe and Thomas [10], using electron microscopy and electron diffraction, have suggested that the ζ-phase of TaC is formed by the removal of C atoms in every fourth C layer, followed by shearing of the overlying Ta layer. The stacking sequence of the ζ-phase was given as $A\gamma B\overset{\alpha}{\uparrow}A\gamma B\alpha C\beta A\overset{\gamma}{\uparrow}C\beta A\gamma B\alpha C\overset{\beta}{\uparrow}B\gamma C\alpha$, where arrows indicate the complete absence of carbon atoms in the corresponding planes. Thus, the ζ-phase was considered as a stacking fault with a composition of an ordered Ta_4C_3 phase. Recently, Markhasev et al. [11] have proposed that the formation of the ordered Ta_4C_3 phase (ζ-phase) occurs by a diffusionless slip mechanism, and is promoted by the compressive stress. However, no microstructural evidence has been reported to support the fact that the ζ-phase is an ordered phase.

In the case of the substoichiometric VC and NbC, which belong to the Group V transition metal carbides, the existence of long range ordering has been established and the ordered phases found were V_8C_7, V_6C_5 and Nb_6C_5 [12]. In contrast to those carbides, the same type of

4000

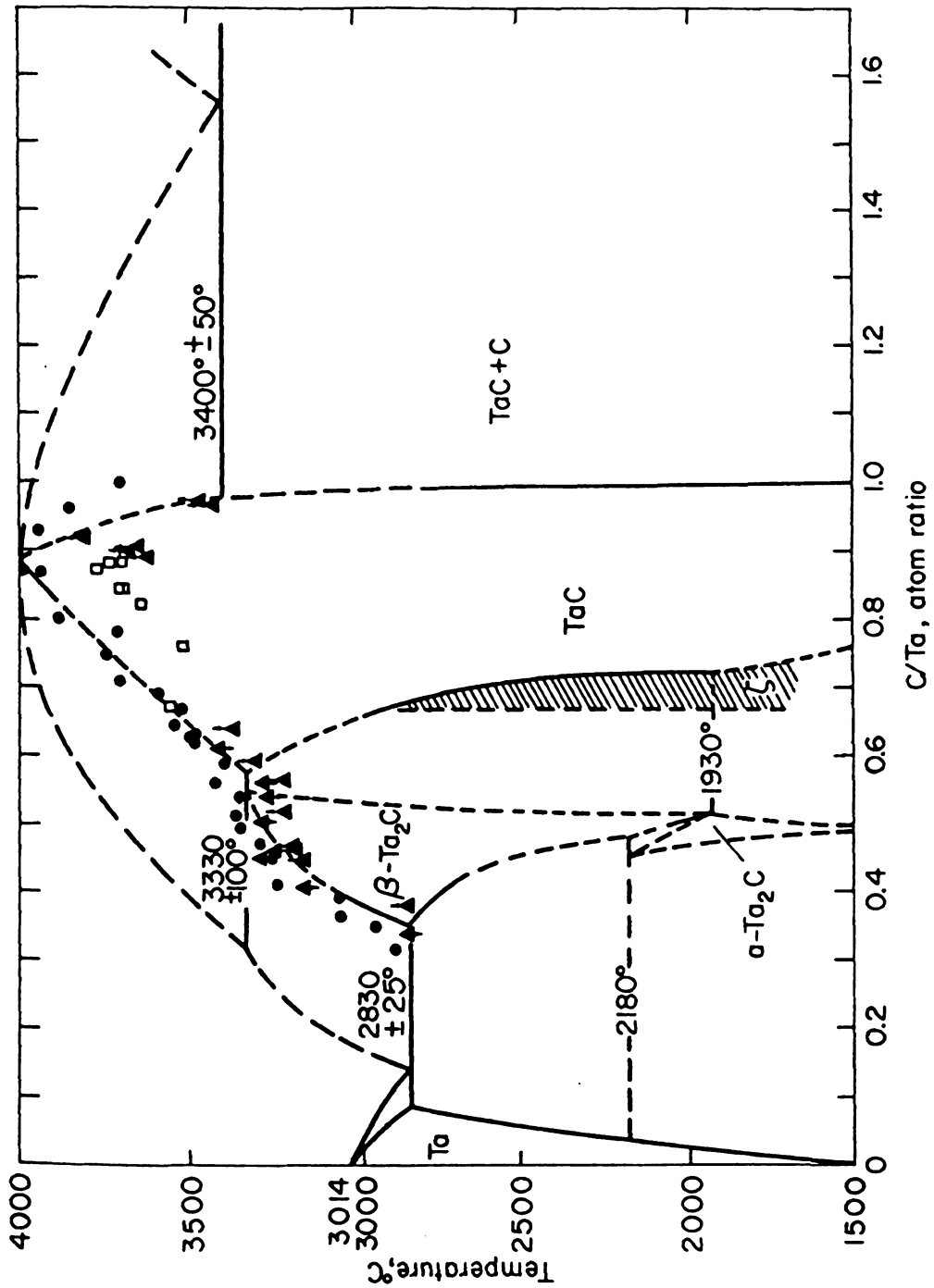

Figure 1. Phase diagram of the Ta-TaC system (From Ref.[2]).

ordering has not been reported for tantalum carbide. The electron diffraction pattern of single crystal $TaC_{0.83}$, which was slowly cooled through the order-disorder temperature, revealed the presence of diffuse bands, rather than discrete superlattice spots [13]. It was suggested that the ordering in tantalum carbide is very imperfect. Similar diffuse band of the electron diffraction pattern have been also observed in other compositions of tantalum monocarbide [10]. Venables and Meyerhoff [13] have concluded that the order-disorder temperature for TaC is lower than those of VC and NbC, and that the long range order in $TaC_{0.83}$ is difficult to develop due to the extremely low carbon diffusivity in that temperature range. De Novion and Maurice [12] have reported that short-range ordering is typical in $TaC_{0.78}$ - $TaC_{0.85}$.

Most of the physical properties of tantalum carbide have been found to depend on the carbon-to-tantalum atomic ratio. Bowman [14] first reported that the lattice parameter of TaC decreases linearly with decreasing composition. Later, Storm [2] analyzed the additional data based on well-characterized material and obtained the following equation:

$$a_o = 4.2908 + 0.1673\ x \qquad (1)$$

where a_o is the lattice parameter of tantalum carbide and x= C/Ta($\pm$ 0.01). The reported values of lattice parameter and the density of $TaC_{0.99}$ are about 4.456 Å and 14.48 g/cm^3, respectively. A change in color of TaC occurs as a function of composition. At low carbon concentrations below about $TaC_{0.8}$, the color is a metallic gray, changing to a bright golden color near the stoichiometric composition.

The electrical resistivity of TaC was found to increase with carbon deficiency [15-17]. Cooper and Hansler [16] reported a linear relationship between resistivity and the C/Ta ratio. This was attributed to the fact that the carbon vacancies act as scattering centers for electrons. Steinz and Resnick [17] measured the value of specific resistivity of stoichiometric TaC as about 24 $\mu\Omega\cdot$cm at room temperature and reported that the temperature coefficient of resistivity decreases rapidly with decreasing carbon content. The magnetic susceptibility of TaC also varies with the composition. The magnetic property of TaC changes from paramagnetic to diamagnetic in the range of $TaC_{0.9}$ - $TaC_{0.97}$ [15, 17]

The coefficient of thermal expansion and the thermal conductivity of $TaC_{0.99}$ at room temperature were reported as 6.3 $\times 10^{-6}$/°C and 0.053 cal/cm·sec·°C, respectively [1]. The elastic properties of TaC at room temperature were determined by Brown et al. [18]. The Young's modulus, shear modulus and Poisson's ratio of $TaC_{0.99}$ were about 537 GPa, 216 GPa and 0.24, respectively.

2.2 MI

2.2.1

micr

temp

kg/r

The

tem

exp

for

sug

ter

sh

qu

lo

oc

o

th

a

r

2.2 MECHANICAL PROPERTIES OF TRANSITION METAL CARBIDES

2.2.1 Microhardness

Westbrook [19] performed extensive measurements on the microhardness of the polycrystalline carbides as a function of temperature. At room temperature, TiC is the hardest carbide ($H_v \approx 3200$ kg/mm^2), but it rapidly loses its hardness with increasing temperature. The hardness of TaC is the lowest ($H_v \approx 1800$ kg/mm^2) at room temperature among the group IV and V transition metal carbides. An exponential relationship between hardness and temperature was proposed for TiC [20,21]. An Arrhenius plot showed two straight line segments, suggesting that a process with higher activation energy dominates at high temperature. This is in qualitative agreement with the critical resolved shear stress of TiC single crystals in compression [22]. However, quantitative agreement could not be found. The predicted slopes were too low and the deflection point in the slope of the experimental curve occurred at a rather low homologous temperature. It was suspected that other processes or mechanisms were operative in the case of the carbides than in the case for pure metals.

A number of researchers have shown that the hardness of TMMC is a sensitive function of stoichiometry, as well as temperature. It was reported that hardness values depend on stoichiometry in the opposite

way

stoic

rapi

a co

stre

situ

com

caus

gro

carl

pro

ban

abo

ele

bar

inc

fro

bar

inc

ha

be

co

th

ca

way for TiC and TaC [4, 23]. In TiC_{1-x}, the hardness increases sharply as stoichiometry is approached. In TaC_{1-x}, however, the hardness increased rapidly with deviation from stoichiometry. Maximum hardness occurs at a composition of $TaC_{0.83}$ [15, 24]. Santoro [15] further found that strength and hardness vary in opposite direction with composition. This situation casts doubt on some of the experimental results. The analysis is complicated by the occurrence of ordered phases in the group V carbides causing an increase of hardness.

Two possible explanations of this contrasting behavior between group IV and V carbides were suggested, using atomic bonding in carbides and a hard sphere model [1, 25]. Carbide formation results in a pronounced separation of the bonding and antibonding parts of the d band. The bonding portion of the resultant band structure is filled with about 8-8.5 valence electrons. Deviation from stoichiometry in TiC (8 electrons) results in a depletion of electrons in the bonding portion of the band and hence lower bond strength. Thus the hardness decreases with increasing deviation from stoichiometry. In TaC(9 electrons), deviation from stoichiometry deplete electrons from the antibonding portion of the band and the average bond strength increases. Thus the hardness increases with decreasing carbon content.

Another explanation of the composition dependence of hardness has been attempted by using a hard sphere model which distinguishes between the nearly stoichiometric carbides of group IV and V. A comparison of lattice parameters for parent metal and carbide suggests that group IV carbides are more ideally close-packed, whereas group V carbides are more open structures. Hence it is argued that the greater

duct

carb

for t

in la

IV b

shou

latti

harc

harc

ope

she

(10

sim

is a

is r

sin

ove

ani

of

Ro

on

lov

tha

be

ductility and preferred {111}<1$\bar{1}$0> slip of nearly stoichiometric group V carbides arises from easier dissociation of dislocations in this slip system for the more open structure. With decreasing carbon content a decrease in lattice parameter indicates a tendency to the more close-packed group IV behavior. For the group IV carbides, any deviation from stoichiometry should not change the arrangement of atoms significantly, since the lattice is already close-packed. At low carbon contents, a reduction in hardness would be expected as a result of the change in Peierls stress.

In 1971, Brookes and coworkers [26] improved existing analyses of hardness anisotropy and showed that it can be used to determine operative slip systems. Figure2 shows the change in effective resolved shear stress with indenter direction for knoop impressions made on the (100) face. The shape of the anisotropy curve for (100)<1$\bar{1}$0> slip is similar to that for (111)<1$\bar{1}$0> slip. They further showed that the hardness is at a maximum when the effective resolved shear stress on the slip plane is minimized. Since then, a number of Knoop hardness measurements on single crystals of carbides have been made to find out the slip systems over a range of temperature [25, 27-29]. By incorporating the hardness anisotropy measurements with the results of etch-pitting and TEM, most of the slip systems could be found and these were summarized by Rowcliffe [30] (Table 1). It is seen that the choice of slip system depends on carbon deficiency and temperature.

Hannink et al. [27] suggested that the preference for (110) slip at low temperatures is a result of strong, directional carbon to metal bonds that prohibit slip on {111}. As the temperature is raised, these bonds become less directional as electrons pass into metallic states, and slip

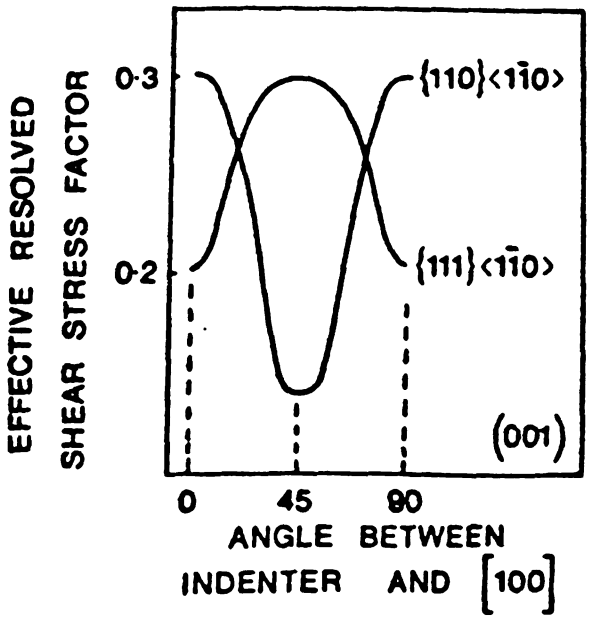

Figure 2. Variation of the effective resolved shear stress on (001) surface with {110}<1$\bar{1}$0> and {111}<1$\bar{1}$0> slip (From Ref. [30]).

Table 1. Slip planes in the transition metal carbides (From Ref. [30]).

Carbide	Room temperature	High temperature
TiC	110	111
ZrC	110	111, 110, 100
HfC	110	Not known
$VC_{0.84}$	110, 111	111
$NbC_{0.83-0.96}$	110, 111	111
$TaC_{0.96}$	111	111, 110
$TaC_{0.83}$	110	111

becor

impli

[25].

[111

stoic

mon

defo

mot

met

2.2.

latt

me

the

of

[1

of

di

di

di

w

B

sc

becomes more similar to fcc metals, namely {111}<1$\bar{1}$0>. Similar implications are made in simple hard sphere models as explained earlier [25]. However, nearly stoichiometric TaC was found to deform by {111}<1$\bar{1}$0> slip even at room temperature. It was also reported that stoichiometric TaC is considerably softer than most of the other monocarbides of group IV and V transition metals [24, 28], and that TaC deforms plastically before it cracks, and cracks arise from dislocation motion. Based on these findings, it was suggested that TaC is more metallic in nature than other carbides [28].

2.2.2 Mechanical behavior of group IV carbides

In early work on single crystal TiC, Williams [22] suggests that lattice resistance to dislocation motion controls yielding in transition metal carbides. It was suggested that the high Peierls stress resulted from the occupation of the octahedral sites by carbon atoms in fcc sublattices of TiC. In 1966, Kelly and Rowcliffe [31] proposed a model for slip on {111} planes along <1$\bar{1}$0> in TiC that takes into account the difficulties of moving dislocations in this structure. Figure 3 shows a schematic diagram of the {111} slip plane in cubic carbides and the <1$\bar{1}$0> slip directions such as B_1B_2, B_2B_3 etc. It is unlikely that slip will proceed directly in $B_1 \rightarrow B_2$, $B_2 \rightarrow B_3$ etc., since the {111} plane will be forced widely apart. Instead a dislocation can dissociate as shown here, that is $B_1B_3 \rightarrow B_1C + CB_3$ and each of the Shockely partials splits according to the scheme shown in this figure. The consequence of this model is that high

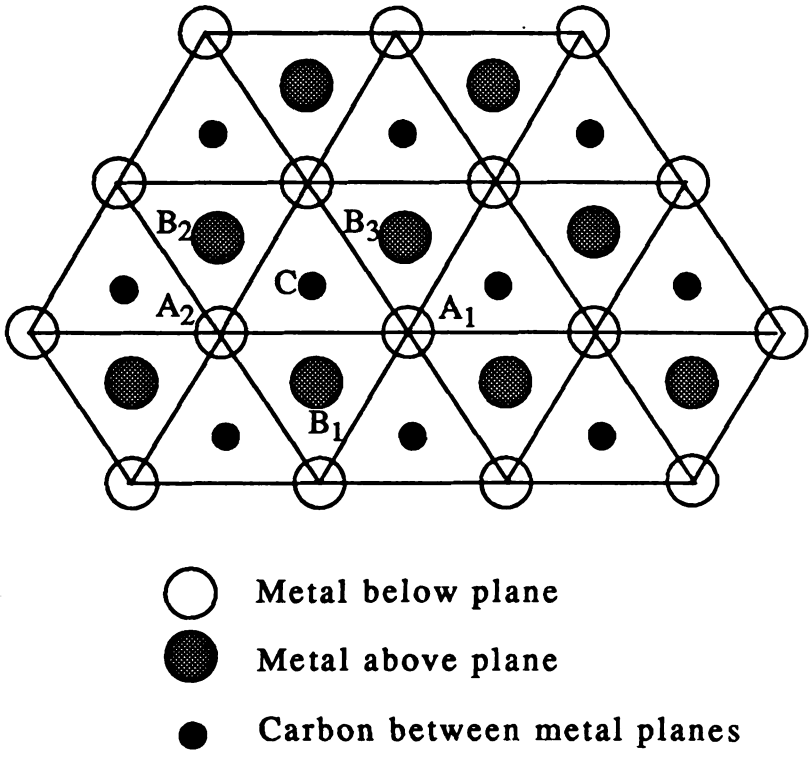

$B_1B_3 \rightarrow B_1C + CB_3$ ($a/2[1\bar{1}0] \rightarrow a/6[2\bar{1}\bar{1}] + a/6[1\bar{2}1]$)

$B_1C \rightarrow B_1A_1 + A_1C$ ($a/6[2\bar{1}\bar{1}] \rightarrow a/6[1\bar{2}1] + a/6[11\bar{2}]$)

Figure 3. Schematic diagram of the {111} plane in cubic carbides showing possible slip path (Adapted from Ref. [30]).

temp
disl
from
[32-
and
disl
resp
carb

ran
pit
{11
cor
car
she
cor

de
Ho
sli
ty
ob
of
is
de
in

temperature deformation will be governed by carbon diffusion near the dislocations. Evidence in support of this mechanism has been obtained from a number of studies in which strain rate sensitivity was measured [32-36]. TEM observations of the dissociation of dislocations in TaC [47] and TiC [37] were reported. The dissociation widths of partial dislocations in TiC and TaC were about 2.5 nm and 2.7-5.2 nm, respectively. From these values, the stacking fault energies for both carbides were calculated to be about 170 mJ/m^2.

Single crystals of TiC were deformed in bending over a temperature range of 800 °C - 2200 °C by Williams and Schaal [38]. Dislocation etch-pit studies on {100} cleavage surfaces revealed that slip occurred on $\{111\}\langle 1\bar{1}0\rangle$ systems. Williams [22] subsequently conducted uniaxial compression tests on single crystals of TiC, ZrC and NbC with various carbon contents in the temperature range 800 °C- 1600 °C. The critical shear stress was found to decrease exponentially with increasing carbon content. No yield point was observed in the stress-strain curve.

Electron microscopy of single crystals of TiC_x (x=0.88 and 0.97) deformed in compression between 900 °C and 1200 °C was conducted by Hollox and Smallman [39]. They confirmed the activation of $\{111\}\langle 1\bar{1}0\rangle$ slip as proposed earlier by Williams et al. [38]. Dislocation structures typical of FCC metals with high stacking fault energy were observed. The observation of elongated dislocation loops and dipoles in the early stage of deformation and of cell structures in more heavily deformed samples is also consistent with the ease of cross slip. Annealing of plastically deformed TiC is accompanied by coalescence of vacancy loops. The initial stages appear to be associated with the formation of trails of small

loops. The final stages involve the formation of a hexagonal network of dislocations. Changes in carbon content did not appear to have any influence on dislocation structures in TiC, but annealing kinetics were changed.

Chatterjee et al. [40] have reaffirmed the TEM results of Hollox and Smallman in TiC single crystals deformed in compression. They found that around 600 °C, a gradual transition from $\{110\}\langle 1\bar{1}0\rangle$ slip to $\{111\}\langle 1\bar{1}0\rangle$ slip occurs and around this temperature both slip systems are operative. This was interpreted to be the governing mechanism of brittle to ductile transition in TiC. Recently, Kurishita et al. [32] have observed yield drops or work softening phenomena in single crystals of $TiC_{0.95}$ deformed in compression from 1007 °C to 2000 °C. A mechanical equation of state at yielding was proposed as:

$$\dot{\gamma} = A\left(\frac{\tau_c}{\mu}\right)^m exp\left(-\frac{Q}{RT}\right) \qquad (2)$$

where $\dot{\gamma}$ is the shear strain rate, A is a constant, τ_c is the critical resolved shear stress, μ is the shear modulus, m is the stress exponent, Q is the activation energy, R is the gas constant and T is the absolute temperature. The values of stress exponents as well as activation energies are quite different below and above the transition temperature around 1377 °C. The deformation rate was considered to be determined by the Peierls mechanism below the transition temperature and by carbon diffusion above this temperature.

Research on deformation of polycrystalline TiC in bending and compression has been conducted by a number of investigators. Kelly and

Rowcliffe [41] investigated the plastic deformation of hot pressed polycrystalline carbides in four point bending and under compression. They found that a brittle to ductile transition occurs at approximately half the melting temperature of a carbide. TiC and VC recovered extensively on annealing for short times near 2000 °C. In a more recent extensive study, Das et al. [37] using four point bending and compression found that the brittle-ductile transition temperature of polycrystalline $TiC_{0.97}$ depends also on grain size. However, they determined that the yield stress was a function of grain size and could be described by a Hall-Petch type relationship. A yield point drop was observed in specimens deformed in compression at 1000 °C, but not at higher temperature where the stress-strain curve exhibited almost parabolic behavior. The activation energy for plastic deformation determined between 1050 °C and 1500 °C was of the order of 3.2 to 3.6 eV. Although these values are not close to the activation energy for C diffusion in TiC (about 5 eV), the authors concluded that the controlling mechanism is similar to the Kelly and Rowcliffe's model [31]. It was also observed that a remarkable improvement in bending strength resulted from annealing of the hot pressed samples at 2000 °C for 4 hours in vacuum. The drastic drop in strength between 900 °C and 1200 °C for as-hot pressed samples has been attributed to segregation of impurities such as Fe and Co to grain boundaries. SEM fractographs taken near the tensile surface of the bending specimens revealed that the fracture mode is predominantly intergranular for both types of samples tested at temperatures ranging from room temperature to 1575 °C. However, evidence for transgranular fracture was also found in specimens tested at lower temperatures.

VC.
of T
less
plan
Thi
nod

exa
of Z
TiC
inv
ori
{10
the
has
app
abs
sta
pre

str
at
pla
rat
Rc

Boron was found to significantly increase the strength of TiC and VC. Williams [42] reported that the critical resolved shear stress (CRSS) of TiC crystals is increased by a factor of five at 1600 °C by addition of less than 1% boron. He observed boride precipitates (TiB_2) on {111} planes and suggested that precipitation is the strengthening mechanism. This was confirmed by Venables [43] who also showed that dislocation nodes are important in acting as nucleation sites for this precipitation.

Plastic deformation in single crystals of other carbides have been examined to a lesser extent. Williams [22] has shown that single crystals of $ZrC_{0.88}$ are stronger than TiC at all compositions between $TiC_{0.79}$ and $TiC_{0.95}$, and this has been confirmed by Lee and Haggerty [34]. The latter investigators also measured the strength of $ZrC_{0.9}$ as a function of crystal orientation and induced slip on $\{111\}\langle 1\bar{1}0\rangle$, $\{110\}\langle 1\bar{1}0\rangle$ and $\{100\}\langle 1\bar{1}0\rangle$ systems, when the crystal orientation was chosen such that the Schmid factor favored slip on these systems. One observation which has not yet been explained is that the CRSS for slip on $\{110\}\langle 1\bar{1}0\rangle$ appears to be slightly lower than that for slip on $\{111\}\langle 1\bar{1}0\rangle$. The absence of both stacking faults and extended nodes indicates that the stacking fault energy is high. Additional TEM studies revealed the presence of well defined cell walls similar to earlier observations in TiC.

Darolia and Archbold [33] found that the compressive yield strength of arc melted polycrystalline $ZrC_{0.94}$ decreased from 77 kg/mm^2 at 1200 °C to 19 kg/mm^2 at 1800 °C. Yield drops were observed with plastic strain rates greater than 3 x 10^{-3}/sec but not with slower strain rates. The deformation rate results were consistent with the Kelly and Rowcliffe model. Hafnium carbide has been the least investigated of the

trans

data

incr

decr

temp

repo

{11

2.2

des

the

VC

ca

at

di

th

H

be

T

g

h

d

c

transition metal carbides because of its limited availability. The tensile data of HfC samples which contained 2 to 5% free carbon showed an increase in strength from room temperature to 1600 °C and a rapid decrease afterwards [23]. Microhardness of $HfC_{0.98}$ single crystals at low temperatures was measured by Rowcliffe and Hollox [28]. They also reported that the active slip system of HfC at room temperature was $\{110\}<1\bar{1}0>$.

2.2.3 Mechanical behavior of group V carbides

Venables et al. [44] have mentioned that cubic VC is more correctly described as a series of ordered compounds. Hollox [5, 46] has reported the effect of ordering and composition on the CRSS in single crystals VC_x. The primary slip system is again $\{111\}<1\bar{1}0>$; however, as the carbon content is increased, the yield strength passes through a maximum at $VC_{0.84}(V_6C_5)$ which is also the composition having the highest order-disorder temperature. Above the brittle to ductile transition temperature, the strength appears to be governed by one thermally activated process. However, two thermally activated processes control the deformation behavior of $VC_{0.75}$ and so this behavior appears to be similar to that of TiC. Williams [22] has shown that single crystals of $NbC_{0.76}$ exhibit a greater strength than either $ZrC_{0.88}$ or $TiC_{0.95}$. Kelly and Rowcliffe [41] have shown that hot pressed $NbC_{0.95}$ is stronger than $NbC_{0.88}$ of similar density, indicating an increase strength with carbon content over this composition range between 1500 °C and 2000 °C. A number of creep

studies on single crystals and polycrystals of NbC_x have been conducted previously. Some of the results of these studies are discussed in Section 4.1 along with the reported creep behaviors of the other TMMC.

Except for some measurements of microhardness [24, 25, 28], mechanical properties of TaC single crystals have not been extensively investigated. Santoro [15] studied a number of properties of carburized TaC filaments as a function of carbon content. He has shown a maximum in the microhardness and a minimum in the room temperature rupture strength between $TaC_{0.8}$ and $TaC_{0.85}$. He correlated these changes with several other physical changes, such as a change in color and a maximum in diamagnetism, and suspected an electronic structural transition in this composition range. Measurements of the bending strength of hot-pressed TaC_x (with 4% of Co binder) at high temperatures showed similar trends to that reported by Santoro [15], although the minimum bending strength occurred at $TaC_{0.9}$ [45]. In addition, the brittle to ductile transition temperature increases linearly with increasing carbon content from compositions within the $TaC+Ta_2C$ two phase field across the TaC region to the two phase TaC+C field.

The tensile strength of polycrystalline $TaC_{0.98}$ was measured at temperatures between 1800 °C and 2200 °C with a strain rate of 8.3×10^{-4}/sec [23]. The samples were made from Ta sheets, carburized in graphite powder at 2700 °C to 3000 °C in vacuum or argon atmosphere. The elongation became noticeable at about 2000 °C and increased rapidly at higher temperature, while the strength decreased slowly. Below about 1850 °C, no reproducible values for the elongation could be obtained. The microstructure showed large carbide grains. At 2160 °C, the UTS was

98 MPa and an elongation of 33% was obtained. Necking was definitely observed, but there was little, if any, separation of grains visible in the microstructure after test.

Kelly and Rowcliffe [41] reported a ductile to brittle transition at about 1750 °C for hot pressed polycrystalline TaC. In their study employing four-point bend tests, they found further that even at 2000 °C only a small permanent strain of 0.1% could be achieved prior to failure. However, Becher [35] observed significant plastic deformation in compression tests even at temperatures as low as 1280 °C at strain rates ranging from 8.3×10^{-4}/sec to 8.3×10^{-6}/sec. He also suggested that the deformation occurred in part by dislocation motion controlled by carbon diffusion in contrast to the previous result by Steinitz [23].

The most extensive studies on the carburized thin sheets of TaC_{1-x} have been performed by Martin and coworkers [36, 47]. They performed four-point bending experiments up to 2200 °C and strain rates ranging from 10^{-7}/sec to 4×10^{-4}/sec. They showed that the specimens could undergo extensive plastic deformation above 1500 °C for a strain rate of 10^{-4}/sec (1200 °C for strain rate of 10^{-7}/sec). Annealing effects became evident only at very high temperatures and low strain rates (1900 °C and 10^{-7}/sec, 2000 °C and 10^{-6}/sec, T>2100 °C for higher strain rates) and were considered to be caused by dislocation climb. They analyzed the results of bending tests in terms of a strain rate law of the type:

$$\dot{\varepsilon} = A(\sigma - \sigma_i)^{\alpha} exp\left[\frac{(\sigma - \sigma_i)V}{kT}\right] exp\left(\frac{-\Delta U}{kT}\right) \qquad (3)$$

where, $\dot{\varepsilon}$ is the strain rate, A and α are constants, σ is the applied and σ_i

is the

consta

The r

carbo

revea

and t

repor

speci

of di

Allis

singl

carb

carb

defo

is the internal stress, V is an activation volume, k is Boltzmann's constant, T is the absolute temperature and ΔU is an activation energy. The results of their study were interpreted on the basis of a model of carbon diffusion assisted glide of dislocations.

TEM studies of the dislocations in deformed $TaC_{0.7-0.8}$ samples revealed stacking fault fringes bounded by Shockely partial dislocations, and these were interpreted as a result of shearing [10]. Martin [47] also reported the dissociation of dislocations in the deformed $TaC_{0.93-0.95}$ specimens by using weak beam dark-field microscopy. He found the width of dissociation to decrease with increasing carbon content [36]. Recently, Allison et al. [48] analyzed the carbon concentration in stacking faults of single crystals of $TaC_{0.78}$. The analysis showed a significantly lower carbon concentration in the fault. They concluded that the diffusion of carbon away from the moving dislocation must accompany plastic deformation.

2.3

2.3.

con

tem

ten

mo

hor

ten

abo

cur

Th

cu

co

pr

ac

du

D

oc

st

in

2.3 FUNDAMENTALS OF CREEP IN CRYSTALLINE SOLIDS

2.3.1 Creep curves

Creep is a time dependent deformation of materials under a constant load or stress. Although creep can occur at low homologous temperatures, creep of most materials is usually not significant at temperatures below 0.3 T_m, where T_m is the melting point. Therefore, most practical creep experiments have been performed at higher homologous temperatures. The range of temperature for intermediate-temperature creep usually lies between 0.3 T_m and 0.5 T_m. The creep above 0.5 T_m is regarded as high-temperature creep.

Creep in a solid can be represented by a creep curve. The creep curve is a plot of strain versus time for a given stress and temperature. The creep rate is determined as the slope of the creep curve. Typical creep curves of annealed crystalline materials in tension are normally composed of four stages (Figure 4): instantaneous strain, transient or primary creep, steady-state or secondary creep, and tertiary or accelerating creep. The creep rate continuously decreases with time during the transient creep and is constant during the steady-state creep. During the tertiary creep, the creep rate increases until creep rupture occurs. In compression tests, tertiary creep is absent and, following the steady-state creep period the creep rate decreases continuously as strain increases. The extent of each stage depends mainly on the temperature and the

Figur

const

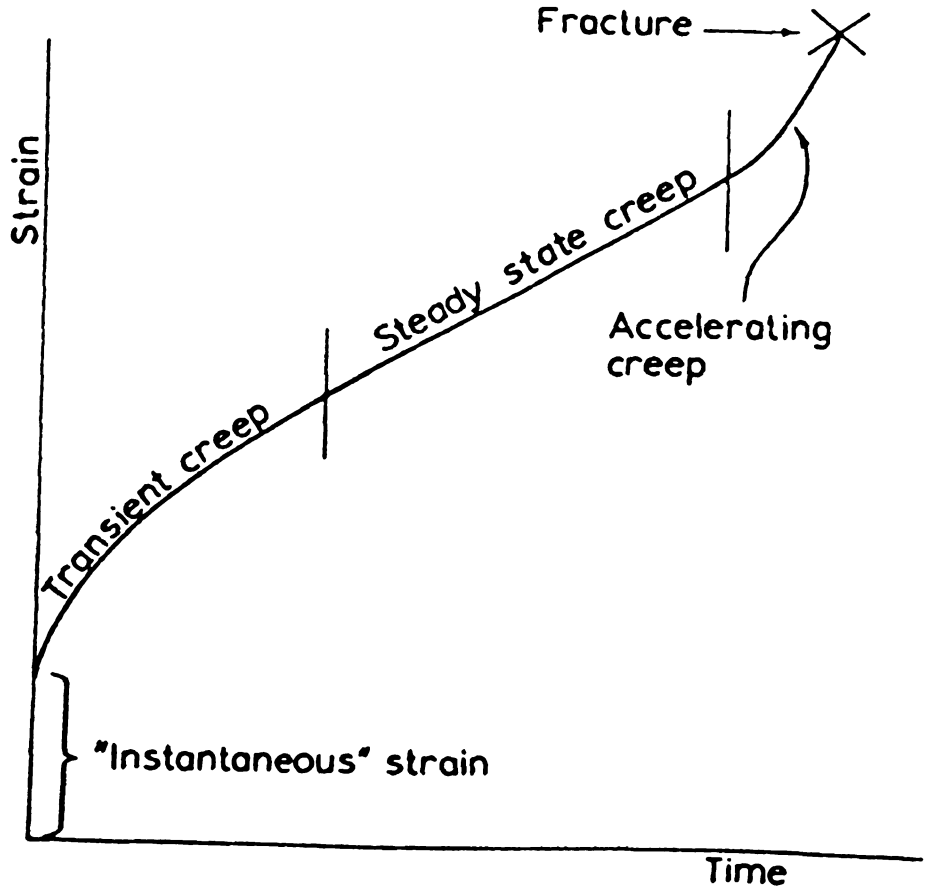

Figure 4. Schematic drawing of typical creep curve observed under a constant tensile stress (From Ref. [52]).

app

stag

whi

pla

the

str

loa

the

str

du

dis

str

cu

su

cu

sc

cr

tr

du

bo

cr

m

p

o

applied stress of the creep test. Thus, a creep curve with four well-defined stages can be observed under certain conditions of stress and temperature.

Phenomenologically, creep can be considered as a process during which two competing processes of strain hardening and recovery take place. The decrease in creep rate during primary creep is associated with the strain hardening process, i.e. with gradual changes in the dislocation structure. Dislocations, which are homogeneously distributed upon loading, begin to form cells or subgrains. The constant creep rate during the steady-state creep stage results from a dynamic balance between strain hardening and recovery processes. The substructure development during steady-state creep is characterized by a constant average dislocation density and constant subgrain size despite increasing creep strain.

Besides the typical creep curve, several different shapes of creep curves have been observed for various materials and these were summarized by Bird et al. [49]. The major difference between these creep curve were found over the transient creep regime. For certain solid solution alloys in which the solute drag effects on dislocations control creep resistance, the creep rate increases with creep strain during the transient creep period. The creep curves of many solid solution alloys during the transient creep stage are often sigmoidal in nature because of both solute drag and strain hardening effects [50]. The shape of creep curves also can be affected by the thermomechanical history of a material. For example, a continuous increase in creep rates during primary creep was observed in some prestrained and recovered specimens of pure nickel and nickel alloys [51].

2.3

em

ma

of

the

wl

ap

th

m

di

te

cr

te

te

fe

a

s

2.3.2 Steady-state creep

In most theoretical and experimental creep studies, the major emphasis has been placed on the steady-state creep stage. For many materials, it has been found that the temperature and stress dependency of the steady-state creep rate can be best represented by an equation of the form:

$$\dot{\varepsilon}_s = A_c\left(\frac{\sigma}{\mu}\right)^n exp\left(\frac{-Q_c}{kT}\right) \tag{4}$$

where $\dot{\varepsilon}_s$ is the steady-state creep rate, A_c is the creep constant, σ is the applied stress, n is a constant known as stress or creep exponent, Q_c is the activation energy for creep, k is Boltzmann's constant, μ is the shear modulus and T is the absolute temperature. It has been found that different creep mechanisms can be operative depending on the range of temperature and the applied stress for the creep test. Some important creep mechanisms are discussed in Section 2.3.3.

The value of the activation energy for creep can depend on temperature; for example, in Al [53]. At low or intermediate-temperatures, the activation energy for creep is usually lower than that for self-diffusion. For high-temperature creep, it is established that the activation energy for creep is nearly equal to the activation energy for self-diffusion [54].

Sherby and Burke [55] discussed the structural variables that are

important in the power-law creep of polycrystalline materials. These variables include elastic modulus, stacking fault energy, grain and subgrain size. In general, an increase in elastic modulus yields a large decrease in creep rate for a given stress. Thus, materials having a higher elastic modulus can be expected to be more creep resistant than ones with lower elastic modulus provided that other variables are the same. An opposite trend was observed for the dependency of stacking fault energy on the steady-state creep rate. The analysis of creep data for pure FCC metals revealed that the creep rate increased with increasing stacking fault energy (γ). The creep rate was found proportional to $\gamma^{3.5}$. An explanation for this behavior is due to the greater difficulty in climb for the widely separated partial dislocations of low stacking fault energy materials. The stacking fault energy can also influence the creep rate in an indirect way by affecting the subgrain size of materials. It was reported that the influence of grain size on the steady-state creep rate in pure metals was of minor importance. On the other hand the subgrain size seems to play an important role. In general, the creep rate of a fine subgrain size material is much smaller than that of coarse subgrain size material at the same stress level.

Cannon and Langdon [56] reviewed the creep behavior of ceramics and noted that the steady-state creep behavior of ceramics was similar to that of metals. Despite the overall similarity, they found that there were two major differences between the creep of ceramics and the creep of metals. First, diffusional creep with a stress exponent of 1 is a common deformation mode in ceramics. Second, the power-law creep behavior of ceramics yields stress exponents of about either 3 and 5, whereas pure

metals usually exhibit stress exponent close to 5.

The important contribution of diffusional creep in ceramics was attributed to a low grain boundary mobility, i.e. fine grain size, and the preferential enhancement of diffusion of one of the ionic species along grain boundaries in ceramics. For power-law creep behavior of ceramics, the stress exponent of about 5 was associated with fully ductile behavior and the stress exponent of about 3 was associated with plastic deformation in a less ductile condition, e.g. a lack of five independent slip systems. Cannon and Langdon [56] also concluded that the creep mechanism for the steady-state creep behavior with the stress exponent of about 3 was due to dislocation climb from Bardeen-Herring sources [57] under the conditions where crystallographic slip was restricted.

2.3.3 Mechanisms of creep

Although various mechanisms for creep deformation have been proposed in the past, there are basically two major creep mechanisms: dislocation creep and diffusional creep. Dislocation creep occurs by dislocation motion aided by vacancy diffusion. Depending on the level of stress applied in the creep test, dislocation creep mechanisms can be categorized into three creep regimes. They are known as power-law creep, Harper-Dorn creep and power-law breakdown. Diffusional creep usually occurs at low stresses and high temperatures by diffusion of vacancies only. The diffusional creep mechanism can be categorized into two cases, i.e. Nabarro-Herring creep and Coble creep. In the following,

some of characteristics of these creep mechanisms are briefly discussed.

In the stress range of $10^{-4} < \sigma/\mu < 10^{-3}$ and at temperatures above about 0.3 T_m, the stress exponent (n) in eqn.(4) varies between 3 and 8. This regime is called power-law creep. Two different cases of power-law creep may be distinguished. When the obstacles to dislocation motion have dimensions on the scale of a few interatomic distances, the dislocation may overcome these obstacles by thermally-activated glide alone. The power-law creep for this case is known as glide-controlled creep. Weertman [58] considered the case where dislocation glide over the Peierls barrier was the rate-controlling process of steady-state creep. She found that the creep rate in this glide-controlled creep followed a power-law and the value of the stress exponent was close to 3. It was noted that this model may be important in the case of non-metallic crystals with high Peierls stress.

The second case of power-law creep occurs when the obstacles to dislocation motion are too wide to be overcome by thermally-activated glide alone. At high temperatures, gliding dislocations which are held up by obstacles, can overcome the obstacles by climb and then continue to glide to the next obstacles. The rate-controlling process in this case is the diffusion of vacancies to or from the climbing dislocations. The power-law creep by this climb-plus-glide sequence is known as climb-controlled creep. In general, climb-controlled creep is regarded as real power-law creep. From the Bailey-Orowan equation, it has been proved that the 'natural' stress dependency for any climb-controlled creep is a power-law with stress exponent n=3 [59]. In the climb-controlled creep model proposed by Weertman [60], she considered that the groups of dislocation

dipoles form from the dislocation loops which were created at dislocation sources. She assumed that each dislocation glides the mean radius of the loops before it climbs a half of the spacing between parallel slip planes of neighboring dislocation sources and that the dislocation glide makes the major contribution to the creep strain. Using a relation between the glide velocity and the average climb velocity of dislocations, it was found that the creep rates varied by a power-law with a stress exponent of 4.5. Mukherjee et al. [54] showed that many aspects of steady-state climb-controlled creep could be correlated by the following semi-empirical equation.

$$\dot{\varepsilon}_s = A\frac{D\mu b}{kT}\left(\frac{\sigma}{\mu}\right)^n \tag{5}$$

where, A is a constant, D is the respective diffusion coefficient, and b is the Burgers vector. It was found that for climb-controlled creep of pure metals and solid solution alloys, the stress exponent (n) generally ranges from 4 to 7. The equation (5) is also known as the Dorn equation [54].

At low stresses, $\sigma/\mu \leq 5 \times 10^{-6}$, the creep rate is found to be proportional to the stress, i.e. n=1. If it is due to dislocation creep, it is called Harper-Dorn creep. Harper and Dorn [61] first observed this linear-viscous creep in Al polycrystals, which were deformed at near melting temperature and stresses lower than 0.09 MPa. Although this linear-viscous creep behavior is usually associated with the diffusion creep mechanism, they found that the creep rates were about three orders of magnitude greater than those predicted by Nabarro-Herring diffusional creep mechanism. Harper-Dorn creep was also observed in Al alloys [62]

and

Harp

cond

repo

cree

slip.

cree

with

thar

as p

can

con

can

hig

wh

an

br

di

di

N

hy

and CaO [63]. Based on TEM studies, Langdon et al. [64] proposed that Harper-Dorn creep arises from the climb of edge dislocations under the condition that jogs are saturated with vacancies. Mohamed et al. [65] reported that the dislocation substructure developed during Harper-Dorn creep in Al showed the absence of subgrains and the evidence of cross-slip. It is believed that Harper-Dorn creep is due to climb controlled creep under conditions where the dislocation density does not change with the stress.

At high stresses, $\sigma/\mu \geq 10^{-3}$, the creep rate is found to be faster than equation (4) predicts, i.e. n is large. This creep behavior is known as power-law breakdown or as the exponential creep region. This process can be considered as a transition from climb-controlled to glide-controlled flow. Luthy et al. [66] proposed an empirical equation which can describe the steady-state creep behavior between intermediate and high stress regime:

$$\dot{\varepsilon}_s = D_{eff} B \left(\sinh \alpha \frac{\sigma}{E}\right)^n \tag{6}$$

where, D_{eff} is the effective diffusion coefficient. B and α are constants. and E is the dynamic unrelaxed Young's modulus. The power-law breakdown starts at a value of $\alpha \equiv (\sigma/E)^{-1}$.

At high temperatures and relatively low stresses, $\sigma/\mu < 10^{-4}$, diffusional creep becomes the controlling mechanism of creep. For diffusional creep, the creep rate is proportional to the stress, i.e. Newtonian flow. Nabarro [67] and Herring [68] proposed that a non-hydrostatic stress field could give rise to a gradient of chemical potential

on grain surfaces and thus cause a diffusional flow of matter within the grain. This diffusion controlled creep process is referred to as Nabarro-Herring creep which can be represented as:

$$\dot{\varepsilon}_s = \alpha_{NH}\frac{D_v\sigma\Omega}{kTd^2} \tag{7}$$

where, α_{NH} is a constant, D_v is the lattice diffusion coefficient, Ω is the atomic volume and d is the grain size. Thus, for Nabarro-Herring creep, the creep rate changes with the square of the grain size and is proportional to the applied stress. For the Nabarro-Herring mechanism, the grains become elongated by the flow of vacancies from grain boundaries experiencing a tensile stress to those under compressive stress, and a simultaneous flow of the atoms in the opposite direction. This process is important only if the flux of vacancies is large, so the Nabarro-Herring creep is important for materials having small grain sizes and at high temperatures where the diffusion coefficient is large.

Coble [69] proposed a model in which the diffusional mass flow during creep occurred through grain boundaries. This diffusional creep mechanism is called as Coble creep. Coble creep generally becomes important at lower temperatures where grain boundary diffusion predominates over volume diffusion. The Coble creep equation can be described by the following equation:

$$\dot{\varepsilon}_s = \alpha_c\frac{D_{gb}\delta\sigma\Omega}{kTd^3} \tag{8}$$

Where, α_c is a constant, D_{gb} is the grain boundary diffusion coefficient,

δ is the

in Coble

Nabarro

that the

the inve

δ is the grain boundary thickness. As can be noted from the equation (8), in Coble creep the stress dependency of creep rate is the same as the Nabarro-Herring creep model. The important difference lies in the fact that the creep rate in Coble creep depends on the inverse of d^3 rather than the inverse of d^2 as in Nabarro-Herring creep.

RO

3.1

the

def

tes

to

bri

fre

lo

th

de

p

T

h

s

i

CHAPTER 3

ROOM TEMPERATURE DEFORMATION & ANNEALING OF TaC

3.1 INTRODUCTION

Most ceramic materials are known to suffer brittle fracture below their brittle-to-ductile transition temperature without any sign of plastic deformation, when they are subjected to conventional uniaxial or bending tests. The group IV and V transition metal monocarbides (TMMC) belong to this class of materials. The main reason for the low temperature brittleness of these materials is their high Peierls stress which comes from the very strong covalent bond between metal and carbon atoms. At lower temperatures the fracture strength of these materials is much lower than the yield strength, so that brittle fracture will occur before plastic deformation.

However, it has been shown for a number of brittle solids that plastic flow can occur at low temperatures e.g. during indentation [70]. This has been attributed to the fact that the stress around the indentation has a large hydrostatic stress component and that during indentation high shear stress can be obtained locally [71]. These promote slip while inhibiting brittle fracture. Therefore, microhardness indentation is a suitable method to investigate the deformation behavior of brittle solids at low temperatures.

In most previous studies on this subject, Vickers or Knoop indentations has been made on single crystals and the surfaces were etched to reveal the dislocations and slip traces. The anisotropy in the microhardness of single crystals along with etch-pitting of indented surfaces have been used to determine the slip systems of these materials [26]. The results of Knoop indentation experiments on single crystals of group IV and V transition metal monocarbides indicate that slip occurs preferentially by $\{110\}\langle 1\bar{1}0\rangle$ slip system at low temperatures except for some particular compositions of group V transition metal monocarbides [30]. It was reported that at room temperature plastic deformation of $NbC_{0.83}$ crystals took place by both $\{111\}\langle 1\bar{1}0\rangle$ and $\{110\}\langle 1\bar{1}0\rangle$ slip [29]. For single crystals of $TaC_{0.96}$ the preferred slip system was found to be $\{111\}\langle 1\bar{1}0\rangle$ by etch-pitting method [24] as well as analysis of the hardness anisotropy curve [28]. Rowcliffe and Warren [24] even observed significant plastic flow around indentations in $TaC_{0.96}$ single crystal deformed at liquid nitrogen temperature. They concluded that stoichiometric tantalum carbide was considerably softer than the other transition metal carbides and that it behaves like a relatively ductile material.

However, in order to study details of the plastic deformation process and the dislocation structure in a deformed material, high magnification of transmission electron microscopy (TEM) is necessary. TEM studies of Si single crystals deformed by indentation at room temperature have been reported earlier [72,73]. These results showed a high density of dislocations along with cracks or dislocation loops in the vicinity of the indentation. Annealing of the deformed crystals above 550 ^{o}C

caused a reorientation of the dislocation loops into approximately edge orientation or the formation of new screw-edge loops [73]. The indentation in alumina at room temperature was studied by TEM and the results gave evidence of plastic deformation by both slip and twinning in the vicinity of the indentations [74].

For TMMC, Morgan and Lewis [29] conducted a TEM study of dislocation arrangements around Knoop indentations for Nb_6C_5 single crystals in an attempt to confirm the slip process deduced from hardness anisotropy measurements. The transmission electron micrographs showed that the density of dislocations near the indentation is high and that lattice rotations occur within the small volume of deformation around the indentation. By trace analysis, the Burgers vector of dislocations at the periphery of the deformed region were identified to belong to the {111} $<1\bar{1}0>$ slip system. Although the details of the study were not presented, Rowcliffe [30] reported TEM micrographs of HfC crystals deformed at room temperature by indentation. The result of Burgers vector analysis of dislocations showed {110} $<1\bar{1}0>$ slip system in HfC crystals. No such studies have been reported yet for other TMMC.

The present study was undertaken to investigate deformation behavior of $TaC_{0.99}$ at room temperature by means of an indentation technique and transmission electron microscopy. The main purpose of the study can be described as the following: (1) to directly observe dislocation structures in $TaC_{0.99}$ crystals deformed by indentation; (2) to determine the active slip systems of $TaC_{0.99}$ at room temperature; and (3) to obtain information about the effects of annealing on plastically deformed $TaC_{0.99}$.

3.2

3.2.

pur

the

con

nur

spe

cut

(L

mi

se

gri

di

µn

bo

or

m

a

o

ir

3.2 EXPERIMENTAL PROCEDURE

3.2.1 Processing and characterization of tantalum carbide specimens

A hot pressed tantalum carbide rod with a square cross section was purchased from Cerac Inc. of Milwaukee, Wisconsin. The dimensions of the rod were approximately 11.4 mm × 11.4 mm × 153 mm. The chemical composition of the as-received TaC specimen is presented in Table 2. A number of $TaC_{0.99}$ specimens were cut out from the rod by using a low speed diamond saw (ISOMET™, Buehler Ltd., Lake Bluff, Illinois). After cutting, these specimens were mounted with thermoplastic powder (LUCITE®, Leco, St. Joseph, Michigan). The samples for optical microscopy and microhardness measurement were prepared as follows. A series of SiC papers, from 200 to 600 grit, were used for mechanical grinding and the final polished surface was obtained by using two size diamond compounds (MICROID® diamond compound, Leco), 6 μm and 1 μm, on nylon polishing clothes. An etchant for revealing the grain boundaries of TaC was the solution of 50% HF and 50% HNO_3 by volume.

The grain size was determined by using the linear intercept method on optical micrographs. The grain size obtained was the average of ten measurements. Microhardness was measured on the etched surface using a Vickers microhardness tester (Buehler Ltd.) with 1 kg load, 20 seconds of loading time and 50 μm per second in loading speed. In general, the indentations were made in the interior of grains and the microhardness

Table 2. The chemical composition of as-received TaC specimen*.

C / Ta Ratio	0.99	
Impurity (%)	Al 0.01	Nb 0.05
	B < 0.001	Ni 0.005
	Co 0.01-0.06	Si 0.01
	Fe 0.01	Ti 0.005
	Mo 0.02	W 0.01-0.09

* Data from CERAC Inc., Milwaukee, WI.

Table 3. Some characteristics of TaC specimens.

Specimen	Grain size(μm)	Vickers hardness(kg/mm^2)	Density(%)
As-received	22 ± 3	1178 ± 89	95*
HIP Processed	57 ± 6	1214 ± 70	97

was determined by averaging 10 to 15 indentation measurements.

In order to improve the density, hot pressed TaC specimens were hot isostatically pressed without encapsulation in hot isostatic pressing (HIP) containers. The time, temperature and pressure profile of the HIP process is presented as HIP #1 in Figure 40 of Section 5.2.2. After hot isostatic pressing, the density of the specimens was measured by the buoyancy method [75]. First, the specimens were cleaned with acetone and subsequently with methanol, and dried completely before measuring the weight in air (W_A) with a balance (Mettler instrument corp.) having an accuracy of 1×10^{-4} g. The weight of each sample used in these measurements was about 20 grams. A 0.09 mm in diameter copper and nickel alloy wire was tied to a sample on one end while the other end was made into a hook for hanging on the balance. The sample was then weighed (W_T) after being totally immersed in distilled water. It was carefully checked that no air bubbles adhered to the sample and the wire. The weight of the wire immersed in the distilled water up to a reference position was measured as W_O. The weight of the specimen in water (W_W) was calculated by the equation, $W_W = W_T - W_O$. The density of the specimen (ρ) was computed by the following equation:

$$\rho = \frac{(W_A \rho_W - W_W \rho_A)}{(W_A - W_W)} \qquad (9)$$

where, ρ_W and ρ_A are the density of water and air, respectively. The values of ρ_W and ρ_A used were 0.99679 g/cm^{3}and 1.181×10^{-3} g/cm^3 at a temperature of 26 °C.

Optical microscopy and hardness measurements were performed on

the I

both

pres

TaC

anne

3.2.

wer

and

slic

and

mn

ele

an

ca

sm

ad

bl

fil

co

3

th

p

the HIP processed specimens as mentioned before. The characteristics of both the as-received and hot isostatically pressed TaC specimens are presented in Table 3. In the following experiments, the HIP processed TaC was used as the specimens for the room temperature deformation and annealing study.

3.2.2 Indentation deformation and TEM specimen preparation.

Thin slices of $TaC_{0.99}$ between 0.1 mm and 0.2 mm in thickness were cut by a low speed diamond saw with application of a minimum load and speed in order to prevent chipping and tapering of samples. The slices were mechanically ground through various grades of SiC papers and finally polished with 6 μm and 1 μm diamond compounds. Discs of 3 mm in diameter were trepanned from the above slices by using either a electrical discharge machine (EDM) (AGIETRON, Model EMT 1.10) or an abrasive slurry drill(South Bay Technology Inc., Model 350). In the case of trepanning by EDM, a slice of tantalum carbide was glued to a small steel block using a mixture of silver powder and rapid cure adhesive. After the conductive adhesive was completely dry, the steel block was fastened on a magnetic holding plate and then the tank was filled with a solution of kerosene. As an electrode, a graphite and copper composite material was machined into a tube having an inner diameter of 3 mm.The electrode was lowered to the tantalum carbide specimen and the electrical discharge started. Typical machining speed was about 5 μm per minute. When the cutting was completed, the discs were removed

from the steel block by soaking in acetone.

For the abrasive slurry drill, a slice of tantalum carbide was mounted onto an aluminium plate with low temperature melting wax by heating on a hot plate to a temperature of about 120 °C followed by cooling to room temperature. The abrasive slurry employed was a mixture of 400 mesh boron carbide powder, glycerol and water. After applying small amounts of slurry on the tantalum carbide specimen, a rotating brass tube having 3 mm in inner diameter was slowly lowered onto the specimen. A speed and a weight of the drill were adjusted to prevent specimen breakage during trepanning, and occasionally fresh slurry was added on the specimen. Typically, the time required to cut one disc out of a 0.1 mm thick slice was about 40 minutes. After the cutting was finished, the Al plate was cleaned with water until free from the slurry and reheated to remove the disc specimens. A residual of the wax on the disc specimens was further cleaned in acetone and ethanol.

The $TaC_{0.99}$ disc specimens were then mounted on a tantalum carbide block of about 12 mm in thickness by using an adhesive (DURO™ Super glue, Loctite Corp.) before applying Vickers indentations. The microhardness indentations were made at room temperature using a Vickers microhardness indenter with a load of 300 g applied for 5 seconds and a loading speed of 40 μm per second. On each disc, rows of 29 indentations were made with a spacing of about 50 μm. After indentation, the TaC discs were carefully separated from the block by soaking in acetone. Thin foils for TEM study were prepared in two stages. First, the surface opposite to the indented side was dimpled to the final thickness of 25 μm using a dimple grinder (Gatan dimple grinder Model 656). A

disc

and

grind

size

whe

side

hou

The

whe

cur

res

of

the

the

an

ro

19

M

d

g

A

a

t

disc was mounted on a sample stage with low temperature melting wax and the stage was centered with respect to a 10 mm diameter brass grinding wheel by using an optical microscope. A small amount of 3 μm size diamond compound and distilled water was supplied to the grinding wheel at intervals of few minutes.

In the second stage, the dimpled sample was thinned first from both sides by ion milling (Ion Tech., Teddington, England) for about 2.5 hours, and then thinned from the dimpled side until perforation occurred. The perforation of the TEM foil was detected by an optical microscope when the light source under the foil was seen through. The voltage and current of the ion milling process were 5 KV and 1.5 mA for each ion gun, respectively. The pressure of Ar gas was about 1×10^{-5} Torr. The angle of the incident ion beam was 30 degrees. In general, the time taken until the perforation occurred was between 15 and 20 hours. After perforation, the samples were further thinned from both sides with an incident beam angle of 18 degrees in order to increase the electron transparent area.

To study the annealing effect on $TaC_{0.99}$ after prior deformation at room temperature, some of the indented disc samples were annealed at 1992 ±1 °C ($\approx 0.53\ T_m$) for 1 hour in a vacuum furnace (Centorr, Model M-60) with a vacuum of about 2×10^{-6} Torr. In order to prevent possible decarburization, the samples were wrapped with about 0.15 mm thick graphite foil and placed in a graphite crucible before vacuum annealing. After the annealing, the samples were dimpled and thinned by ion milling as described above. In addition to these samples, TEM foils of undeformed $TaC_{0.99}$ were also prepared. For the undeformed specimens, both surfaces were dimpled for an equal amount to the final thickness of

about

elect

stage

with

repe

extr

cons

load

The

con

con

ord

about 25 μm followed by ion milling.

The thin foils were examined in a Hitachi H-800 transmission electron microscope (TEM) operating at 200 KV with a double tilting stage capable of tilting ±45° along both tilting axes. Usually thin foils with a relatively large transparent area were obtained after a few repetitions of ion milling and examination in the TEM. Because of the extreme brittleness of tantalum carbide thin foil TEM specimens, considerable care was needed during the preparation, transportation and loading-unloading process of thin foil specimens for TEM investigation. The Burgers vectors of dislocations were determined by using the conventional $\mathbf{g}\cdot\mathbf{b}$ analysis [76]. In most cases two different diffraction conditions in which the dislocations became invisible were obtained in order to determine the Burgers vectors unambiguously.

3.3 EXPERIMENTAL RESULTS

The optical micrographs of the as-received and HIP processed TaC specimens are shown in Figure 5(a), (b) and (c), (d), respectively. By comparing these micrographs, it can be seen that considerable grain growth has occurred during the HIP process and that the porosity has been decreased by the HIP process. The grain size and density of both specimens are presented in Table 3 of Section 3.2.1. The microstructure of the HIP processed specimen in Figure 5(d) shows that many pores are located at three-grain junctions. Some of pores located on two-grain interfaces can be seen to separate from grain boundaries. These pores may have resulted from the separation of pores from the grain boundaries during grain growth. Many pores are also found inside of grains, where they can not exhibit large shrinkage during the densification process [77]. Some of square or triangular shapes in Figure 5(b) and (d) are due to dislocation etch pits.

Figure 6 shows transmission electron micrographs of the TaC specimen before the indentation experiment. Individual dislocations and grain boundaries can be seen in Figure 6(a).The initial density of dislocations is relatively low. The double image of some of dislocations is probably due to three beam imaging conditions [76]. A grain boundary triple point is shown in Figure 6(b). The grain boundaries are clean without any second phase. The microstructure of TaC deformed by the Vickers indentation is shown in Figure 7(a). This micrograph was taken

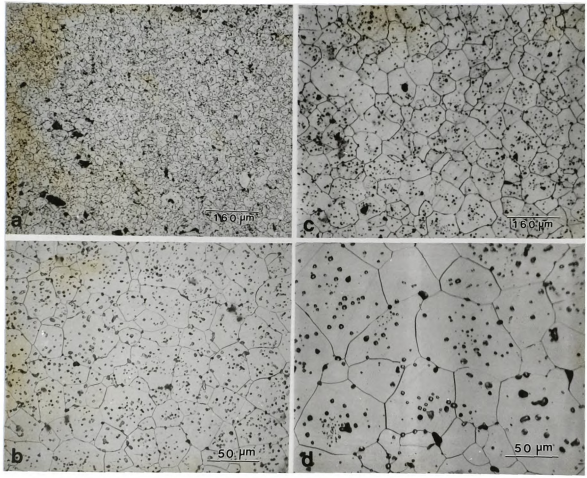

Figure 5. Optical micrographs of as-received and HIP processed $TaC_{0.99}$ specimen: (a),(b); as-received specimen, (c),(d); HIP processed specimen.

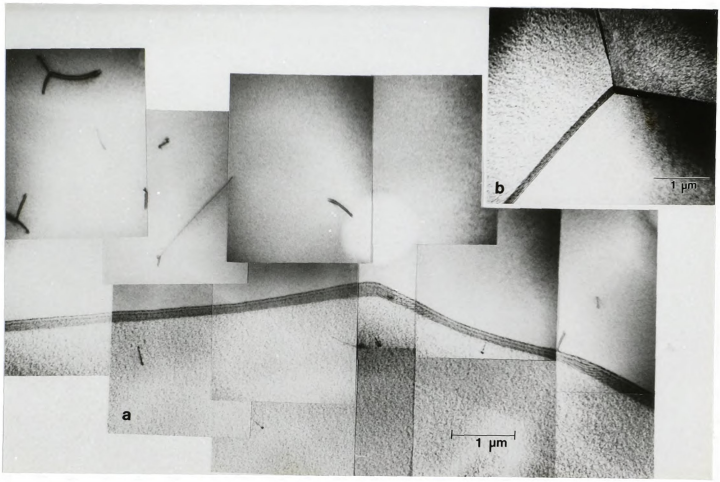

Figure 6. Transmission electron micrographs of undeformed $TaC_{0.99}$ specimen: (a) Near grain boundary region, (b) Triple grain boundary point.

around the area labeled as A in Figure 7(c). Figure 7(b) shows the corresponding selective area diffraction pattern (SADP) of the bright field image in Figure 7(a). Since the Vickers indentation was made well inside the grain, the deformation can be considered as indentation in a single crystal of tantalum carbide. The diffraction pattern belongs to the [111] zone of a B1 structure, so the plane parallel to the indented foil surface is close to a {111} plane.

In Figure 7(a), a very high density of dislocations can be seen in the region up to the distance of few microns away from an indenter facet. In this region dislocations are so highly tangled that the individual dislocations can not be resolved. Outside of this region, three different sets of dislocations can be identified. The acute angles formed by these sets of dislocations are about 60 degrees. One set of dislocations is not in good image contrast, but the two sets of long and straight dislocations are thought to lie in a {111} plane parallel to the foil surface along $<1\bar{1}0>$ directions. A set of dislocations near the bottom of the micrograph appears to be formed by a group of end-on dislocations which lie in another {111} plane inclined to the surface of the foil.

The Burgers vector analysis of one set of dislocations is shown in Figure 8. The beam direction and diffraction vector for each micrograph are denoted as **B** and **g** respectively. In Figure 8(b) and (d), the dislocations are out of contrast implying that the condition of $\mathbf{g}\cdot\mathbf{b}=0$ is satisfied, where **b** represents the Burgers vector. Since edge dislocations can give rise to contrast even if $\mathbf{g}\cdot\mathbf{b}=0$, the complete invisibility condition for a general dislocation is $\mathbf{g}\cdot\mathbf{b}\times\mathbf{u}=0$, where **u** is a direction of the dislocation line. But, in practice the dislocation contrast usually becomes

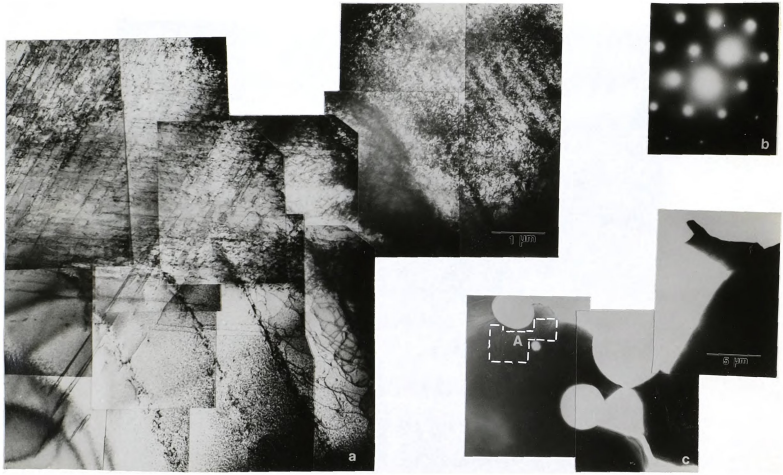

Figure 7. Transmission electron micrographs and the diffraction pattern of indentation deformed $TaC_{0.99}$ specimen: (a) Dislocation structures near the indentation, (b) Selective area diffraction pattern corresponding to $[111]_{B1}$ zone, (c) Low magnification image of the indented TEM foil.

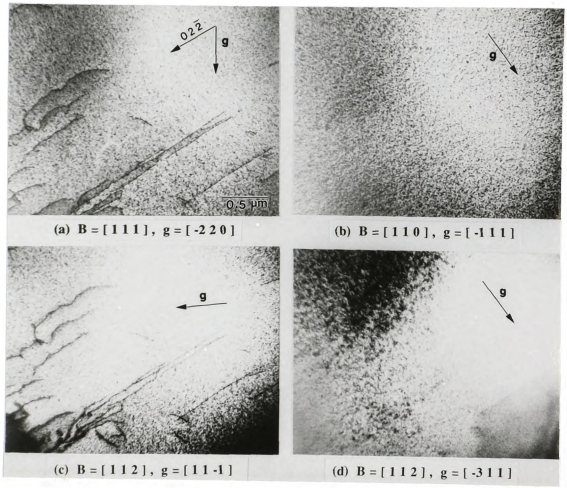

Figure 8. Burgers vector analysis of single set of dislocations: B; beam direction, g; diffraction vector.

ery weak when $\mathbf{g}\cdot\mathbf{b}=0$ except in some special cases [76]. The resultant lislocation contrast of this single set of dislocations is presented in Table . Since the dislocations are out of contrast with two diffraction vectors, $_1=[\bar{1}11]$ and $g_2=[\bar{3}11]$, the direction of the Burgers vector of these lislocations can be obtained from the cross product of diffraction ectors, i.e. $g_1 \times g_2 = [\bar{1}11] \times [\bar{3}11] = [0\bar{1}1]$. Therefore, the Burgers vector f these dislocations is a/2 $[0\bar{1}1]$, where a is the lattice parameter of $aC_{0.99}$. Since the Burgers vector and the direction of dislocations are arallel to each other, these dislocations are pure screw dislocations.

Table 4. Dislocation contrast of single set of dislocations.

g	$[1\bar{1}1]$	$[\bar{1}11]$	$[11\bar{1}]$	$[\bar{3}11]$
	Vi	Inv	Vi	Inv

where, Vi and Inv denote that the dislocations are visible and invisible respectively.

In another area of the specimen, two sets of dislocations apparently teract with each other as shown in Figure 9. This micrograph was taken ith a beam direction close to <112>. The intersecting angle between the o sets of dislocations is approximately 60 degrees. Elongated slocation dipoles, elongated loops and small loops are also seen in the me micrograph. The transmission electron micrographs for Burgers

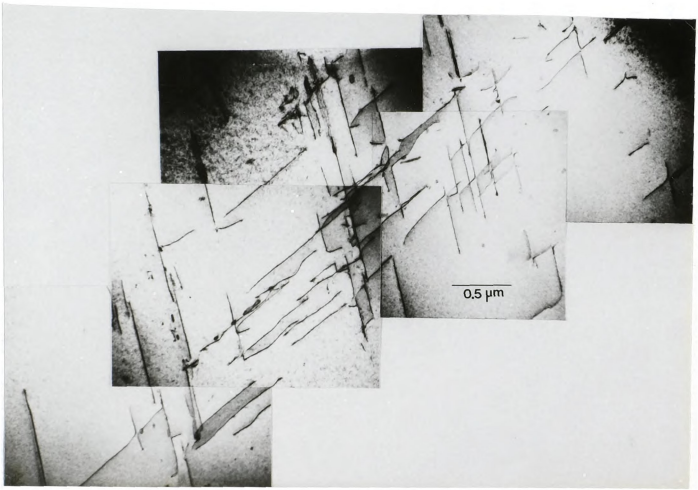

Figure 9. Transmission electron micrograph of two sets of dislocations.

vector analysis of the two sets of dislocations are shown in Figure 10. The two types of dislocations are denoted as 1 and 2 in Figure 10(a). The dislocations of type 1 and 2 are approximately oriented along the $[0\bar{1}1]$ and $[1\bar{1}0]$ directions, respectively. The dislocation contrast of the two sets of dislocations with four different diffraction vectors is listed in Table 5. From the result, the Burgers vectors of dislocations of type 1 and 2 were found to be a/2 $[0\bar{1}1]$ and a/2 $[\bar{1}10]$ respectively. Because some of these dislocations obviously lie in the same slip plane, the slip plane which contains both Burgers vectors will be (111). By considering the direction of the dislocation lines and the Burgers vectors, both dislocations are also pure screw type dislocations.

Table 5. Dislocation contrast of two sets of dislocations.

g	$[1\bar{1}1]$	$[\bar{1}11]$	$[11\bar{1}]$	$[\bar{1}\bar{1}3]$
1	Vi	Inv	Vi	Vi
2	Vi	Vi	Inv	Inv

The microstructure of an annealed $TaC_{0.99}$ specimen, which was ndentation-deformed at room temperature, is shown in Figure 11(a). igure 11(a) is a high magnification image of the region delineated by the otted line in Figure 11(b). In Figure 11, a recrystallized grain marked as can be seen in the vicinity of the indentation where the heavy plastic eformation might be occurred during the indentation. The region near

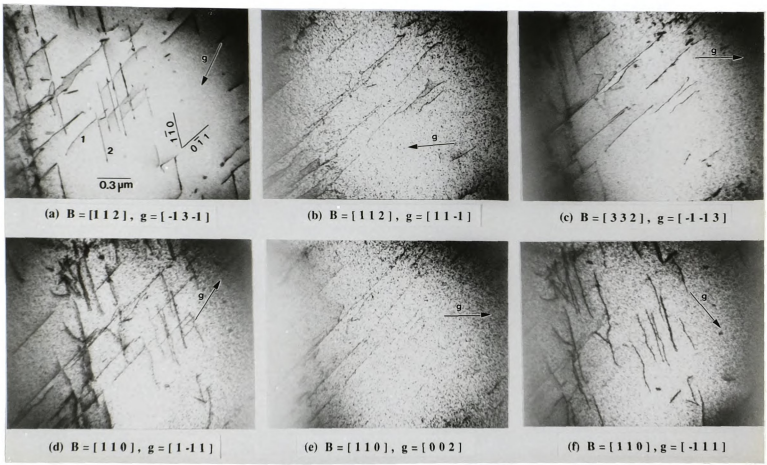

Figure 10. Burgers vector analysis of dislocations of type1 and 2: B; beam direction, g; diffraction vector.

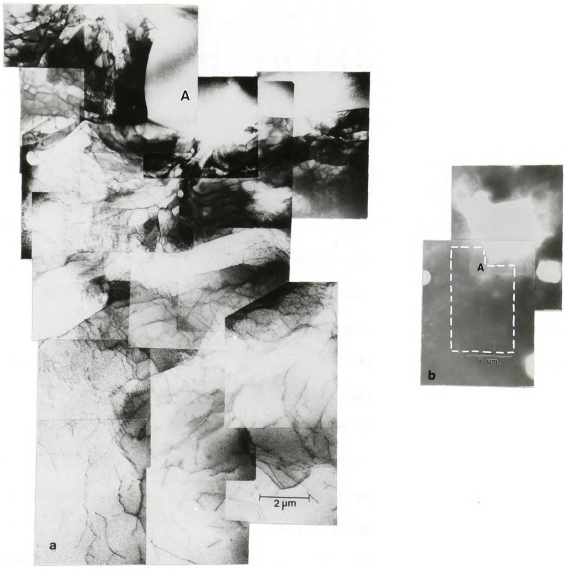

Figure 11. Transmission electron micrographs of the indented and annealed $TaC_{0.99}$: (a), (b); High and low magnification images near the indentation area of an annealed specimen.

the recrystallized grain contains the elongated subgrains indicating recovery during the annealing process. The high magnification image of the region next to the recrystallized grain is shown in Figure 12. This micrograph reveals well-developed subboundaries and hexagonal networks which are characteristics of recovered structures of face centered cubic (FCC) metals with high stacking fault energy, e.g. aluminium. From the observed changes of contrast it can be concluded that the orientation of the elongated subgrains occurred around the recrystallized grain is not uniform. A high magnification image of some of the subboundaries and hexagonal networks are shown in Figure 13. In the micrograph, twist boundaries (s) are clearly shown and some of hexagonal networks (n) are connected to the subboundaries by single dislocation. Further away from the center of the indentation where the dislocation density was low, the formation of a dislocation cell structure can be observed in Figure 11(a). A higher magnification image showing both the subgrain structure and the cell structure is presented in Figure 14.

In order to identify the Burgers vectors of dislocations forming the hexagonal networks in the annealed specimen, a Burgers vector analysis was performed on the hexagonal networks and is shown in Figure 15. Three types of dislocation components of the hexagonal network are denoted as 1, 2 and 3 in Figure 15(a). The summary of these dislocation contrasts with five different diffraction vectors is listed in Table 6. Calculating the cross products of diffraction vectors for which the invisibility criterion was satisfied, the Burgers vectors of dislocation of type 1 and 2 were found to be a/2 $[10\bar{1}]$ and a/2 $[0\bar{1}1]$. Because only one invisibility condition was obtained for dislocations of type 3, an

Figure 12. Transmission electron micrograph showing the region near the recrystallized grain.

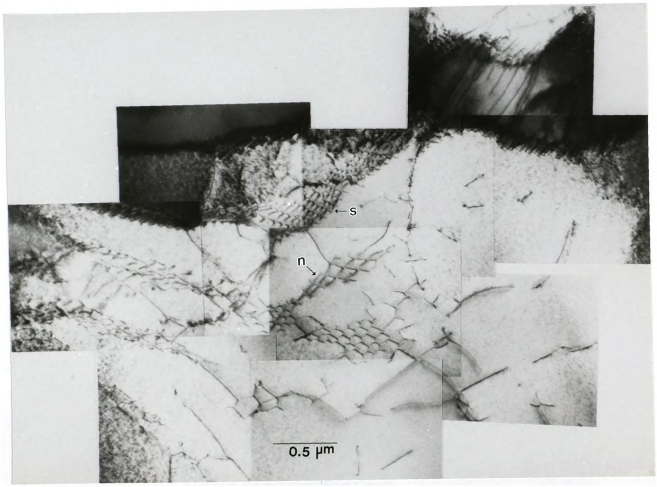

Figure 13. Transmission electron micrograph showing the subboundaries and hexagonal networks.

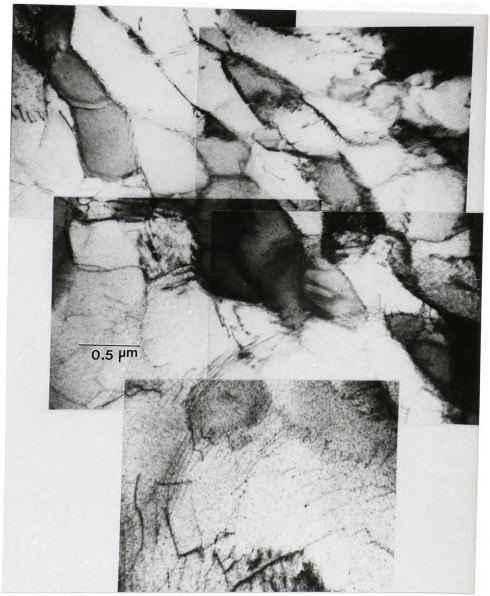

Figure 14. Transmission electron micrograph showing some of subgrains and cell structure.

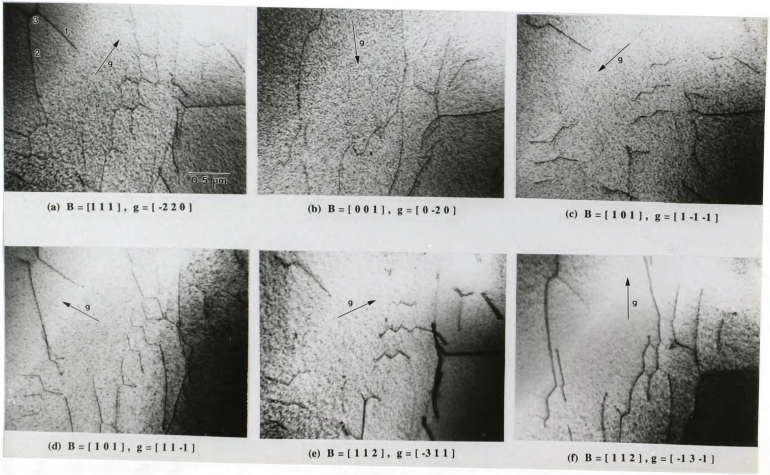

Figure 15. Burgers vector analysis of the hexagonal networks.

Table 6. Dislocation contrast of dislocations in hexagonalnetworks.

g	$[1\bar{1}\bar{1}]$	$[11\bar{1}]$	$[\bar{3}11]$	$[\bar{1}3\bar{1}]$	$[0\bar{2}0]$
1	Vi	Vi	Vi	Inv	Inv
2	Inv	Vi	Inv	Vi	Vi
3	Vi	Inv	Vi	Vi	Vi

unambiguous determination of the Burgers vector was not possible. However, the dislocations forming the networks should satisfy the condition that the Burgers vector is conserved at the nodes, i.e. $\mathbf{b}_1 + \mathbf{b}_2 + \mathbf{b}_3 = 0$, where the $\mathbf{b}_1$, $\mathbf{b}_2$ and $\mathbf{b}_3$ are the Burgers vector of dislocation of type 1, 2 and 3 respectively. Thus, the Burgers vector of dislocation of type 3 can be determined as a/2 $[1\bar{1}0]$. The result of the directional analysis indicates that these dislocations are mixed dislocations. Since the plane which contains all three Burgers vector is only (111), these dislocations might lie in the (111) plane.

In order to determine the orientation difference between subgrains of an annealed specimen, the Kikuchi patterns of two neighboring subgrain were obtained and indexed (Figure 16). The Kikuchi patterns in Figure 16(c), (f) and (h) indicate that the beam directions are $[\bar{1}27]$, $[\bar{1}14]$ and $[\bar{2}15]$ respectively. These Kikuchi patterns were obtained from the corresponding subgrain labeled 1. The Kikuchi patterns for subgrain 2 are shown in (b), (e) and (g) of Figure 16. By comparing these Kikuchi

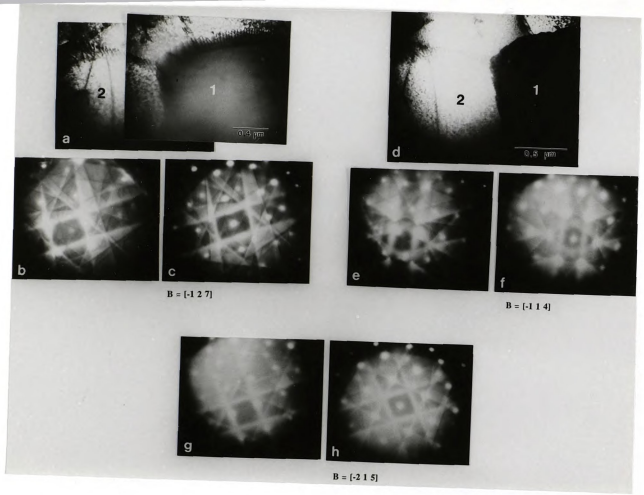

Figure 16. The Kikuchi pattern analysis of the misorientation angle between two subgrains: (a), (d); bright field images of two subgrains labeled 1 and 2. (c),(f) and (h); the corresponding Kikuchi patterns of subgrain 1. (b), (e) and (g); the corresponding Kikuchi patterns of subgrain 2. B; beam direction.

patterns with the corresponding Kikuchi patterns for subgrain 1, it can be noticed that the position of Kikuchi line pairs are displaced relative to the transmitted beam spot. The misorientation angle (θ) between subgrains 1 and 2 can be determined by the following equations: $\varepsilon = |\mathbf{a}| / L$ and $\theta = \arctan \varepsilon$, where ε is the tilt, $\mathbf{a}$ is the shift vector and L is the camera length [78]. The values of $|\mathbf{a}|$ and L used in the present study were 10 mm and 800 mm respectively. So ε is 0.0125 or the average of misorientation angle is about 0.72 degrees. This value is comparable to the generally reported values of the misorientation angle across low angle grain boundaries in metals.

3.4 DISCUSSION

The TEM study of $TaC_{0.99}$ specimens, which were deformed at room temperature by the Vickers indentation, revealed that extensive plastic deformation by slip occurred near the indentation area. The results of the Burgers vector analysis of the dislocations formed during the indentation process indicate that the slip system of $TaC_{0.99}$ at room temperature is $\{111\}<1\bar{1}0>$. This result is consistent with the earlier reported slip system of $TaC_{0.96}$ at room temperature [24,28].

In order to understand the plastic deformation behavior due to the microindentation, it is necessary to know the stress field forming around the indentation. Despite the simple nature of the indentation process, the stresses around an indentation are very complex. Hill [79] treated the problem of the indentation of plastically rigid material by a smooth wedge using the slip-line field theory. It was found that the slip-lines meet the indenter face at 45 degrees and the indentation pressure increased with the angle of the wedge. The pressure on the wedge was found to be distributed uniformly and the indentation produced the pile-up of material around the edge of the indenter. Samuel and Mulhearn [80] experimentally investigated the deformed zone associated with the Vickers indentation of a brass specimen. They found that the forces immediately below the impression are largely compressive and the mode of deformation resembles the radial flow of material away from the indenter. The indentation produced a 'sinking-in' impression instead of

'piling-up' type.

Marsh [81] considered that the elasticity of the deforming material is an important factor and pointed out that the mode of deformation in the work of Samuel and Mulhearn [80] is analogous to the expansion of a spherical cavity by an internal pressure. By using the results of Hill [79], he suggested the following expression for the indentation:

$$P/Y = C + KBlnZ \tag{10}$$

where, P is Vickers hardness number, Y is yield stress, C and K are constants, and B and Z are functions of Y/E, where E is the elastic modulus. It was found that for highly elastic material, i.e. for high Y/E, the ratio of P/Y was lower than that of an ideal plastic material. For an ideal plastic material, it is known that $P/Y \approx 3$ [79, 82].

Johnson [83] modeled the elastic-plastic indentation problem. It was considered that the small hemispherical core formed immediately below the indenter and within the core, a hydrostatic pressure was assumed. Outside the core, an ideal plastic region exists in which the stress and the displacements have radial symmetry and are the same as the case of the expansion of cavity by internal pressure. The elastic region lies beyond the plastic region. In case of single crystals, the analysis of deformation behavior by indentation is more complicated due to the marked anisotropy in plastic properties. Because polycrystalline TaC was used in the present investigation, it was not possible to align the edge of the indenter to a known direction on the known crystallographic plane in a grain. So the exact quantitative analysis of stress field around

the indenter was not possible.

However, a rough estimate of the stress which can cause the observed slip under the indenter can be made by using earlier results. According to the result of Marsh [81], the ratio of P/Y for glasses, which have high values of Y/E, was found to be about 2. Although the exact value of Y/E for tantalum carbide is not known, the Y/E ratio of tantalum carbide is considered to be high due to its high Y value. So it may be assumed that the ratio of P/Y for $TaC_{0.99}$ lies between 2 and 3. Since Y is approximately equal to 2S, where S is the shear yield stress, the shear stress is equal to the value between 0.17 - 0.25 P. Using the measured value of Vickers hardness (P) and the reported value of the shear modulus (μ) [18] for tantalum carbide, i.e. P ≈ 12 GPa and $\mu \approx 216$ GPa, the shear stress developed during the indentation is approximately 0.01 μ. At room temperature the Peierls stress (τ_p) of an edge dislocation in tantalum carbide for $\{111\}\langle 1\bar{1}0\rangle$ slip can be calculated by the equation [84,85]:

$$\tau_p = \frac{2\mu}{1-\nu} \cdot exp\left(-\frac{2\pi}{1-\nu}\frac{d}{b}\right) \qquad (11)$$

where, ν is Poisson's ratio, d is interplanar spacing and b is the Burgers vector. The values of ν, d and b are 0.24, $a/\sqrt{3}$ and $a/\sqrt{2}$ respectively, where a is the lattice parameter. The calculated value of the Peierls stress is about 0.003 μ. Thus, to a rough estimation, the shear stress developed during indentation is high enough to cause the plastic deformation of TaC by overcoming the Peierls barrier at room temperature.

In Figure 7(a), in the vicinity of the indentation where the stresses are very high, the highly tangled dislocation structure was formed and

this suggests that the slip in this region probably occurred by several symmetric {111}<1$\bar{1}$0> slip systems. The dislocations gliding on the different slip planes interact with each other, and form the dislocation tangles. This can result in high internal stresses in this region. Further away from the indentation, where the stresses are lower, the slip occurs on a reduced number of {111}<1$\bar{1}$0> systems to accommodate the strain and stress. A schematic sketch of the slip configuration for this region is shown in Figure 17.

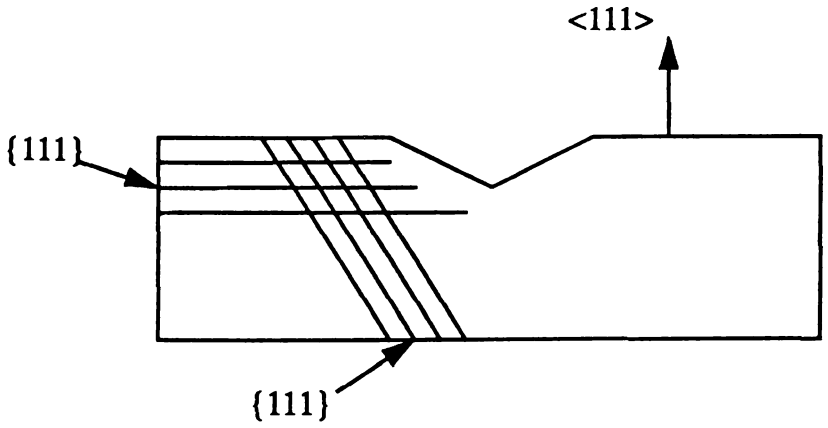

Figure 17. Schematic of the slip configuration near the indenter.

Two distinctive features of dislocations can be observed in this region. First, the long and straight screw dislocations are observed along the <1$\bar{1}$0> slip directions. Secondly, some of the dislocations show a wavy character as shown in Figure 8(a). The long screw dislocations observed in the current study are very similar to the dislocations

observ
tempe
forma
of the
disloc
the th
more
segm
struc
is no
dislo

dislo
deve
in th
able
disl
ther
be
plan
the
me
Na
ma
the
str

observed in the body centered cubic (BCC) metals deformed at low temperatures [86-88]. In BCC metals, it has been established that the formation of long screw dislocations is mainly due to the core structure of the screw dislocation [89]. The core structure of a/2 [111] screw dislocations in BCC metals was described as non-planar and spread into the three {110} planes of the [111] zone. Because of the dissociation on more than one plane screw dislocations are not mobile and form long segments due to the motion of the edge components. Whether the core structure of a/2 $[1\bar{1}0]$ screw dislocation in $TaC_{0.99}$ is planar or non-planar is not known. Hence, the dislocation motion and consequently the dislocation arrangement can not be explained at present.

However, a qualitative explanation of the formation of long screw dislocations in $TaC_{0.99}$ may be attempted. Due to high shear stress developed during the indentation, dislocation half-loops can be formed in the vicinity of the impression. Some of the dislocation loops, then, are able to expand due to the action of shear stress. If the velocity of an edge dislocation is assumed to be much higher than that of a screw dislocation, then dislocation dipoles with long screw segments of opposite sign will be formed as the mobile edge dislocation segments glide on the slip plane. The schematic of this process is sketched in Figure 18. Although the velocities of dislocations are not known for $TaC_{0.99}$, previous measurements of dislocation velocities in iron single crystals [88] and NaCl [90] indicated that the velocity of an edge dislocation is order of magnitude higher than that of a screw dislocation. The main reason for the low mobility of the screw dislocation is probably its higher Peierls stress compared to the edge dislocation. The wavy character of some of

Figur
segm
e; ed

screv

Thus

TaC(

disl

be r

wer

by t

Bur

inv

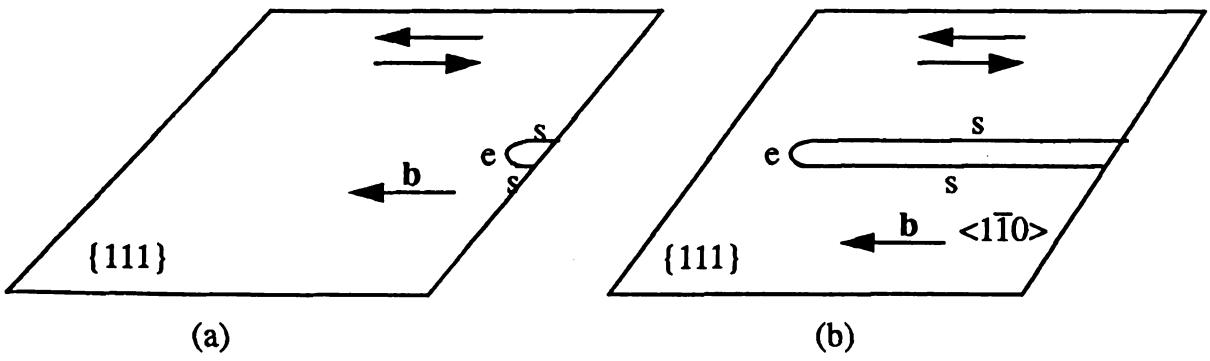

Figure 18. Schematic of the possible formation of long screw dislocation segments from the dislocation half-loop: (a) initial stage, (b) after glide, e; edge dislocation, s; screw dislocation, **b**; Burgers vector.

screw dislocations can also be attributed to their high Peierls stress. Thus, it can be considered that the low temperature deformation of $TaC_{0.99}$ is accomplished mainly by the glide of edge dislocations.

The dislocation structure in Figure 9 shows two sets of dislocations, dipoles and dislocation loops. A slightly darker contrast can be noticed between the long dislocations. Because these microstructures were not observed in the undeformed specimen, they have been formed by the interaction of dislocations during the indentation. The result of the Burgers vector analysis confirmed that the two sets of dislocations under investigation were of pure screw type. Therefore, the possible

interactions

microstructu

the same sli

joined by a

reaction [9

the nodes.

by the foll

The disloc

probably

very short

can be fo

separatio

small, so

can attra

the elong

Th

been rep

at low te

was prod

$TaC_{0.99}$

melting

occurre

grain fr

interactions between screw dislocations, which can result in the observed microstructure, will now be considered. When two screw dislocations on the same slip plane are meeting at a point as in Figure 9, two triple nodes, joined by a new dislocation segment, can be formed by a dislocation reaction [91]. The Burgers vectors of dislocations should be conserved at the nodes. In the present case, the new dislocation segment can be formed by the following dislocation reaction:

$$a/2\ [0\bar{1}1] + a/2\ [\bar{1}10] = a/2\ [\bar{1}01] \qquad (12)$$

The dislocation segments formed are not shown clearly in the micrograph probably due to the fact that the length of the dislocation segments is very short or the invisible diffracting condition is met. The screw dipoles can be formed by the aforementioned process (Figure 18). When the separation distance between two screw dislocations of the dipoles is small, some part of the screw dislocation segments with opposite signs can attract and annihilate each other. Thus, these dipoles may pinch off the elongated or small dislocation loops (Figure 9).

The annealing behavior of most transition metal carbides has not been reported probably due to difficulties in obtaining large deformation at low temperatures. In the present study, relatively large deformation was produced during indentation at room temperature. The annealing of $TaC_{0.99}$ subsequent to cold deformation by indentation at about half melting point resulted in an annealed dislocation structure with the occurrence of recrystallization and strong recovery. A recrystallized grain free of dislocations was formed in the vicinity of the impression

where the

agreement

formed in t

Next

dislocation

networks a

during rec

Figure 12

metals wit

evidence

micrograp

distance

carbon co

beam stu

deformati

revealed

of 2.7-5.

the disl

contents

$TaC_{0.99}$

dissociat

conventi

dislocat

used in

elongat

where the dislocation density was very high (Figure 11). This is in agreement with the established fact that the recrystallization nuclei are formed in the region where the dislocation density is greatest [92].

Next to the recrystallized grain, well-defined subgrains and dislocation networks are observed. The subgrains and the dislocation networks are known to form by dislocation glide and climb processes during recovery. The characteristics of these recovered structures in Figure 12 and 13 are very similar to the recovered structures of FCC metals with high stacking fault energy such as Al. In fact, there was no evidence of dislocation dissociation in $TaC_{0.99}$ from the TEM micrographs observed. A previous study indicated that the dissociation distance depends on the stoichiometry of tantalum carbide, i.e. as the carbon content increases, the width of dissociation decreases [36]. Weak beam studies of dislocations generated during high temperature deformation of TaC_x, where x was between 0.93-0.95, by Martin [47] revealed that the dislocations were dissociated into partials with spacing of 2.7-5.2 nm. However, it was argued that there is an uncertainty about the dislocation dissociation because of high oxygen and impurity contents in the specimen investigated [93]. From the current study on $TaC_{0.99}$ specimens, there is no evidence that the dislocations are widely dissociated. The dissociation may have been too small to detect by conventional TEM. Unfortunately, a good weak beam image of dislocations was not successfully obtained due to the relatively thick foil used in the current investigation.

Some of subgrains formed near the recrystallized grain were elongated and the orientation of elongation tended to change around the

indentation.

deformation

from the ind

annealing, d

cell walls. C

the annealed

center of t

dislocation

deformed fc

the driving

dislocations

off recrysta

indentation. This phenomenon is likely due to the strong anisotropy of deformation in the $TaC_{0.99}$ crystal near the indentation. Further away from the indentation where the dislocation density was low before the annealing, dislocations tend to form cells with low dislocation density cell walls. Corresponding to the strain distribution owing to indentation the annealed microstructures of $TaC_{0.99}$ also vary with distance from the center of the indentation, and far away from the indentation the dislocation structure resembles the dislocation arrangement of the deformed foil before the annealing. This is consistent with the fact that the driving force of recrystallization and recovery is the strain energy of dislocations, and that a critical driving force has to be overcome to set off recrystallization.

3.5 SUMMA

For th
microinden

1. Extensiv
   microin
2. The disl
   of long
   suggest
   motion
3. The lac
   $TaC_{0.99}$
   edge di
4. Screw d
   observe
   tempera
5. Strongl
   were ob
   These
   stackin

3.5 SUMMARY

For the first time the dislocation structure of $TaC_{0.99}$ deformed by microindentation at room temperature was observed by TEM.

1. Extensive local plastic deformation was observed in the vicinity of microindentations.
2. The dislocation structure of deformed $TaC_{0.99}$ consists almost entirely of long screw dislocations. The wavy character of screw dislocations suggests the existence of a high Peierls stress for screw dislocation motion at room temperature.
3. The lack of edge dislocations suggests that plastic deformation of $TaC_{0.99}$ at room temperature is mainly accomplished by the motion of edge dislocations, leaving long screw dislocation segments behind.
4. Screw dislocations were found to form nodes. Screw dipoles were observed to pinch off, forming dislocation loops during low temperature plastic deformation.
5. Strongly recovered microstructures and evidence of recrystallization were observed in $TaC_{0.99}$ specimens annealed after microindentation. These phenomena strongly resemble those found in metals with high stacking fault energy.

INTE

4.1 INTRO

As m
monocarbi
applicatio
TMMC at
comprehen
TMMC at
to be con
polycrysta
presented

Kei
$TiC_{0.96}$ p
and 1809
be about
732 KJ/m
have stud
stress an
At stress
was betw

CHAPTER 4

INTERMEDIATE-TEMPERATURE CREEP OF TaC

4.1 INTRODUCTION

As mentioned in Chapter 1, the group IV and V transition metal monocarbides have good potential for high temperature structural applications. Thus, it is important that the mechanical properties of TMMC at elevated temperatures are well known and thus have been comprehensively studied. Among these properties, the creep behavior of TMMC at elevated temperatures is one of the most important properties to be considered. A number of creep studies on single crystals and polycrystals of TMMC have been reported and some of them will be presented in the discussion below.

Keihn and Kebler [94] have conducted tensile creep tests on $TiC_{0.96}$ polycrystals within the range of temperatures between 1600 °C and 1809 °C in vacuum. The activation energies of creep were found to be about 544 KJ/mol below 1698 °C for the stress of 55.2 MPa, and about 732 KJ/mol above 1698 °C for the stress of 48.3 MPa. Spivak et al. [95] have studied creep behavior of $TiC_{0.63\text{-}0.96}$ polycrystals in the ranges of stress and temperature of 4.9-29.4 MPa and 2000-2650 °C, respectively. At stresses in excess of about 15 MPa the value of the stress exponent was between 3 and 4. The activation energy of creep at temperatures of

2000-2300 °

carbon diffu

about 4.9-9.

KJ/mol, wh

diffusion. T

14.7 MPa.

mechanism

the change

the homoge

compressiv

of tempera

exponent o

3.5 at mod

at tempera

KJ/mol, re

deformatic

temperatu

possible n

region we

carbon

respective

Lei

ZrC polyc

in the ra

MPa. The

below 21

2000-2300 °C was found to be very close to the activation energy for carbon diffusion in TiC. At temperatures above 2300 °C and stresses of about 4.9-9.8 MPa, the values of activation energy were about 565-598 KJ/mol, which corresponded to the activation energy for titanium self-diffusion. The stress exponents were found to be 1 below the stresses of 14.7 MPa. They suggested that creep occurred by the Nabarro-Herring mechanism under these experimental conditions. They also reported that the changes in the creep rate with stoichiometry were nonmonotonic in the homogeneity range of TiC. Chermant et al. [96] have investigated the compressive creep properties of polycrystalline $TiC_{0.93}$ within the ranges of temperature and stress of 1500-2000 °C and 8.8-93 MPa. The stress exponent obtained was 2.7 at high temperatures and low stresses, and was 3.5 at moderate temperatures and high stresses. The activation energies at temperatures below and above 1750 °C were about 380 KJ/mol and 650 KJ/mol, respectively. They concluded that the low temperature mode of deformation is controlled by the diffusion of carbon, and at high temperatures, deformation is controlled by the diffusion of Ti. The possible mechanisms of deformation for the low and high temperature region were suggested to be the thermally activated formation of kinks at carbon vacancies and non-conservative dislocation movement, respectively.

Leipold and Nielson [97] have studied the tensile creep behavior of ZrC polycrystals, which contains 1-2% free carbon at grain boundaries, in the ranges of temperature and stress of 1800-2600 °C and 2.5-34.5 MPa. They found that the activation energies for creep were 314 KJ/mol below 2150 °C and 837 KJ/mol above 2150 °C. The higher value of

activation en

free carbon,

3. Lee and

$ZrC_{0.945}$ sin

temperature

activation e

controlling

of dislocati

with the vo

specimen r

indication

the dissoci

Amo

relatively

compressiv

range of 1

below 22(

exponent

above 22(

respective

crystallog

below 22

diffusion

dislocatio

Nixon et a

intervals

activation energy was ascribed to the effect of impurities, principally free carbon, at grain boundaries. The stress exponent obtained was about 3. Lee and Haggerty [98] investigated the dynamic creep behavior of $ZrC_{0.945}$ single crystals at 1400 °C, 1600 °C and 2000 °C. Over the temperature range studied, the values of stress exponent and the activation energy were 5 and 460 KJ/mol, respectively. The rate-controlling recovery process proposed was the diffusion-controlled climb of dislocations, although the value of the activation energy agrees better with the volume diffusion of C in ZrC. The TEM micrographs of a crept specimen revealed well-defined cell walls, which may be a further indication of dislocation climb. In addition, no evidence was found for the dissociation of dislocations into partials in the crept specimen.

Among the group V carbides, the creep properties of NbC are relatively well-established. Dement'yev et al. [99] have conducted compressive creep tests on single crystals of $Nb_{0.89}$ in the temperature range of 1800-2700 °C at stresses of 11.8-68.6 MPa. At temperatures below 2200 °C, the values of the activation energy and the stress exponent were about 356 KJ/mol and 3.3, respectively. At temperatures above 2200 °C, these values were changed to 502 KJ/mol and 4.8, respectively. Based on these values, along with optical and x-ray crystallographic analyses, they proposed that the mechanism of creep below 2200 °C was viscous glide of dislocations controlled by the diffusion of carbon atoms, and that above 2200 °C the mechanism was a dislocation-diffusion mechanism controlled by the diffusion of Nb atoms. Nixon et al. [100] have studied the creep of HIPed $Nb_{0.74}$ polycrystals in the intervals of stress and temperature of 16.4-69.2 MPa and 1457-1827 °C,

respectively.
1657 °C and
respectively
exponents w
and TEM m
of steady-sta
and 1557-1
continued t
controlled
Che
research or
stress used
The values
1300 °C, 4
energy inc
High volta
arranged i
°C, and th
above 170
concluded
and annih
obstacles
regime an
in the h
extended
crept spe

respectively. The activation energies in the temperature ranges of 1457-1657 °C and 1627-1827 °C were found to be 240KJ/mol and 470 KJ/mol, respectively. In the stress ranges of 16-54 MPa and 48-70 MPa, the stress exponents were 2.0 and 3.2, respectively. By analyzing the kinetic data and TEM micrographs, they concluded that the controlling mechanisms of steady-state creep were either Peierls stress or cross slip at 1457-1497 °C and 1557-1657 °C. At 1827 °C, under low stresses, dislocation glide continued to control creep, but under stresses above 64 MPa, creep was controlled by climb.

Chevacharoenkul et al. [93,101] performed extensive creep research on $NbC_{0.775-0.873}$ single crystals. The ranges of resolved shear stress used were 6.9 to 44.4 MPa at temperatures from 1100 °C to 1800 °C. The values of the creep stress exponent were found to be about 3 at 1100-1300 °C, 4.6 at 1400 °C and 6.8 at 1600-1650 °C. The value of activation energy increased from 290 KJ/mol at 1300 °C to 546 KJ/mol at 1600 °C. High voltage electron microscopy revealed that the dislocations were arranged in the cell structures at temperatures between 1100 °C and 1600 °C, and that the dislocations arranged into subboundaries at temperatures above 1700 °C. From these kinetic data coupled with TEM studies, they concluded that the creep mechanisms in NbC_x involved dislocation glide and annihilation. The rate controlling processes were the surmounting of obstacles in cell walls during glide in the intermediate temperature regime and annihilation of dislocations by Nb diffusion controlled climb in the high temperature regime. No dissociation of dislocations or extended nodes were found in a weak-beam dark-field TEM study of the crept specimen.

Stein
polycrystal
between 19
no reliable
was estima
found to be
the activat
addition, it
deviation
creep in T
studies on

The
informatio
elevated te
at interme
creep test
TEM and
microstruc
results of

Steinitz [23] conducted tensile creep tests on $TaC_{0.92-0.99}$ polycrystals under the stresses of 45.9 and 68 MPa, at temperatures between 1960 °C and 2100 °C. Due to the fluctuation of carbon content, no reliable value for the stress exponent could be obtained, but the value was estimated to lie between 2 to 4. The activation energy of creep was found to be about 711 KJ/mol. This value was considered to lie between the activation energies of C diffusion and Ta diffusion in TaC. In addition, it was found that the creep rate of TaC decreases strongly with deviation from the stoichiometric composition. He proposed that the creep in TaC is controlled by a diffusion of Ta in TaC. No other creep studies on TaC have been reported yet.

The main purpose of the present investigation is to obtain information about the mechanical behavior of $TaC_{0.99}$ polycrystals at elevated temperatures, in particular the kinetics and mechanisms of creep at intermediate temperatures. The temperatures employed for the present creep tests were much lower than those investigated by Steinitz [23]. TEM and optical microscopy have been conducted to study the microstructure developed during the creep tests and to complement the results of creep tests.

4.2 EXPER

4.2.1 Creep

Hot
specimens
$TaC_{0.99}$ po
used for
chemical
were pres
specimens
3 mm in
were prep

Fi
by a sur
diamond
order to
were pol
smooth
11.4 mm
machine
machine
compute
deioniz

4.2 EXPERIMENTAL PROCEDURE

4.2.1 Creep specimen preparation

Hot pressed and HIPed $TaC_{0.99}$ polycrystals were used for specimens of the compressive creep study. The characteristics of the $TaC_{0.99}$ polycrystals were the same as those of specimens which had been used for the room temperature deformation study in Chapter 3. The chemical composition and some characteristics of $TaC_{0.99}$ polycrystals were presented in Table1 and Table2 of Section 3.2.1. The creep specimens were circular cylinders of approximately 6 mm in height and 3 mm in diameter i.e. with an aspect ratio of approximately two. They were prepared from a $TaC_{0.99}$ block as described below.

First, the top and bottom surfaces of the $TaC_{0.99}$ block were ground by a surface grinder (HARIG Model 618 Automatic) with a 150 grit diamond impregnated grinding wheel (Diamond Wheel Industries inc.) in order to obtain flat and parallel surfaces. After grinding, the surfaces were polished with a 1μm size diamond compound to obtain mirror-like smooth surfaces. The final dimensions of the block were approximately 11.4 mm × 6 mm × 50 mm. The cylindrical creep specimens were machined from this block by using a traveling wire electrical discharge machine (TWEDM, Raycon/Brother Model HS-300) equipped with a computer control system. The $TaC_{0.99}$ block was held by a small vise in deionized water. The cylindrical specimens were trepanned by electrical

discharge fro

was obtained

the starting

wheel to obt

4.2.2 Creep

Comp

machine (M

temperatur

power syst

control u

controller

MicroProf

personal c

test progr

of a moly

KN-100 K

and a LVI

displacem

Th

consisted

in diame

inner shi

of opera

discharge from the traveling brass wire. A nearly perfectly round surface was obtained, except for a cosmetic burr where the EDM wire cut through the starting point. The burr was carefully ground off using the diamond wheel to obtain the exact roundness.

4.2.2 Creep test apparatus

Compressive creep tests were performed using an MTS testing machine (Model 810, MTS Systems Corporation), equipped with a high temperature vacuum furnace (Centorr, Model S-60) and servohydraulic power system. The operation of the MTS machine was controlled by a control unit, composed of a MicroConsole (MTS 458.20), an AC controller (MTS 458.13), two DC controller (MTS 458.11) and a MicroProfiler (MTS 458.91). The control unit was interfaced to a personal computer for data acquisition and external control of various test programs. The two push rods, about 51 mm in diameter, were made of a molybdenum alloy (TZM). The upper push rod was connected to a 10 KN-100 KN load cell and the lower push rod was connected to an actuator and a LVDT(Linear variable differential transformer) for measurement of displacement.

The heating elements of the high temperature vacuum furnace consisted of a tungsten-mesh. The size of the hot zone was about 76.2 mm in diameter and 203.2 mm high. Radiation shielding was provided by two inner shields of W and four outer shields of Mo. The furnace was capable of operating up to 2000 °C either in vacuum or inert gas atmosphere.

The tempera
controller (
The temper
thermocoup
molybdenur
a malfuncti
additional t
of the furna
both high-v

Two
compressiv
block was
platens, ha
between th
a possible
temperatu
(Eagle-Pi
and 98%
creep spe
dimensio

For
1500 °C
specimen
to be too
deforma
contribu

The temperature inside the furnace was monitored by a temperature controller (Honeywell, Model UDC 5000 universal digital controller). The temperature measurement was achieved by a W-5%Re/W-26%Re thermocouple which was insulated with BeO and protected with a molybdenum sheath. In order to prevent possible overheating caused by a malfunction of the thermocouple during high temperature testing, an additional thermocouple was installed to limit the maximum temperature of the furnace. The safety of the furnace system was further provided by both high-vacuum and cooling water safety interlocks.

Two TZM compression blocks were used to transmit the compressive load to the $TaC_{0.99}$ creep specimen. The upper compression block was fixed to the upper push rod using two W-pins. The Al_2O_3 platens, having dimensions of about 6 mm × 6 mm × 1 mm, were inserted between the TZM push rods and the TZM compression blocks to prevent a possible diffusion bonding under the conditions of high stress and high temperature. Because of its excellent creep resistance, hot pressed α-SiC (Eagle-Picher Industries, Inc.), having a purity and density of about 99% and 98% respectively, was selected for a pair of compression platens. A creep specimen was placed in between these compression platens. The dimensions of the SiC platen were about 13 mm × 13 mm × 6 mm.

For the several initial creep tests at temperatures of 1300 °C to 1500 °C and stresses of 30 to 300 MPa, the displacement of the $TaC_{0.99}$ specimens were measured by the LVDT. However, these data were found to be too inaccurate because they included large contributions to the total deformation mainly from the Al_2O_3 platens. In order to eliminate the contribution of the deformation of the Al_2O_3 platen, a high temperature

extensomete

displacemen

temperature

shields and

TZM compr

the Al_2O_3

about 25.4

tests is sho

For t

the creep

temperatu

compressi

products i

data abov

reaction h

yield stre

conseque

the creep

4.2.3 Cre

Af

set up w

evacuate

the temp

extensometer (MTS, Model 632.51B) was employed to measure the displacements of the specimen during the creep test. The high temperature extensometer was equipped with water-cooled radiation shields and two Al_2O_3 extension rods. Grooves were machined into the TZM compression blocks in order to securely position the knife edges of the Al_2O_3 extension rods. The gauge length of the extensometer was about 25.4 mm. A schematic drawing of the specimen set-up for the creep tests is shown in Figure 19.

For the present creep test apparatus, the maximum temperature of the creep test was limited to about 1500 °C. One of main reasons for temperature limitation was due to the reaction between the TZM compression block and the SiC platen. The formation of the reaction products increased as temperatures increased and could affect the creep data above 1500 °C. In fact, local melting of the TZM block due to the reaction had occurred at about 1700 °C. The other reason was that the yield strength of TZM alloy significantly decreased above 1500 °C and consequently, plastic deformation of the TZM parts could occur during the creep test.

4.2.3 Creep tests

After the creep specimen and the extensometer had been properly set up with a preload of about 70 N, the furnace chamber was closed and evacuated for 3 to 4 hours. After the vacuum reached about 2×10^{-5} Torr, the temperature was slowly increased to the desired test temperature by

Figure 1

1.TZM p

5. SiC pl

rod, 9. E

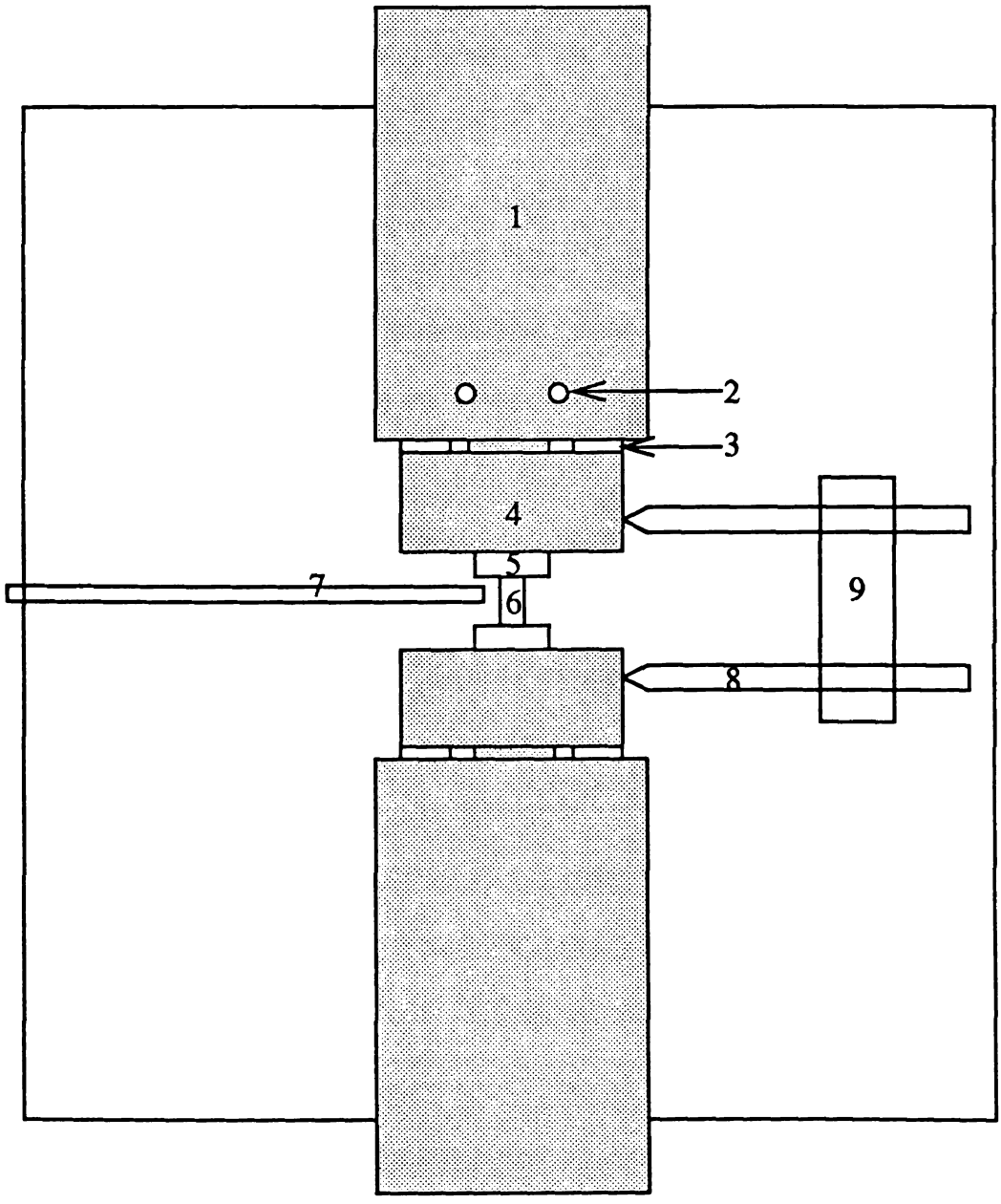

Figure 19. A schematic drawing of specimen set-up for creep tests: 1.TZM push rod, 2. W-pin, 3. Al_2O_3 platen, 4.TZM compression block, 5. SiC platen, 6. $TaC_{0.99}$ specimen, 7. Thermocouple, 8. Al_2O_3 extension rod, 9. Extensometer.

manually in

tests remain

The typical

reached the

a thermal

remained c

desired lev

specimen.

tests were

be regarde

was obtain

level was

Thre

TaC creep

°C/105 M

the creep

MPa to 17

creep de

acquisitio

70 hours.

about 2.4

Aft

transform

where e i

length of

creep rat

manually increasing the set-point of the controller while the mechanical tests remained under load control to compensate for thermal expansion. The typical heating rate was about 20 °C/min. When the temperature reached the test temperature, it was held for about 30 minutes to obtain a thermal equilibrium before applying the load. The temperature remained constant within about ±1 °C. The load was applied slowly to the desired level in order to avoid the possible fracture of the $TaC_{0.99}$ specimen. A typical loading rate was about 8 N/min. Although the creep tests were conducted under the condition of constant load, they can also be regarded as constant stress tests since only a very small final strain was obtained under the present creep conditions. The furnace vacuum level was about 4×10^{-5} Torr during the creep tests.

Three test conditions were employed to obtain the kinetic data of TaC creep. The combinations of the temperatures and stresses were 1400 °C/105 MPa, 1500 °C/105 MPa, and 1500 °C/170 MPa, respectively. For the creep test performed at 1500 °C, the stress was increased from 105 MPa to 170 MPa during the test, in order to find the stress dependency of creep deformation. The time interval between subsequent data acquisition was 5 minutes and a typical creep test was run for about 60-70 hours. The resolution of the data obtained from the computer was about 2.44 μm.

After the creep tests, the displacement data of the specimens were transformed to true strain using the relations: $e = \Delta l / l_o$ and $\varepsilon = ln\ (1+e)$, where e is the engineering strain, Δl is the displacement, l_o is the initial length of the specimen and ε is the true strain. In order to calculate the creep rates, polynomial regression analysis was performed on each set of

about 4 data

program. Th

i.e. $\varepsilon = at^2 +$

The strain r

correspondi

the strain i

time versus

The

about 60 M

for optical

the direct

specimen

Section 3.

between

along the

mm diam

using the

Th

and an i

side to t

ion gun

were si

3.2.2.

perpen

examin

of disl

about 4 data points of the time versus strain curve using the PlotIt® program. The polynomial regression model used was a quadratic equation i.e. $\varepsilon = at^2 + bt + c$, where a, b, c are constants and t is time in seconds. The strain rate at a particular strain was calculated by differentiating the corresponding regression equation and substituting the value of time for the strain into the equation. The PlotIt® program was also used to plot time versus strain and strain versus strain rate graphs.

The specimens crept at a temperature of 1500 °C and a stress of about 60 MPa were used for optical and TEM microscopy. The samples for optical microscopy were sectioned by a low speed diamond saw along the direction parallel to the compressive direction. The procedures of specimen mounting, polishing and etching were the same as described in Section 3.2.1. For TEM samples, thin slices of the crept $TaC_{0.99}$ specimen between 0.1-0.2 mm in thickness were cut by a low speed diamond saw along the direction parallel to the compressive axis. Disc samples of 3 mm diameter were trepanned from the middle portion of the slices by using the abrasive slurry drill.

The TEM foil was obtained by a combination of dimple grinding and an ion milling process. The disc specimens were dimpled from one side to the final thickness of about 25 μm and then ion-milled using two ion guns. The details of the dimple grinding and ion milling procedure were similar to the TEM foil preparation procedure described in Section 3.2.2. The direction normal to the TEM foil was approximately perpendicular to the compressive axis of the creep test. Thin foils were examined in a Hitachi H-800 TEM operating at 200 KV. Burgers vectors of dislocations were determined by using the standard $\mathbf{g \cdot b \times u}$ analysis.

4.3 EXPER

A cre
stress of ab
with an ins
decreased
instantane
slowly thr
about 0.64
about 105
obtained
20. An in
in an imm
onset of
creep in
the exten
creep str
MPa wer
In
plotted
Figure 2
1400 °C
continu
the end

4.3 EXPERIMENTAL RESULTS

A creep curve of $TaC_{0.99}$ polycrystals deformed at 1400 °C under a stress of about 105 MPa is presented in Figure 20. The creep curve begins with an instantaneous creep strain produced upon loading. The creep rate decreased markedly during the initial short period of time after the instantaneous strain. The creep rate kept decreasing, although much more slowly through the transient creep regime. The final strain obtained was about 0.64%. The creep curves obtained at 1500 °C under the stresses of about 105 MPa and 170 MPa are shown in Figure 21. The creep curve obtained under a stress of 105 MPa is very similar to the one in Figure 20. An increase in stress from 105 MPa to 170 MPa at 1500 °C resulted in an immediate increase in the creep rate. This can be considered as the onset of an additional transient creep. But, the extent of the transition creep in the curve obtained from the stress increment was much less than the extents of the transition creep in the other two creep curves. The final creep strains obtained at 1500 °C under the stress of 105 MPa and 170 MPa were about 0.77% and 1.3%, respectively.

In order to determine the steady-state creep rate, the creep rate was plotted versus the creep strain for three creep conditions as shown in Figure 22. The curves obtained under the creep conditions of 105 MPa at 1400 °C and 1500 °C exhibit a similar trend that the creep rates are continuously decreasing up to the end of creep tests. The creep rates at the end of the creep tests were very slow for both creep conditions.

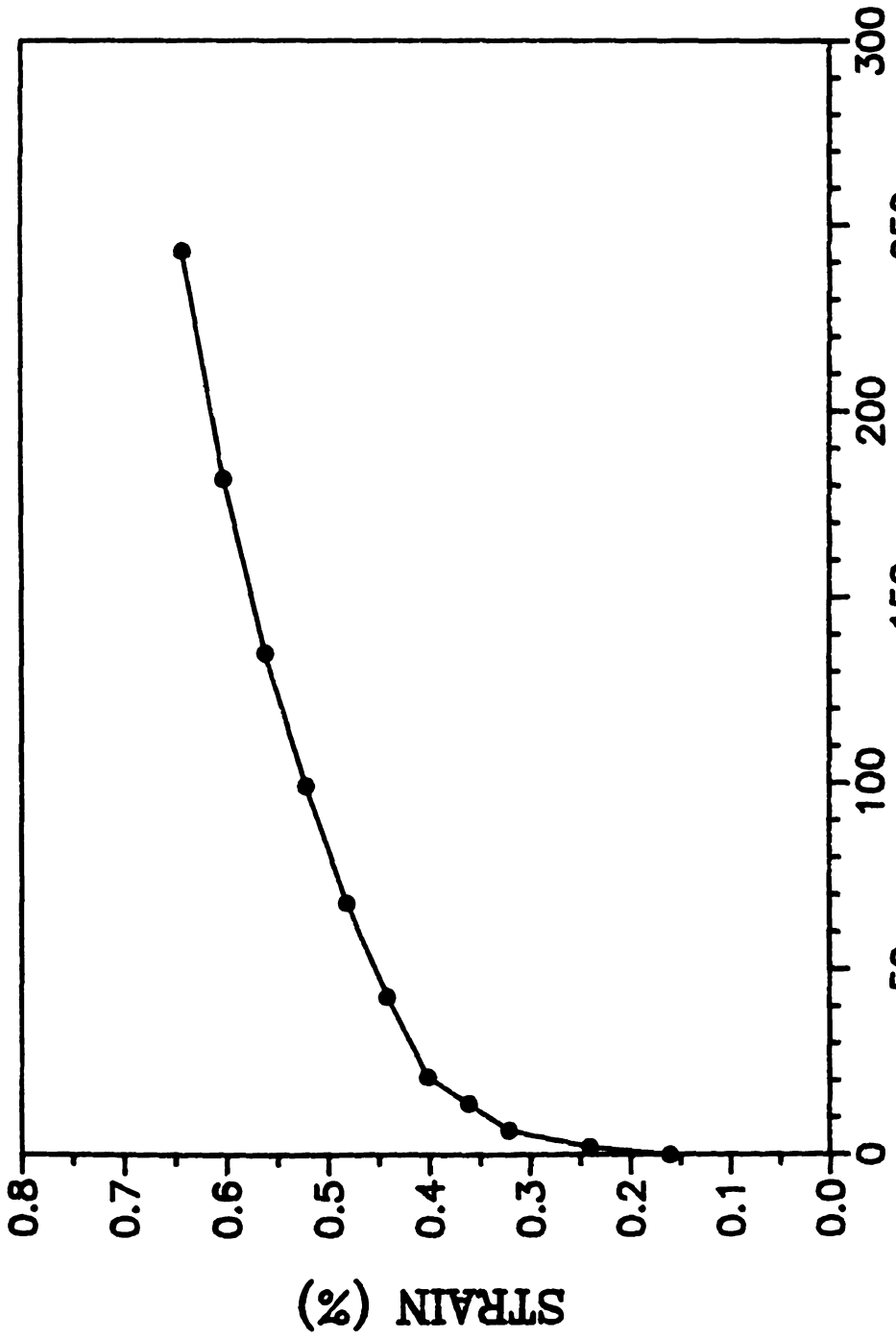

Figure 20. Creep curve of $TaC_{0.99}$ obtained under the conditions of 105 MPa and 1400 °C.

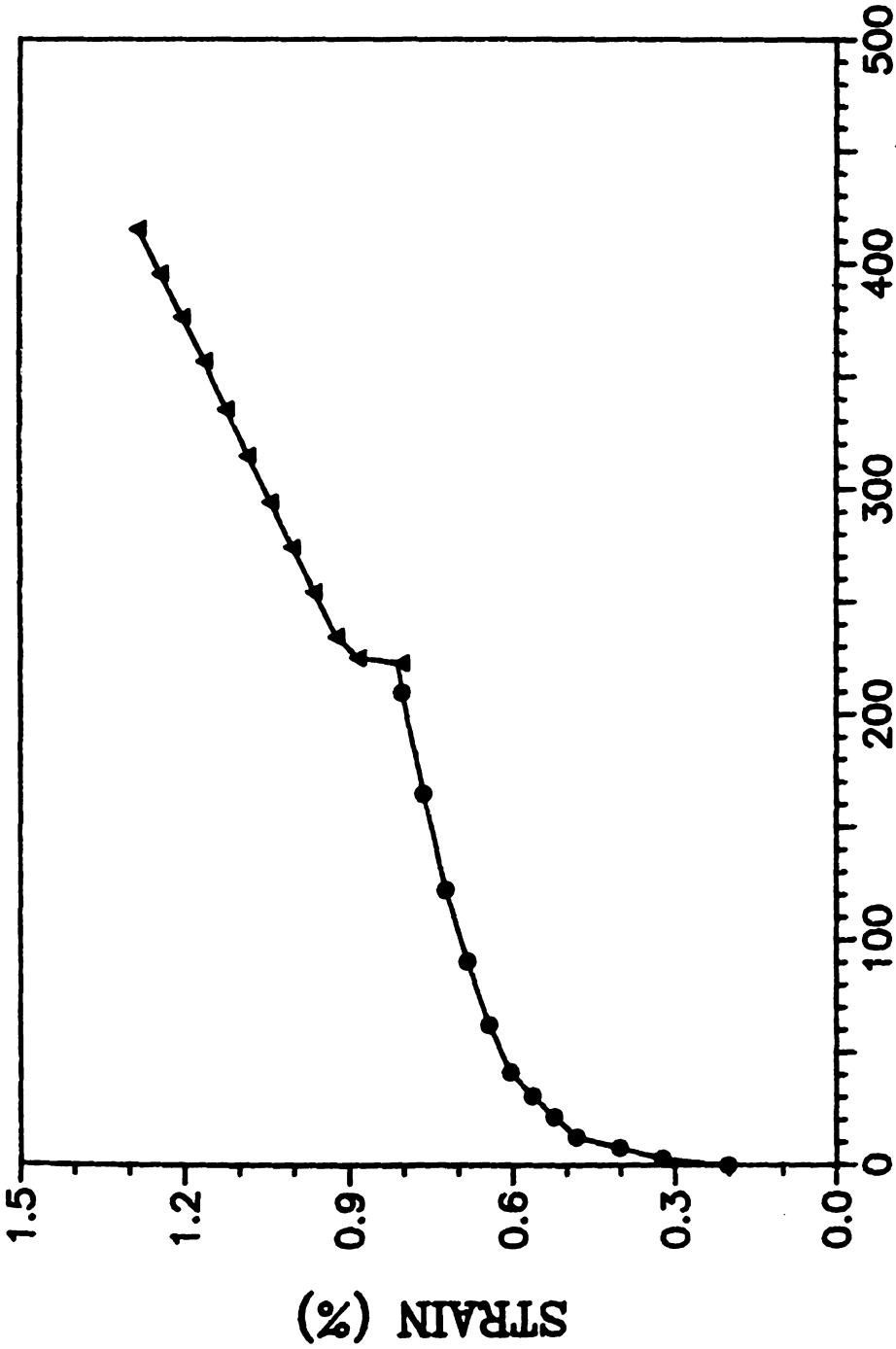

Figure 21. Creep curves of $TaC_{0.99}$ under the conditions of 105 MPa and 170 MPa at 1500 °C:

●; 105 MPa, ▲; 170 MPa.

80

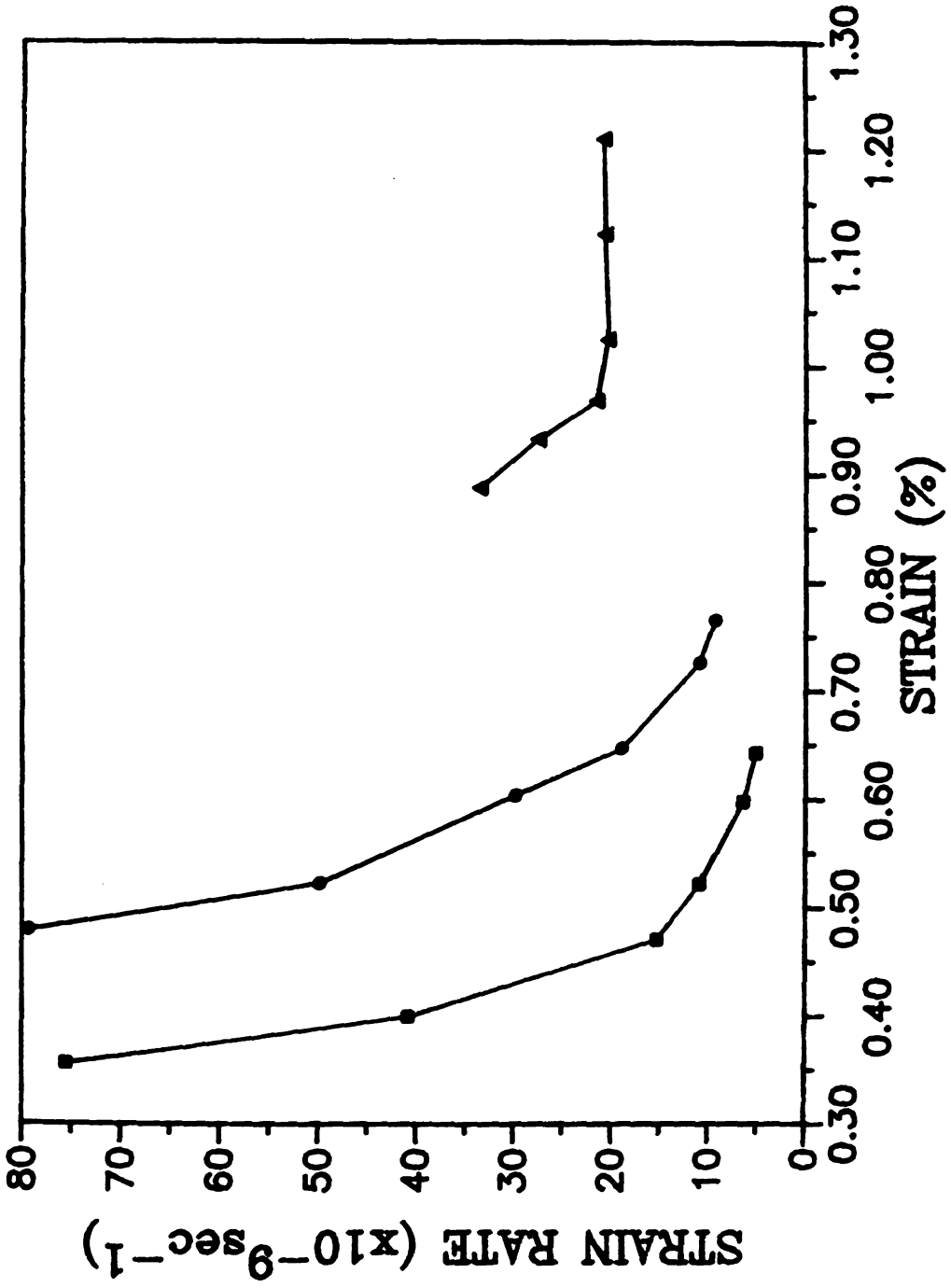

Figure 22. Strain rate as a function of strain: ■; 105 MPa/1400 °C, ●; 105 MPa/1500 °C, ▲; 170 MPa/1500 °C.

Although th
test conditi
to be nearly
as the quasi
and 1500
beginning
be regarde
rates for t

Table7. Q

Temperat
140
150
150

Fr
the acti
equatio

Although the true steady-state creep stages were not reached for these test conditions, the creep rate at the end of the creep tests were assumed to be nearly equal to the steady-state creep rates and thus, were regarded as the quasi steady-state creep rate. For the creep conditions of 170 MPa and 1500 °C, the creep rate decreased with the creep strain at the beginning and eventually attained a relatively constant value, which can be regarded as the steady-state creep rate. The quasi steady-state creep rates for three creep test conditions are given in Table 7.

Table7. Quasi steady-state creep rate data of $TaC_{0.99}$ polycrystals.

Temperature (°C)	Stress (MPa)	Quasi steady-state creep rate ($\times 10^{-9}$/sec)
1400	105	5.10
1500	105	9.34
1500	170	20.80

From the equation (4) in Section 2.3.2, the stress exponent(n) and the activation energy for creep (Q_c) can be obtained using the following equations:

$$n = \frac{\log(\dot{\varepsilon}_1/\dot{\varepsilon}_2)}{\log(\sigma_1/\sigma_2)} \qquad (13)$$

Where, $\dot{\epsilon}_1$ a
respectivel
state creep
value of t
energy for
A T
MPa is pr
consists c
dislocatic
interactic
dislocati
subgrain
strain, b
Op
stress o
microgr
specime
mainly
slightly
is indic
microg
which
located

$$Q_c = \frac{R ln(\dot{\varepsilon}_{T_1}/\dot{\varepsilon}_{T_2})}{1/T_2 - 1/T_1} \quad (14)$$

Where, $\dot{\varepsilon}_1$ and $\dot{\varepsilon}_2$ are the steady-state creep rates at stresses of σ_1 and σ_2, respectively. R is the universal gas constant. $\dot{\varepsilon}_{T_1}$ and $\dot{\varepsilon}_{T_2}$ are the steady-state creep rate at temperatures of T_1 and T_2, respectively. The calculated value of the stress exponent at 1500 °C was about 1.8. The activation energy for creep was calculated to be about 150 KJ/mol.

A TEM micrograph of a specimen crept at 1300 °C and about 300 MPa is presented in Figure 23. The dislocation structure of this specimen consists of dislocation dipoles, numerous dislocation loops and curved dislocation segments probably due to the dislocation-pinning and the interactions with other dislocations. No evidence for the formation of dislocation cells or subgrains can be observed. The dislocation cells or subgrains may not be formed under this creep condition with very low strain, but also the area observed in the TEM foil was not very large.

Optical micrographs of a specimen crept at about 1500 °C under a stress of about 60 MPa is shown in Figure 24. A low magnification micrograph in Figure 24(a) shows the overall microstructure of the specimen after the creep test. Many voids and cracks can be observed mainly along the grain boundaries. The size of voids and cracks may be slightly exaggerated due to the chemical etching. The compression axis is indicated by two arrowheads. Figure 24(b) is a high magnification micrograph taken in the middle of the specimen shown in Figure 24(a), which substantiates that most of the voids and cracks are preferentially located at those grain boundaries, which are relatively parallel to the

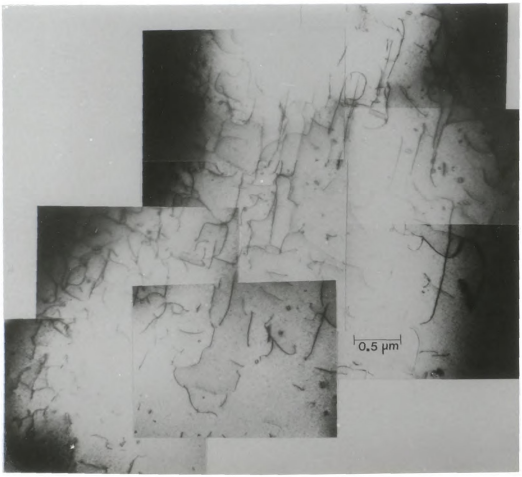

Figure 23. TEM micrograph of $TaC_{0.99}$ crept at 1300 °C and 300 MPa.

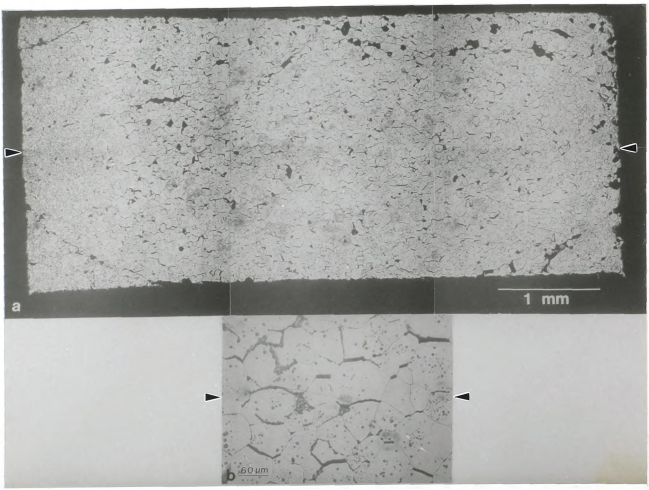

Figure 24. Optical micrographs of $TaC_{0.99}$ crept at 1500 °C and 60 MPa: (a) low magnification image, (b) high magnification image.

compression axis. Some of the voids and cracks seem to have formed by the interconnection of small pores in the grain boundaries. A few wedge cracks were also seen at three grain junctions. The formation of the voids and cracks at grain boundaries suggests that the grain boundary sliding may have occurred during creep deformation.

Dislocation structures in $TaC_{0.99}$ specimens crept at 1500 °C under a stress of about 60 MPa are presented in Figure 25 to Figure 36. Figure 25 shows a subboundary, and individual dislocations. Figure 26 shows a higher magnification micrograph of the subboundary presented in Figure 25. The subboundary is a tilt boundary, which is composed of a set of straight parallel dislocations. Figure 27 shows another subboundary which seems to be less perfect than the one presented in Figure 25. The spacing between dislocations forming the subboundary is much larger than that of the subboundary shown in Figure 26. A few dislocations of the subboundary appear to interact with the individual dislocations inside the subgrain. At higher magnification it becomes evident that the dislocations which comprise the boundary have many kinks or jogs (Figure 28).

Another TEM foil of crept $TaC_{0.99}$ shows a well-defined twist boundary, which is composed of two sets of long dislocations (Figure 29). The dislocations forming the twist boundary are curved along the boundary which implies that the boundary plane is distorted. Figure 30 shows a higher magnification micrograph of the twist boundary now imaged with a different g vector, $\mathbf{g}=[0\bar{2}\bar{2}]$. It can be noticed that one set of boundary dislocations is out of contrast according to the diffraction condition. The Burgers vector of these dislocations is probably of type

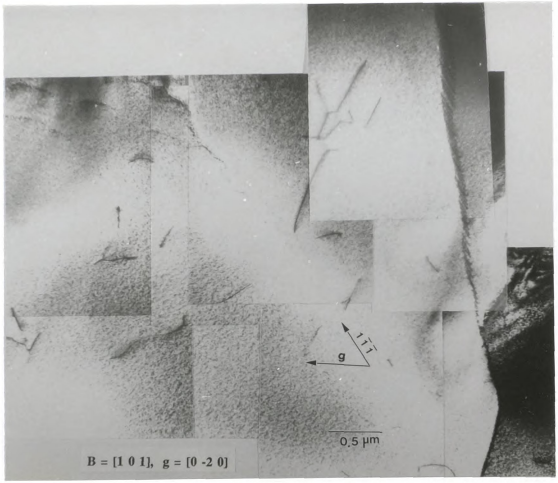

Figure 25.TEM micrograph of $TaC_{0.99}$ crept at 1500 °C and 60 MPa: B; beam direction, g; diffraction vector.

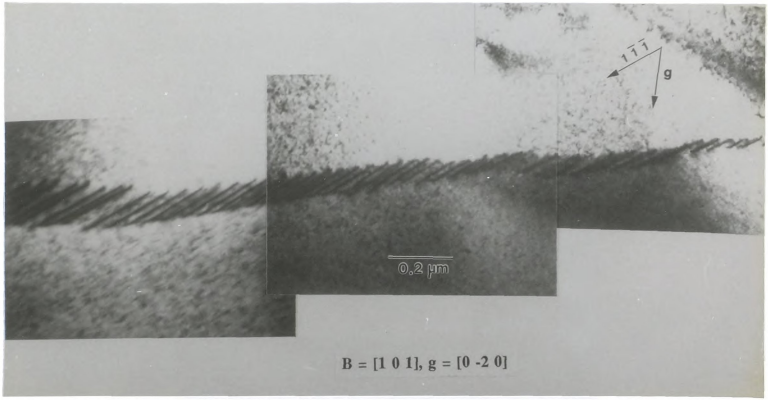

Figure 26. High magnification micrograph of the subboundary shown in Figure 25: B; beam direction, g; diffraction vector.

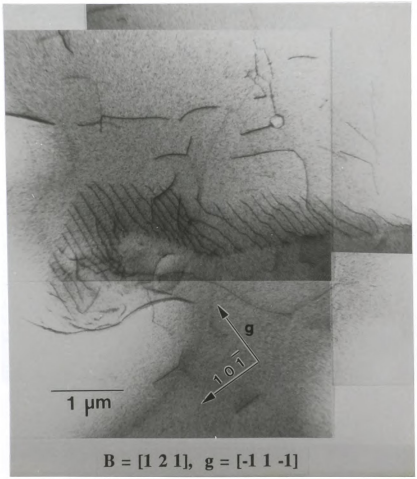

Figure 27. TEM micrograph of crept $TaC_{0.99}$ showing a subboundary and individual dislocations: B; beam direction, g; diffraction vector.

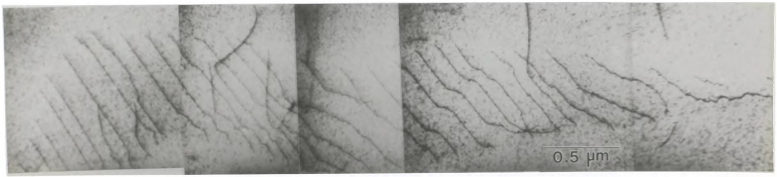

Figure 28. High magnification micrograph of the subboundary shown in Figure 27.

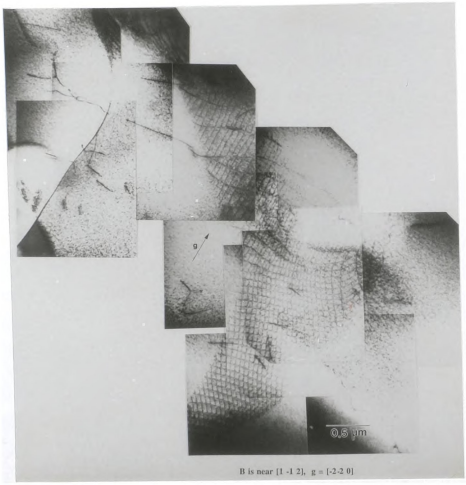

Figure 29. TEM micrograph of crept $TaC_{0.99}$ showing a twist boundary: B; beam direction, g; diffraction vector.

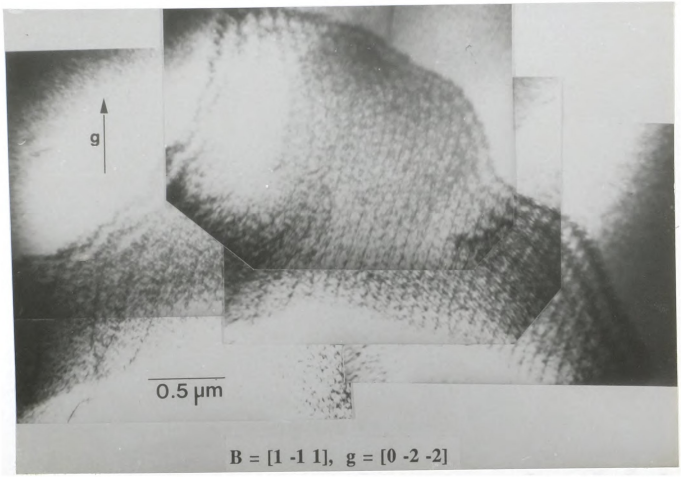

Figure 30. High magnification micrograph of the twist boundary shown in Figure 29: B; beam direction, g; diffraction vector.

$a/2<01\bar{1}>$.

In another area of the specimen, a number of short and straight individual dislocations can be observed (Figure 31). It can also be noticed that some of long dislocations were pinned by these short dislocations, and that the curved dislocation segments were formed between the pinned-points. A Burgers vector analysis of these dislocations is presented in Figure 32. The dislocation contrast of three types of dislocations, denoted as 1, 2 in Figure 32(a) and 3 in Figure 32(c), is listed in Table 8.

Table 8. Dislocation contrast of individual dislocations.

g	$[\bar{1}1\bar{1}]$	$[\bar{2}00]$	$[11\bar{1}]$	[200]
1	Vi	Vi	Inv	Vi
2	Vi	Inv	Vi	Inv
3	Inv	Vi	Vi	Vi

where, Vi and Inv denote that the dislocations are visible and invisible, respectively.

From the results, the Burgers vectors of dislocations of type 1, 2 and 3 were found to be $a/2\ [1\bar{1}0]$, $a/2[01\bar{1}]$ and $a/2[10\bar{1}]$, respectively. Analysis of the line directions and Burgers vectors of three types of dislocations results that they are all mixed type dislocations.

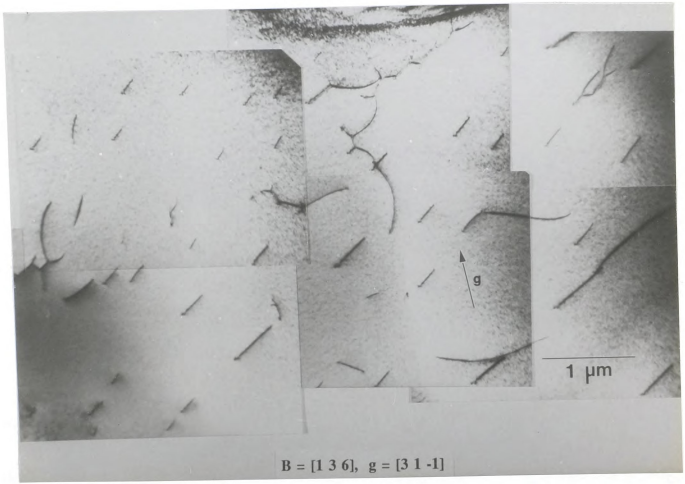

Figure 31. TEM micrograph of crept $TaC_{0.99}$ showing individual dislocations: B; beam direction, g;diffraction vector.

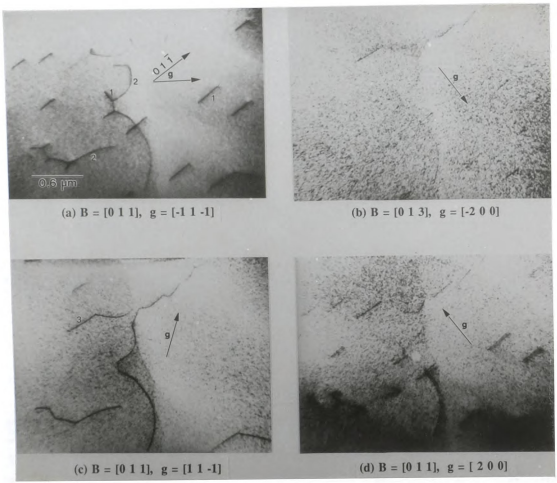

Figure 32. Burgers vector analysis of dislocations of type 1,2 and 3: B; beam direction, g;diffraction vector.

Figure 33(a) shows a subboundary and hexagonal dislocation networks. The high magnification micrograph of a part of the subboundary is shown in Figure 33(b). A set of dislocations comprising the subboundary appears to be out of contrast (Figure 33(b)). A Burgers vector analysis of dislocations in the hexagonal networks is given in Figure 34. The resulting dislocation contrast (Visible or Invisible) of two types of dislocations, denoted as 1 and 2 in Figure 34(a), is listed in Table 9.

Table 9. Dislocation contrast of dislocations in hexagonal networks.

g	$[\bar{1}3\bar{1}1]$	$[0\bar{2}20]$	$[\bar{2}202]$	$[\bar{1}\bar{1}11]$
1	Vi	Inv	Vi	Vi
2	Vi	Vi	Vi	Inv

From the above result, the Burgers vectors of the dislocations type 1 and 2 should be a/2 $[10\bar{1}]$ and a/2 $[1\bar{1}0]$, respectively. Because of their orientation both types of dislocations are mixed dislocations.

Figure 35 shows TEM micrographs of a Burger vector analysis performed on another dislocation networks. Two types of dislocations consisting the networks are denoted as 1 and 2 (Figure 35(a)). The summary of dislocation contrast of these dislocations is presented in Table 10. The Burgers vector of dislocation type 1 and 2 are found to be a/2 $[01\bar{1}]$ and a/2 $[1\bar{1}0]$, respectively. Again, these dislocations are mixed

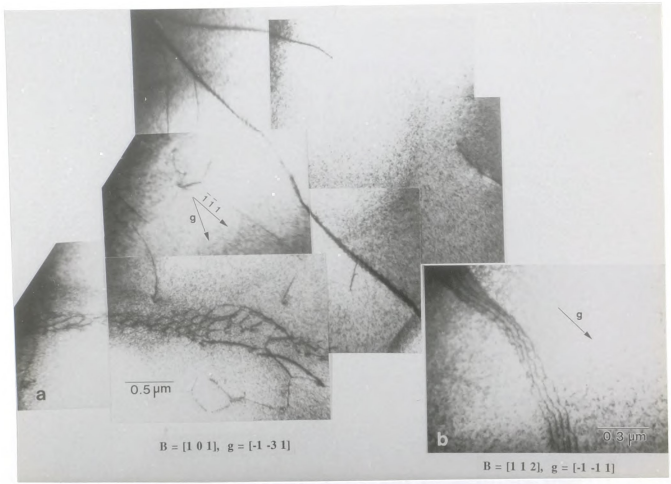

Figure 33. TEM micrographs of crept $TaC_{0.99}$: (a) a subboundary and hexagonal networks, (b) higher magnification image of the subboundary. B; beam direction, g;diffraction vector.

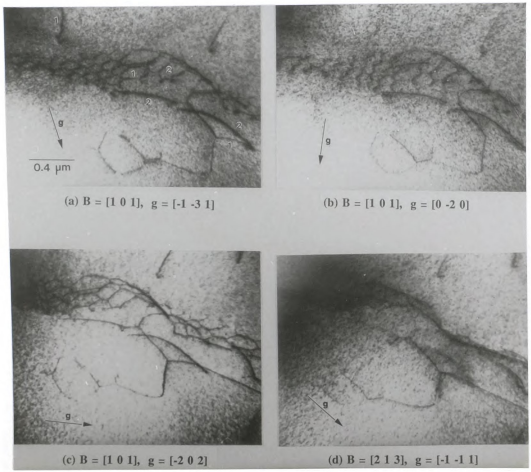

Figure 34. Burgers vector analysis of the hexagonal networks: B; beam direction, g;diffraction vector.

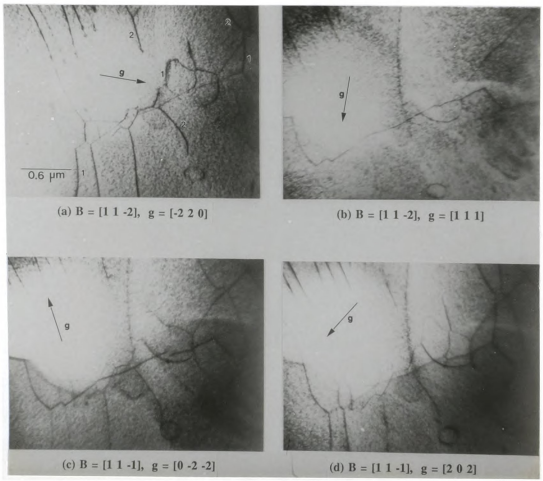

Figure 35. Burgers vector analysis of the dislocation networks: B; beam direction, g;diffraction vector.

type dislocations.

Table 10. Dislocation contrast of dislocations in networks.

g	[$\bar{2}$20]	[111]	[0$\bar{2}\bar{2}$]	[202]
1	Vi	Inv	Inv	Vi
2	Vi	Inv	Vi	Vi

Finally, Figure 36 shows a grain boundary and a subboundary which composed of two sets of dislocations intersecting each other. A misorientation angle across this subboundary was measured using the Kikuchi pattern method as described in Section 3.3. The calculated value of the misorientation angle was about 0.6 °.

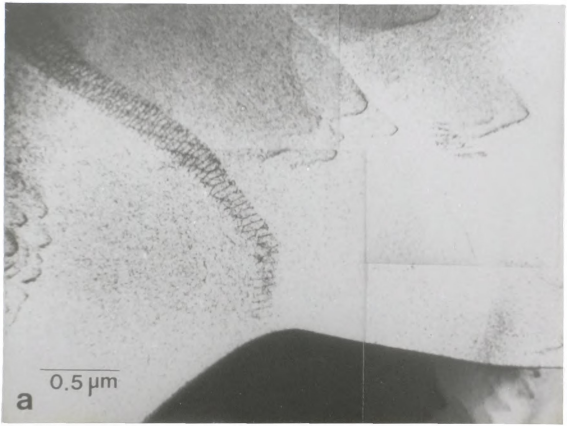

Figure 36. TEM micrograph of crept $TaC_{0.99}$ showing a subboundary and a grain boundary.

4.4 DISCUSSION

As discussed in Section 2.3, it is possible to elucidate the controlling-mechanisms of creep by comparing the kinetic data of a creep experiment with the theoretical steady-state creep models. Two important kinetic data are required to be examined for that purpose. These are the value of the stress exponent and the activation energy for creep. It is also important to know the creep conditions, i.e. the applied stress and temperature, because the operative creep mechanisms may change with these two variables.

The temperatures employed for the present creep tests were about 1400 °C and 1500 °C. These correspond to the homologous temperatures of about 0.39 T_m and 0.42 T_m ($T_m \approx 3983$ °C), respectively. Thus, the present investigation can be considered as intermediate-temperature creep. Since no data exist for the temperature dependency of the shear modulus of $TaC_{0.99}$, the value of shear modulus of $TaC_{0.99}$ at 1500 °C can only be estimated roughly by using a rule of thumb, i.e. the value of shear modulus at the melting point is one half of the value at absolute zero temperature. Using the value of shear modulus of $TaC_{0.99}$ at room temperature (≈216 GPa), the shear modulus(μ) of $TaC_{0.99}$ at 1500 °C is estimated to be about 177 GPa. The applied stresses for the present creep experiments were about 105 MPa and 170 MPa. These correspond to approximately 6×10^{-4} μ and 9.6×10^{-4} μ, respectively. Thus, the creep conditions applied for the present investigation are in the regime where

power-law creep behavior is usually observed for many metals and alloys.

From the result of the creep tests of $TaC_{0.99}$ polycrystals, the calculated value of the stress exponent was close to 2. As discussed in Section 2.3, when the creep is controlled by diffusional creep, the value of stress exponent is 1. The stress exponents of dislocation creep mechanisms are about 3 and 5 depending on whether the creep is controlled by the dislocation glide or the dislocation climb. Thus, the value of the stress exponent obtained in the present creep study lies in the regime between diffusional creep and the dislocation glide-controlled creep. This suggests that more than one mechanism may have contributed to the creep of $TaC_{0.99}$ under the applied conditions.

It has been known that relations exist between the activation energy of self-diffusion and the activation energy for creep at high temperatures. The value of activation energy for carbon diffusion in TaC was reported as about 360 KJ/mol in the temperature range between 1800 °C and 2700 °C [102], and about 497 KJ/mol between 2360 °C and 2960 °C [103]. The value of activation energy for Ta diffusion in TaC is not known, but it is considered to be higher than that for C diffusion. Within experimental error, the value of activation energy for creep obtained in the present study was about 150 KJ/mol. Although the value of activation energy for diffusion generally decreases with decreasing temperature, the obtained value of activation energy for creep is thought to be too low to match with the values of activation energy for either C or Ta diffusion in TaC. Thus, the low value of activation energy for creep suggests that creep of $TaC_{0.99}$ under the present creep conditions may not be controlled by

diffusion mechanisms, which is also likely since the temperatures employed for the present creep study are lower than 0.5 T_m.

An important aspect of the creep of $TaC_{0.99}$ under the present creep conditions is the formation of voids and cracks along the grain boundaries as observed in Figure 6. Gifkins [104] and Chen et al. [105] proposed the mechanisms for the formation of intergranular voids or cracks. Although the details of two mechanisms are different, a necessary prerequisite for both mechanisms is grain boundary sliding. Chang and Grant [106] also proposed models for the formation of various shapes of wedge cracks due to grain boundary sliding which were also observed in this investigation. Thus, the intergranular voids and cracks formed during creep of $TaC_{0.99}$ may be due to grain boundary sliding. The formation of intergranular voids or cracks by grain boundary sliding has also been observed for a number of crept ceramics, e.g. MgO [107], Si_3N_4 [108] and ThO_2 [109].

Langdon et al. [110] reviewed the experimental data on grain boundary sliding in metals and noticed that grain boundary sliding can make a significant contribution to the total creep deformation. They found that the value of the stress exponent for grain boundary sliding was lower than the stress exponent for the overall creep process and the ratio of activation energy for grain boundary sliding and activation energy of lattice self-diffusion ranges from about 0.5 to 1. Although the relative contribution of grain boundary sliding to the observed creep behavior of $TaC_{0.99}$ is not known, the obtained values of stress exponent and activation energy for creep of $TaC_{0.99}$ at intermediate temperatures indicate that creep is probably affected by grain boundary sliding.

Although TEM micrographs could not show the overall substructures of crept $TaC_{0.99}$ specimens, some of important features of dislocation structure were evident. The dislocation structure of $TaC_{0.99}$ crept at 1300 °C and 300 MPa reveals extensive dislocation interactions during the creep test (Figure 23). The microstructure also shows numerous dislocation loops which result from the pinch-off process of dislocation dipoles. This suggests that recovery under these conditions occurs by annihilation of dislocations of opposite sign. However, no conclusive evidence of dynamic recovery processes such as cell or subgrain formations were observed.

The dislocation structure of $TaC_{0.99}$ specimen crept at 1500 °C and 60 MPa consists mainly of subboundaries, dislocation networks and individual dislocations. These features indicate that the dislocation glide activity at 1500 °C is stronger than that in the specimen crept at 1300 °C. A number of TEM micrographs (e.g. Figure 25, 31, 35, 36) reveal interactions between dislocations occurs during creep. While the formation of hexagonal dislocation networks and subboundaries (Figure 33) may have involved also dislocation climb, the prominent features of the microstructure under these conditions seem to be due to dislocation glide and dislocation interactions.

The results of the Burgers vector analysis of the dislocations formed during the creep test substantiate that the slip system of $TaC_{0.99}$ at 1500 °C is $\{111\}\langle 1\bar{1}0\rangle$. This result is consistent with earlier reports [25]. The characteristics of the dislocations formed during the creep test are quite different from those of dislocations formed during the room temperature deformation (Chapter 3). Most dislocations formed during

the creep test (e.g. Figure 31) appear to have no preferential orientation in contrast to the long screw dislocations formed during the indentation-deformation at room temperature. The main reason for these differences is probably due to the fact that dislocation glide over the Peierls barriers becomes easier at elevated temperatures due to thermal activation.

4.4 SUMMARY

1. From the results on creep tests at intermediate temperatures (1400-1500 °C, ~ 0.4 T_m) and stresses (105-170 MPa), the values of the stress exponent (n) and activation energy (Q_c) for power-law creep of $TaC_{0.99}$ were found to be $n \approx 1.8$ and $Q_c \approx 150$ KJ/mol.

2. The low activation energy and the low stress exponent suggest that the creep of $TaC_{0.99}$ at intermediate temperatures is mainly controlled by grain boundary sliding. This is further supported by observation of void formation.

3. The observation of dislocation interaction in the crystal interior suggests that dislocation glide may act as a minor contributing mechanism during creep. TEM investigation also reveals the formation of subboundaries and dislocation networks.

4. Most dislocations formed during creep of $TaC_{0.99}$ have no preferential orientation, in contrast to dislocations formed at low temperatures. This is probably due to thermally activated dislocation motion at elevated temperatures.

CHAPTER 5

PROCESSING OF C-TaC COMPOSITES

5.1 INTRODUCTION

In recent years the fiber reinforced ceramic matrix composites have received considerable attentions primarily because of their potential applications as a structural material at elevated temperatures. One of main advantages of ceramics is their retention of strength at high temperatures and low density as compared with metals. The main disadvantage is their low fracture toughness or resistance to crack propagation. The low toughness is a consequence of very limited dislocation motion in ceramics. Because of their low toughness, ceramics are susceptible to damage by thermal and mechanical shock. Also the strength of ceramics can be drastically reduced by flaws or damages introduced during fabrication or in service. Thus the main incentive for developing the fiber reinforced ceramic matrix composites is to improve their toughness as well as their strength.

In general, the fiber reinforced ceramic matrix composites can be divided into two basic types, the system based on short fibers or whiskers and the continuous fibers. The composites containing short random fibers or whiskers are developed mainly for increasing the toughness of ceramic matrices. The strength of these composites are frequently lower than

unreinforced matrix due to the combined effects of stress concentration and residual thermal stresses. An improvement in strength has been reported only for a few systems, for example SiC whisker reinforced Al_2O_3 [111].

A greater increase in strength and toughness of ceramic matrix composites can be obtained by reinforcing ceramics with continuous aligned fibers. In continuous fiber system the stress concentration at the ends of fibers is minimized and fibers have the major role as the load bearing component while matrix has the secondary role of providing a load transfer medium. The further advantage is that higher volume fractions of fiber can be obtained as compared to short fiber system. Thus the fibers are required to have high strength and high stiffness at elevated temperatures in order to obtain the composite strengthening effect. The work on carbon fiber and silicon carbide fiber reinforced glass and glass-ceramic composites demonstrated the great potential for this type of composite, both in terms of high strength and fracture toughness [112-114].

Several important toughening mechanisms have been considered for ceramic matrix composites. These include load transfer from a matrix to fibers, prestressing of the matrix due to differences in the coefficients of thermal expansion of fibers and the matrix, crack impediment by fibers, microcracking of the matrix, crack deflection and fiber pull-out [115]. It has been found that typically, in a given composite, combinations of the aforementioned toughening mechanisms are operative. The relative contributions of individual toughening mechanisms generally depend on interfacial properties, microstructure of

composites, and the elastic constants of fibers and matrix.

The mechanical properties and behaviors of composites critically depend on the bond strength of an interface between the fiber and the matrix. In contrast to polymer and metal matrix composites, the interfacial bond strength of ceramic matrix composites often need to be low in order to improve their toughness but also need to be high enough to improve their strength. Therefore, it is important to control the interfacial bond strength in order to obtain the optimum combination of toughness and strength in fiber reinforced ceramic composites.

The basic requirements of materials which can be used in fiber reinforced ceramic composites are high melting points and high strength often coupled with low density. The other important requirements which must be considered in choosing a particular fiber-matrix system is the compatibilities between the two components at elevated temperatures. Three types of compatibility between fiber and matrix are need to be satisfied in order to form a successful composite. These are chemical compatibility, thermal expansion mismatch and relative elastic modulus of the fiber and matrix [116].

Among fiber reinforced ceramic composites, the glass and glass ceramic matrices are not very attractive for high temperature applications because the matrices loose their strength at relatively low temperature. The potential matrix materials for higher temperature applications include mainly the refractory ceramics such as carbides, oxides, nitrides and borides. Although numerous potential composite systems can be selected from the various refractory ceramics, the number of practical systems is limited owing to the fibers that are available. At present the

important high performance fibers commercially available are carbon, silicon carbide and alumina fibers. Alumina and silicon carbide fibers are more oxidation resistant than carbon fibers and may be used without oxidation barrier. But, in non-oxidizing atmosphere, carbon fibers provide the highest temperature capability.

Various fabrication techniques of fiber reinforced ceramics have been developed, and a number of reviews on this subject have been published [116-119]. Because of the refractoriness of ceramic matrices the conventional fabrication techniques for ceramic matrix composites employ powder processing methods. Three common problems encountered from powder processing of ceramic matrix composites have been reported by Rice [118]. First, the fibers can be damaged by refractory hard matrix powders. Second, a large porosity at the fiber and matrix interface can be formed due to insufficient formability of the refractory matrix around the fibers. Third, the chemical interaction between the fiber and the matrix increases due to higher processing temperature for more refractory matrices.

In general, a fiber reinforced ceramic can be fabricated by using a two-stage process [116]. The first stage is to incorporate the reinforcing fibers into an unreinforced matrix and the second stage involves the consolidation of the matrix at high temperatures. The general microstructural requirements for high strength of the resulting fiber reinforced composites are high volume fraction of fibers, uniform distribution of fibers, high density and homogeneous ceramic matrix [117].

For short fiber or whisker reinforced composites, the

reinforcements can be readily mixed with the matrix powder or slurry. Uniform dispersion of the reinforcements becomes more difficult as the volume fraction and length of reinforcements are increased and the clustering of reinforcements may occur. In case of continuous fiber composites, the most common technique of fiber incorporation is the slurry infiltration process. In the slurry infiltration process fibers are impregnated with the matrix by passing through a slurry of the matrix to produce a pre-preg sheet. The pre-preg sheets are then laid into desired configuration followed by binder burnout and consolidation processing. The slurry usually contains the carrier liquid and an organic binder in addition to the matrix powder. The volume fraction of fibers in a composite can be controlled by adjusting the composition of the slurry.

The main goal of the consolidation stage is to produce a low porosity matrix while damaging the fibers as little as possible. The various consolidation processing techniques, such as sintering, hot pressing and hot isostatic pressing, which have been applied for unreinforced ceramics can also be applied to ceramic matrix composites. Since the refractory ceramics are usually difficult to sinter to obtain full density and furthermore the fibers tend to inhibit the densification, ceramic matrix composites produced by sintering often exhibit poor mechanical performance due to high porosity. The most widely used technique of consolidating fiber reinforced ceramics is hot pressing. For example, carbon and silicon carbide fiber reinforced glass and glass ceramic composites has been successfully fabricated by using the slurry infiltration process and hot pressing [112-114].

The hot isostatic pressing (HIP) is a relatively new technique in

which high isostatic gas pressure is applied to a powder part or compact at elevated temperatures to produce a material with near theoretical density [120-122]. An improvement in mechanical properties is reported for hot isostatically pressed ceramic matrix composites, for example SiC whisker reinforced alumina matrix [123] and SiC whisker reinforced silicon nitride matrix [124] composites. The main advantage of the HIP process is that superior quality of a product can be obtained owing to the combined effects of low porosity and uniform and fine grained microstructures. A further advantage is its ability to fabricate complex shapes. The disadvantages of the HIP process are that it requires rather complicated preparation and the processing cost is relatively high.

The other fabrication technique of fiber reinforced ceramic matrix composites include chemical vapor deposition (CVD) infiltration and sol-gel techniques. Silicon carbide fiber reinforced SiC matrix and Si_3N_4 matrix composites were fabricated by CVD infiltration technique [125]. Fabrication of Al_2O_3 and SiC fiber reinforced Alumina matrix composites by using sol-gel technique was also reported [126]. Although these fabrication techniques have been most recently developed, at present these are less commonly used due to the shortcomings such as high porosity and low yield.

As mentioned earlier in a previous chapter the transition metal monocarbides possess very attractive properties that can be used as a matrix of composite materials for high temperature structural applications. However, only very few investigations on fiber reinforced transition metal monocarbides have been reported. For example, short graphite fiber reinforced niobium carbide composites were produced by

sintering of cold compacted composites, and also by the slurry infiltration process followed by hot pressing technique [127,128]. A carbon fiber reinforced tantalum carbide matrix composite was fabricated by using a three-step chemical reaction process [129]. In this processing, the yield was low and the residual porosity of the composite was 5 to 10 percent after multiple impregnations. Detailed information on these composites, for example interfacial properties and microstructures of the composites, cannot be obtained because of patented work.

In the present investigation, a continuous carbon fiber and stoichiometric tantalum carbide matrix composite system was studied as a potential material for high temperature structural applications. As described earlier TaC possesses attractive properties for high temperature applications including the highest melting point, high strength, high stiffness and high temperature ductile behavior similar to f.c.c. metals. As a reinforcement phase C-fibers exhibit high specific strength and stiffness at high temperatures. Because the stoichiometric TaC matrix is already saturated with carbon, the diffusion of carbon between two components is not expected to occur at high temperatures. Therefore, the principal advantage of C-TaC system will be its thermal and compositional stability at high temperatures. In the present study carbon fibers were incorporated into a TaC matrix by using either a cold compaction process or a slurry infiltration and cold compaction process. Hot isostatic pressing (HIP) is used as a hot consolidation technique. The nature of the interface between carbon fibers and the tantalum carbide matrix of the composites was investigated. The problems associated with the processing and the possible solutions will be discussed.

5.2 EXPERIMENTAL PROCEDURE

5.2.1 Characteristics of starting materials

Two different types of TaC powder and carbon fibers were employed for producing C-fiber reinforced TaC composites. The important characteristics of these materials are summarized in Table 1. A major difference between type A and type B of TaC powder was the initial particle size. In both types the carbon fibers were polyacrylonitrile (PAN)-based high modulus and high strength type carbon fibers. AS-4 fibers have a larger diameter and higher tensile strength than those of APOLLO™ 55 fibers. But Young's modulus of APOLLO ™ 55 fibers was higher than that of AS-4 fibers.

The morphology of TaC powders and C-fibers were observed by a scanning electron microscope (JEOL model JSM-35C) and these are shown in Figure 37. As can be seen in Figure 37(a) and (c), the shape of type A and type B TaC powder is angular and rounded respectively. In Figure 37(b) the surface of APOLLO™ 55 fibers shows many aligned ridges which are typical of high modulus carbon fibers [130]. On the other hand, the surface of AS-4 fibers in Figure 37(d) is very smooth.

Two kinds of C-TaC composites were fabricated using different carbon fibers and TaC powder. APOLLO™ 55 fibers were incorporated into type A powders, and AS-4 fibers were used with type B powders.

Table 11. Characteristics of as-received TaC powder and C-fiber.

TaC powder

	Type A	Type B
C/Ta ratio	0.99	0.99
Particle size(μm)	< 45	0.5 - 1.5
Impurity(%)	Al 0.01, Nb 0.05, B<0.001 Ni 0.005, Co 0.01-0.06 Si 0.01, Fe 0.01, Ti 0.005	free C 0.08, Ca 0.003 Fe 0.007, Nb 0.13 Si 0.001, Ti 0.001
Vendor	Cerac Inc.	Hermann C. Starck

Carbon fiber

	APOLLO™ 55-500	AS-4
Tensile strength(GPa)	3.45	3.79
Young's modulus(GPa)	379	235
Ultimate elongation(%)	0.91	1.53
Filament diameter(μm)	5	8
Vendor	Fiber Materials Inc.	Hercules Inc.

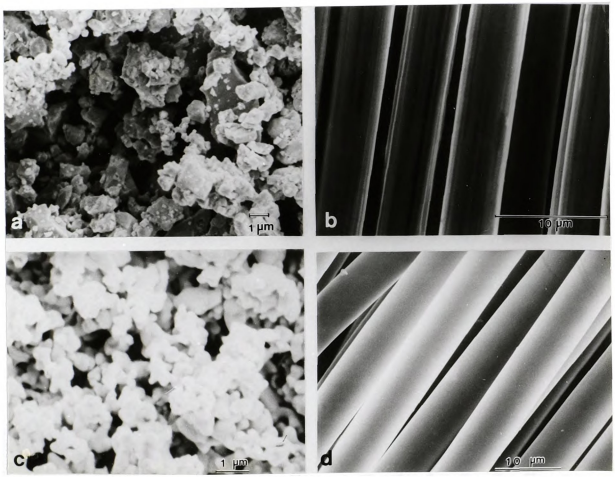

Figure 37. Scanning electron micrographs of as-received TaC powders and carbon fibers: (a) Type A powder, (b) APOLLO™ 55 fiber, (c)Type B powder, (d) AS-4 fiber

5.2.2 Fabrication of C-TaC composites

Two different processing routes were designed to produce C-TaC composite specimens. The block diagrams of each processing route are shown in Figure 38. The main purpose of the processing route #1 was to produce a composite specimen which can be used to study the characteristics of an interface between C-fibers and TaC matrix. So, in the processing route #1, the as-received C-fiber tows were used without large effort in achieving exact alignments and separations of an individual filament of fibers. Carbon fibers and TaC powder used for the first processing route were APOLLO^{TM} 55 fibers and type A powder respectively.

For the processing route #1 in Figure 38, HIP containers were fabricated from a Ta tube, Ta sheet and Ta rod. The inner diameter and the wall thickness of a Ta tube was about 19.5 mm and 3 mm respectively. The thickness of a Ta sheet was about 1.5 mm and the diameter of a Ta rod was about 3.2 mm. The tube was cut into three pieces and the length of each piece was approximately 56 mm. Ta discs with a diameter of 19.5 mm were machined out of a Ta sheet, and these were used as top lids, bottom lids, top and bottom spacers. Each disc for a top lid was drilled at the center to make a hole with a diameter of 3.2 mm. A Ta tube stem of about 30 mm in length and 3.2mm in diameter was made from the Ta rod by drilling and was inserted into a hole of a top lid. Two parts are then tungsten inert gas (TIG)- welded in an Ar gas atmosphere. A bottom lid was press- fitted into the Ta tube and also TIG- welded. Some of Ta

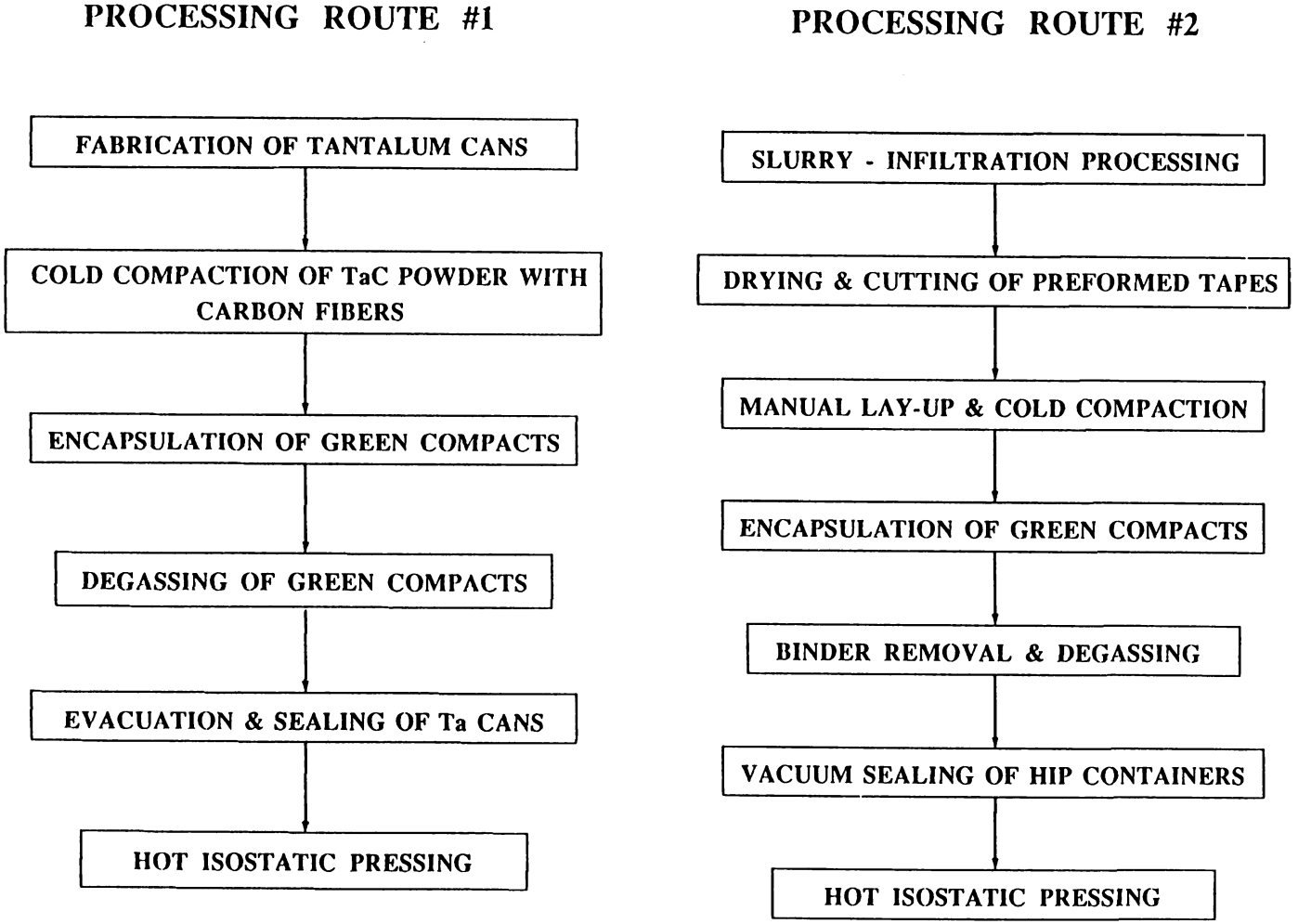

Figure 38. The block diagrams of two C-TaC composite processing routes.

discs were machined to have 8 notches around the periphery and used as the top spacers. For the bottom spacers, some of discs are chamfered around the edges. Some of these fabricated parts of a HIP container are shown in Figure 39(a). The reasons for using these spacers are that the spacers promote a uniform deformation of the HIP container and reduce the possibility of early leakage of the container during hot isostatic processing.

The green compacts of C-TaC composites were made as follows. First, a small amount of TaC powder was added in a cylindrical die and hand-pressed with a plunger after tapping the powder. The die and plunger were made from heat treated tool steel. The dimensions of the cylindrical body of the die were about 90 mm in length, 19.2 mm in inner diameter and 55 mm in outside diameter. Above the TaC powder compact, 12 K tows of carbon fibers were spread and laid manually. A small amount of TaC powder was added to the fibers and pressed manually after tapping. By repeating the above procedure, several layers of carbon fibers were embedded in TaC powder. Then, this sample in the die was cold-pressed by using a MTS machine (Model 810) equipped with a vacuum furnace. The maximum pressure applied during the compaction was 325 MPa. After the cold compaction was completed, the green compact was carefully removed from the die. The typical dimensions of the green compacts are 19.2 mm in diameter and 42 mm in length.

A green compact was then carefully put in a bottom-welded Ta HIP container with a spacer. A molybdenum foil of 0.07 mm in thickness was inserted as a diffusion barrier between the green compact and the Ta container. After three top spacers were dropped in, a top lid was press

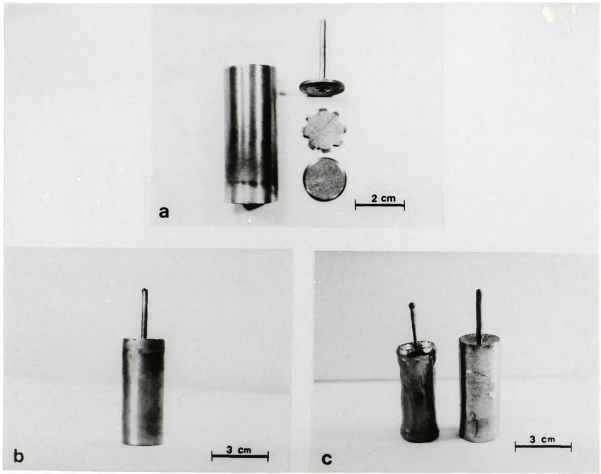

Figure 39. Photographs of Ta HIP containers: (a) some parts of a HIP container (a Ta can, top lid, top and bottom spacer), (b) a vacuum-sealed container before HIP, (c) HIP processed containers (left; a properly processed container, right; a leaked container).

fitted and TIG-welded with the HIP container in Ar atmosphere. The HIP containers were then leak tested with a helium leak tester. After the HIP containers successfully passed leak testing, the green composite compacts in the leak-proof HIP containers were then degassed in a vacuum furnace (CENTORR, Model M60) at a temperature of 1000 °C for 12 hours. The final vacuum was about 3×10^{-6} Torr. After the containers had cooled down, Ar gas was flushed into the vacuum furnace to fill the containers. The containers were then quickly stored in a vacuum desiccator before the vacuum sealing process. The vacuum sealing of the HIP containers was done in a zone refiner (Materials Research Corporation, Model EBZ-94) at a vacuum of about 2×10^{-6} Torr. The final vacuum sealed HIP containers before hot isostatic processing are shown in Figure 39(b).

The hot isostatic pressing was performed at Howmet Turbine Component Corporation of Whitehall, Michigan. The time, temperature and pressure profile of the HIP process for these containers is presented as HIP #1 in Figure 40. The specimens were heated up to about 700 °C in Ar atmosphere and at that temperature the Ar gas pressure started to increase. The maximum pressure of over 200 MPa was reached after 4 hours, but the pressure was lowered to about 105 MPa due to the unstable HIP furnace. The temperature and the pressure of a steady state HIP process were about 1900 °C and 105 MPa respectively.The steady state was kept for 3 hours and after that the temperature and the pressure were decreased linearly. The total time for a HIP process was about 12 hours.

The Ta containers after the HIP process are shown in Figure 39(c). Although the HIP containers had been carefully prepared, one of three

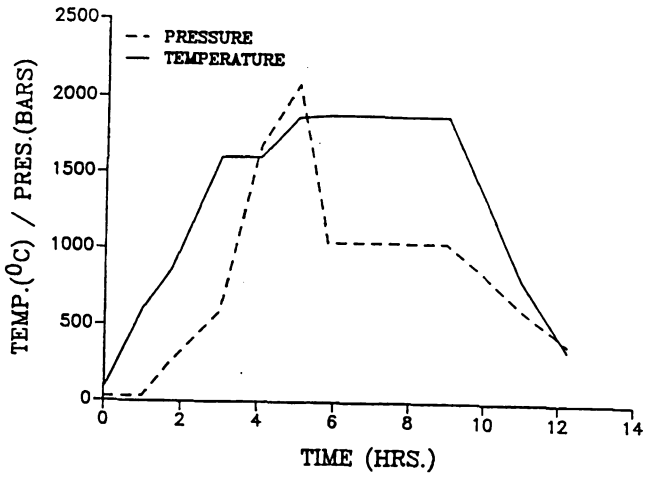

HIP #1 : TIME, TEMPERATURE, PRESSURE PROFILE

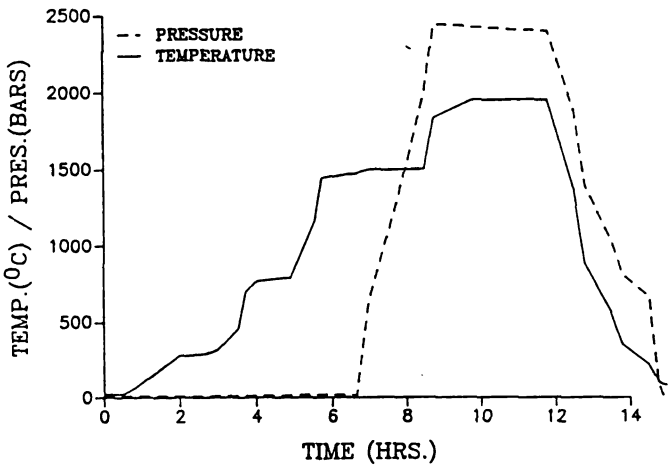

HIP #2 : TIME, TEMPERATURE, PRESSURE PROFILE

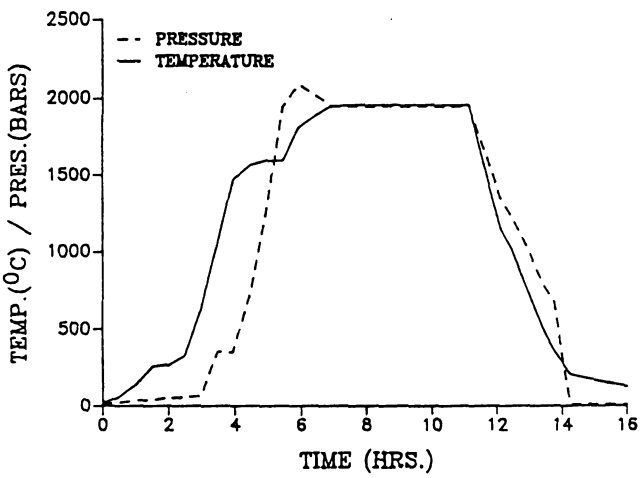

HIP #3 : TIME, TEMPERATURE, PRESSURE PROFILE

Figure 40. Time, temperature, and pressure profiles of HIP process.

HIP containers was not properly consolidated probably due to a leakage. The hot isostatically pressed containers were cut by using a low speed diamond saw (BUEHLER, ISOMET^{TM}). The microstructures of C-TaC composite specimens were studied by using an optical microscope (LECO, NEOPHOT 21) and a scanning electron microscope. The chemical analysis of the interface between carbon fibers and tantalum carbide was performed by using an auger electron spectroscope(AES) (PERKIN-ELMER, Model PH1660).

For the processing route #2 in Figure 38, carbon fibers were incorporated in a TaC matrix by the slurry-infiltration process. The carbon fibers and TaC powder used were AS-4 fibers and type B powder. The slurry was composed of about 87 wt% of TaC powder, 8 wt% of ethanol and 5 wt% of polyethylenimine. A schematic of the slurry-infiltration process is shown in Figure 41. A carbon fiber spool was held by a motor driven pulley. A 12K tow of AS-4 fibers was stretched from the spool and passed through a number of Teflon rollers. While the fibers were passing through the rollers, they were spread uniformly by the vibration of air from a loud speaker which was connected to an amplifier and a function generator. The volume of the amplifier was adjusted to obtain the optimum amount of spreading. The spreaded carbon fibers were then passed through a matrix slurry tank and coated with the slurry. The infiltrated carbon fibers were wound manually to a spool which was wrapped with a Teflon film to prevent it from sticking. The pre-preg tapes were dried in air for 14 hours. The typical thickness of the pre-preg tapes was 0.5-0.7 mm. These composite tapes were cut to 55 mm length.

The green compacts of C-TaC composites were made by cold

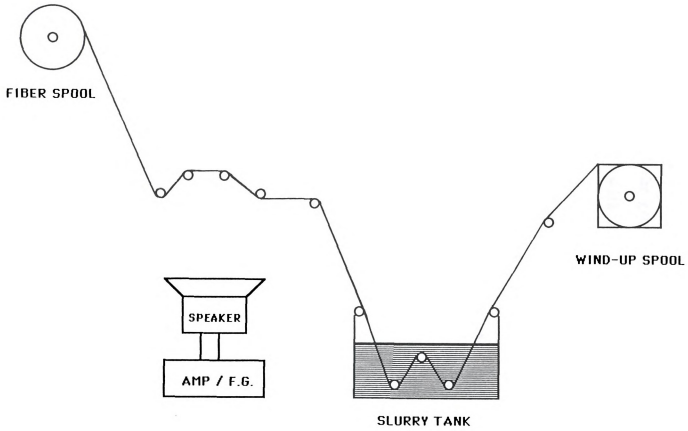

Figure 41. Schematic of slurry infiltration process.

pressing in a low carbon steel die. About fifty pre-preg tapes with a thin layer of TaC powder between each tape were stacked inside the die. The cold pressing was performed by using a hydraulic press (TINIUS OLSEN, Willow grove, Pennsylvania) with the maximum applied pressure of about 10.6 MPa. The dimensions of the green compacts were 70 mm × 30 mm × 30 mm. The green compacts with Mo foils and Nb spacers were then carefully placed in Nb HIP containers which were purchased from Advanced Fusion of Tracy, California. The photographs of a Nb HIP container before the HIP process are shown in Figure 42(a) and (b). The thickness of Nb sheets from which the containers and spacers were made was about 0.36 mm. After the top lids of HIP containers had been TIG-welded in Ar atmosphere, the Nb containers were heated at 500 °C for 4 hours to remove the binder and then degassed at 1000 °C for 12 hours in a vacuum furnace. The degassed containers were filled with Ar gas and the top stems of the containers were covered by rubber bulbs. The vacuum sealing of the HIP containers was carried out with an electron beam welding machine at Howmet Corp.

The time, temperature and pressure profile of a HIP processing for the above specimens, HIP #2, is shown in Figure 40. The Ar gas pressure was applied after the temperature reached 1500 °C and the temperature and pressure of the steady state processing during 3 hours were about 1950 °C and 242 MPa. The Nb container after the HIP process is shown in Figure 42(c) and (d). After HIPing the containers were cut by using a SiC cutting wheel and the composite samples were optically inspected. After inspection, the samples were found to have low density. So, these composite samples were again vacuum-encapsulated in Nb containers for

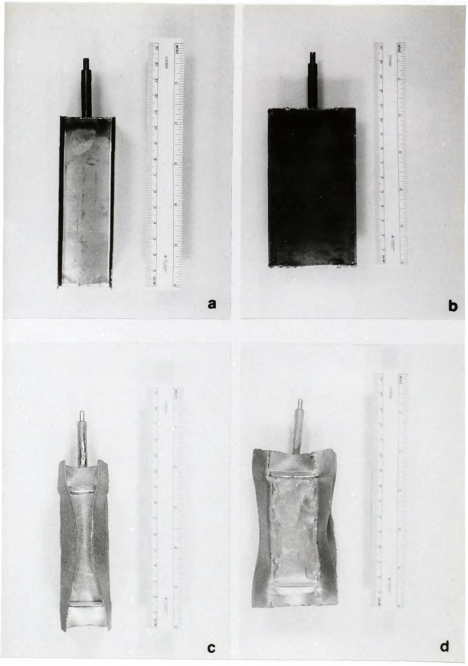

Figure 42. Photographs of niobium HIP containers: (a), (b) a side and front view of a Nb container before HIP, (c), (d) a side and front view of a Nb container after HIP respectively.

the second HIP process similar to the previous procedure. But, this time, the outside of the containers were covered by Mo foils to prevent the carburization from the HIP furnace, and no Nb spacers were inserted in the containers. The profile of a HIP process for these specimens is presented as HIP #3 in Figure 40. The temperature and the pressure at steady state were 1960 °C and 195 MPa respectively. Steady state conditions were kept for 4 hours. The composite specimens obtained after the HIP process were examined by using SEM and AES.

Some individual filaments of AS-4 fibers were coated with tantalum carbide by using a d.c. magnetron sputter coating machine of the Physics department at Michigan State University. The carbon to tantalum atomic ratio of a target, which was purchased from Cerac Inc., was 0.99. The impurity contents were 0.1-1% Nb, 0.01% Cu, 0.01% Ti, 0.001% Al, 0.001% Fe, and less than 0.001% of Ca, Mg, Mn and Si.The size of the target was about 57.5 mm in diameter and 6.35 mm thickness. The target current and voltage applied were 0.8 amperes and negative 400 volts, respectively. The plasma voltage and current were 60 volts d.c. and 4 amperes, respectively. The emitter current was 19 amperes and the deposition rate was about 3.3-3.6 Å per second. The Ar gas pressure during the coating was about 2.5×10^{-3} Torr. The carbon fibers were held in a special specimen holder machined from Al plates and were located over the TaC target. Only one side of the fibers facing the target could be coated each time. So, when the thickness of the coating had reached about 3 microns, the sample holder was flipped over and the other side was coated to the same thickness.

The coated fibers were analyzed by SEM and AES. In order to study

the effect of coating on the damage of fibers, the coated carbon fibers were embedded in a TaC matrix slurry. The composition of the slurry was the same as the one used previously. The dried composites were degassed at 500 °C for 2 hours and sintered at 1980 °C for 12 hours in a vacuum furnace. The sintered C-TaC composites were also examined by using SEM and AES.

5.3 EXPERIMENTAL RESULTS

An optical micrograph of a C-TaC composite produced via processing route #1 is shown in Figure 43(a). It can be noticed that an interface was formed between the carbon fibers and the tantalum carbide matrix. Figure 43(b) is a scanning electron micrograph of a fractured composite specimen showing the interface region, and Figure 43(c) shows the damaged carbon fibers at the interface region in the same specimen. From these SEM micrographs it appears that the interface is composed of damaged carbon fibers.

In order to find out the exact nature of the interface, chemical analysis of the interface was carried out. The results of Auger electron spectroscopy are shown in Figure 44 and Figure 45. In Figure 44, the results of elemental spot analysis of the matrix, fiber and interface region of the fractured C-TaC composite indicates that the interface is only composed of carbon. Traces of oxygen were found in TaC matrix. The tantalum elemental line scans superimposed with SEM micrographs across the interface in Figure 45 also reveal that tantalum is not present at the interface which is consistent with the previous result.

The damage of carbon fibers in the composite is most likely occurred during both cold compaction and hot isostatic pressing process. In order to investigate the damage of carbon fibers during cold compaction process, carbon fibers were embedded in TaC powders and cold pressed with pressure of about 325 MPa. The SEM micrographs

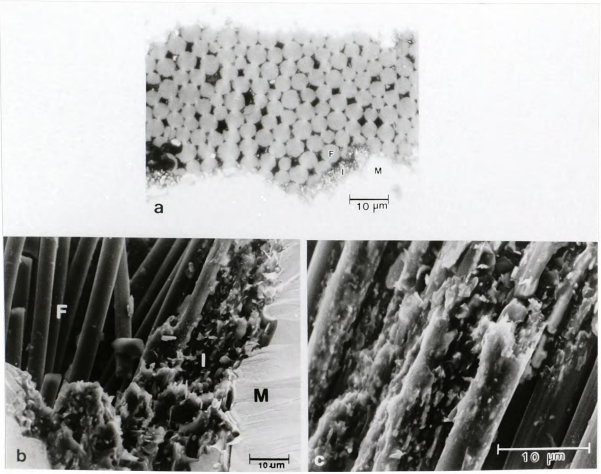

Figure 43. Optical and SEM micrographs of C-TaC composite: (a), (b) optical and SEM micrographs showing the matrix(M), interface(I) and fiber(F) region, (c) a SEM micrograph of damaged carbon fibers.

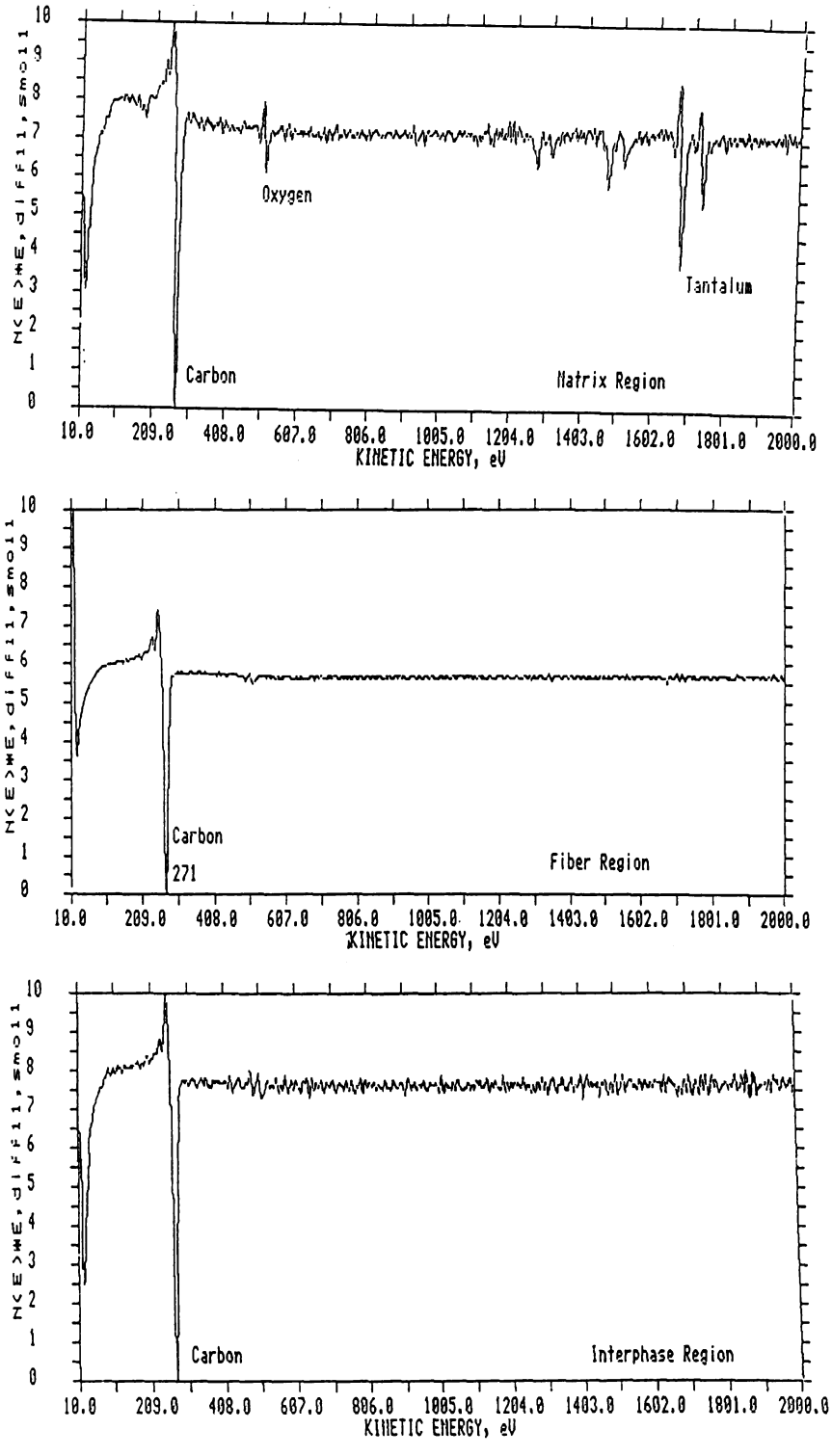

Figure 44. Auger electron spectroscopic survey of C-TaC composite.

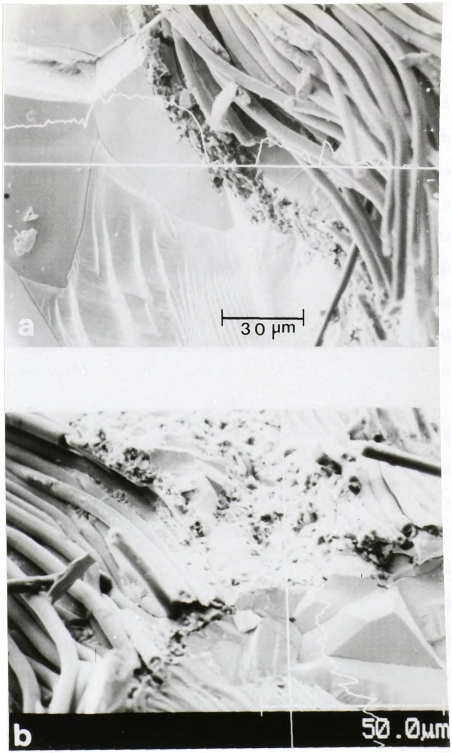

Figure 45. Tantalum line scans across the interface of C-TaC composite: (a) perpendicular to the interface, (b) parallel to the interface.

of this specimen in Figure 46 show that the damage of carbon fibers occurred by indentation of the hard TaC powders during the cold compaction process.

Since the mechanical properties of fiber reinforced ceramic matrix composites are largely degraded by damaged fibers, it is important to use processing techniques which will result in minimal fiber damage. The slurry infiltration process, which was applied in the processing route #2, was found to be successful in avoiding the damage of fibers during incorporation of fibers into the matrix. Another purpose of using the slurry infiltration process was to achieve uniform distribution and alignment of carbon fibers in TaC matrix. The SEM micrographs of TaC slurry infiltrated carbon fibers in Figure 47 indicate that no damage of carbon fibers occurred during the slurry infiltration process.

The scanning electron micrographs of HIP processed carbon fiber reinforced tantalum carbide matrix composite specimens are presented in Figure 48. The image in Figure 48(a) was taken in the direction perpendicular to the carbon fibers. It can be noticed that several elongated voids exist between two pre-preg tapes and some pores also exist around the fibers. This indicates that densification of the green compact of the composites was incomplete. The micrograph taken parallel to the fibers in Figure 48(b) shows that the alignment of carbon fibers is relatively uniform. At higher magnification Figure 49 it is obvious that the final density of the TaC matrix is low and that the carbon fibers are also damaged during hot isostatic pressing.

In order to clarify the reasons for the fiber damage during the HIP process, the pre-preg tapes were degassed at 500 °C for 3 hours and

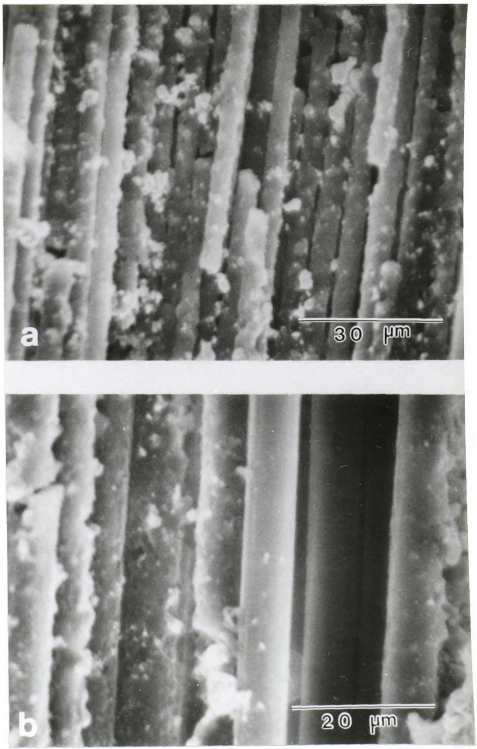

Figure 46. SEM micrographs of damaged C-fibers during cold compaction.

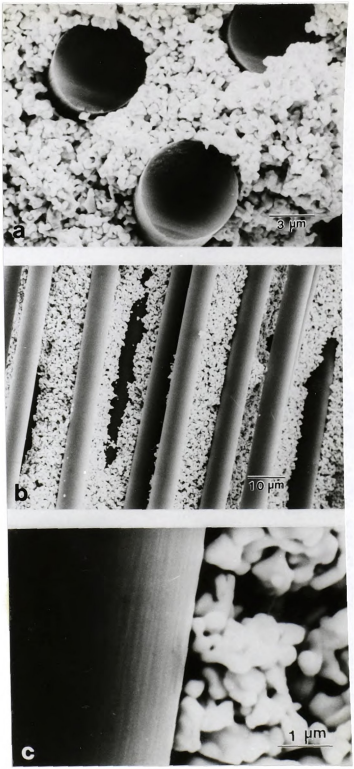

Figure 47. SEM micrographs of slurry infiltrated carbon fibers: (a) perpendicular to the fibers, (b), (c) parallel to the fibers.

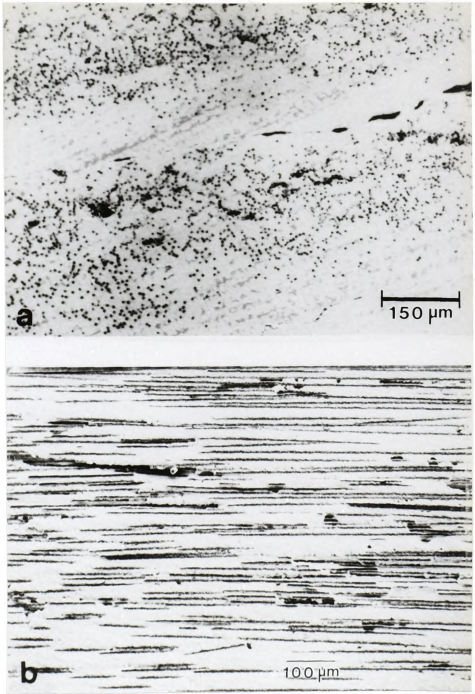

Figure 48. SEM micrographs of C-TaC composites produced by the processing route #2: (a) transverse direction to the fibers, (b) longitudinal direction to the fibers.

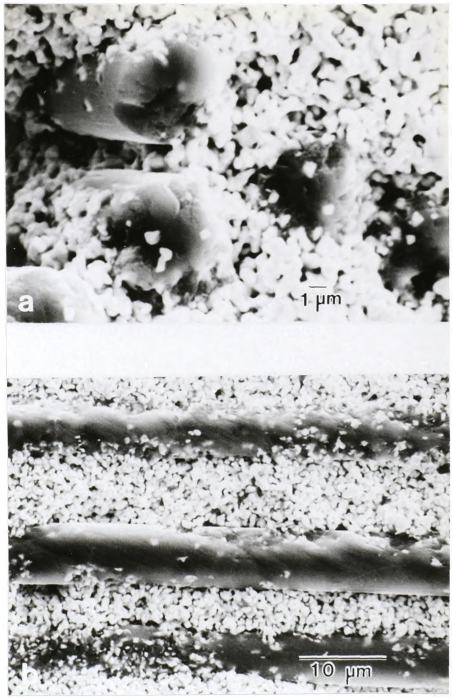

Figure 49. High magnification SEM micrographs of the specimen in Figure 12: (a) transverse direction to the fibers, (b) longitudinal direction to the fibers.

sintered at 1980 °C for 12 hours in a vacuum furnace. The sintered tapes were fractured manually and observed in a SEM. The micrographs of the sintered specimen are shown in Figure 50. Figure 50(a) shows that only a low density of matrix is obtained by sintering. As can be seen in Figure 50(b), the surface of a carbon fiber is still damaged by sintering. Since no external pressure was applied to the sintered specimens, this indentation damage of the fiber can only have occurred due to the high internal pressure developed during the high temperature sintering process.

From the above result, it is clear that the damage of carbon fibers during high temperature consolidation process can not be avoided unless a protection of carbon fibers is achieved. In order to protect the carbon fibers from the damage during processing, the fibers were sputter-coated with tantalum carbide. A tantalum carbide coated carbon fiber is shown in Figure 51. The micrographs evidence that the thickness of coating is not uniform. The result of an AES survey of a coated carbon fiber is presented in Figure 52. The Ta and C line scans in Figure 52(a) and (b) confirm that a tantalum carbide coating had formed on the carbon fiber. The exact quantitative analysis of stoichiometry of the coating was not possible by AES. However, previous experimental studies on the sputtering of tantalum carbide indicate preferential sputtering of carbon occurs [131]. Thus, it is very likely that the composition of tantalum carbide coating formed by sputter process is nonstoichiometric, with carbon being preferentially re-sputters from the fibers.

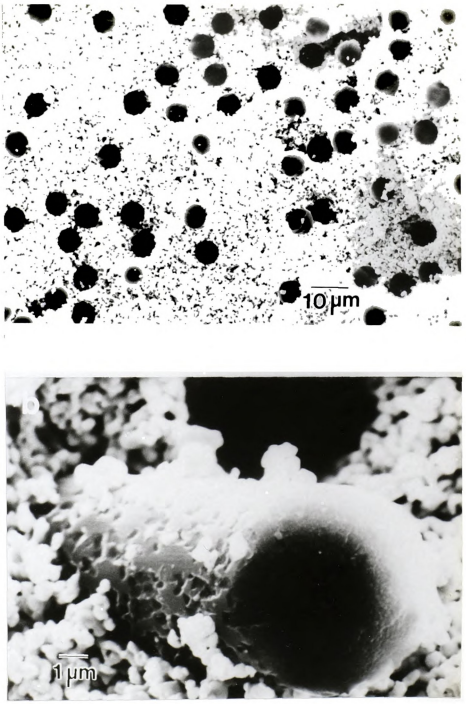

Figure 50. The SEM micrographs of the sintered and fractured pre-preg composite tape.

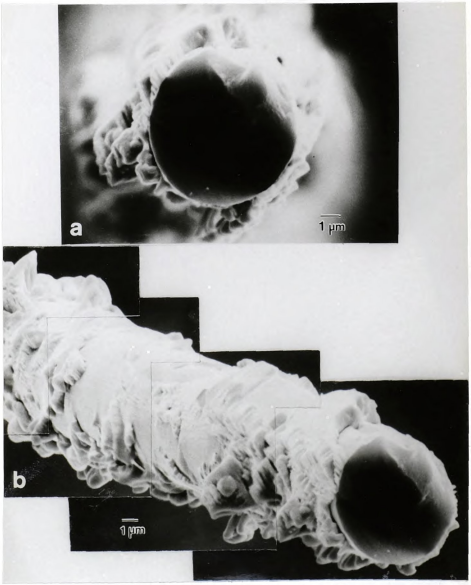

Figure 51. The SEM micrographs of a coated carbon fiber: (a) transverse direction to the fiber, (b) longitudinal direction to the fiber.

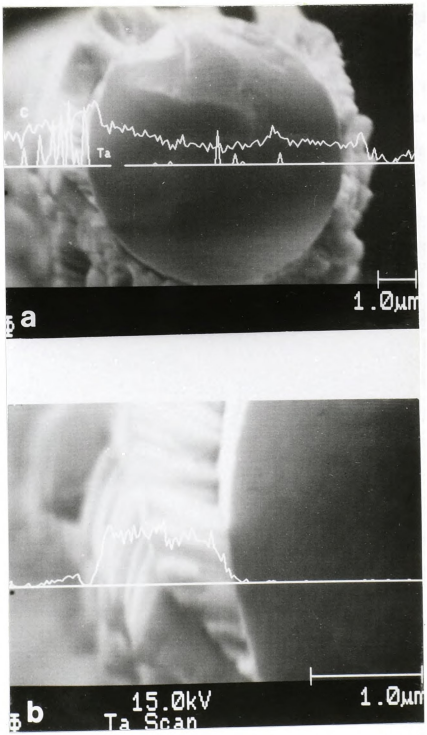

Figure 52. Ta and C line scans of the coated carbon fiber: (a) Ta and C line scan, (b) Ta line scan.

In order to see whether the coating can protect carbon fibers from the damage during high temperature processing, tantalum carbide coated carbon fibers were embedded in the tantalum carbide slurry and sintered as described before. The scanning electron micrographs of this specimen and a Ta line scan are shown in Figure 53. In Figure 53(a), it can be seen that the coating successfully protected the carbon fiber from mechanical damage. The interface of the coating and the fiber appears to have become diffuse. This might be due to the fact that the interface of the coating and the fiber became unclear by surface-polishing of the specimen. The other possible explanation is that the interfacial diffusion may have occurred between the nonstoichiometric tantalum carbide coating and the carbon fiber. The Ta line scan superimposed with a SEM micrograph in Figure 53(b) shows that the tantalum carbide coating between the fiber and the matrix exists in the specimen after high temperature sintering process.

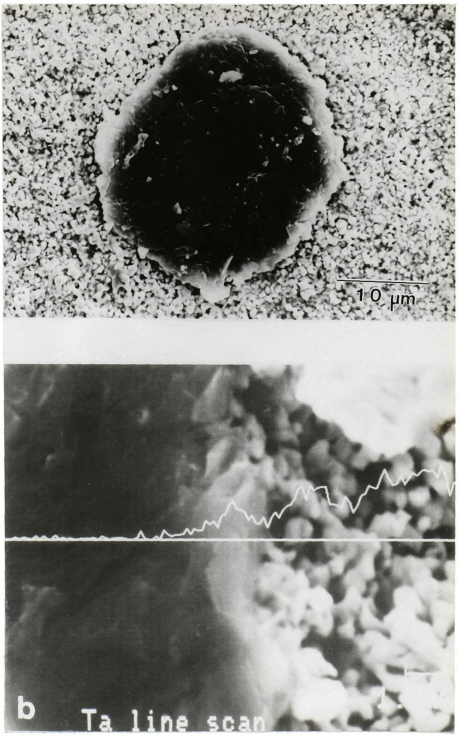

Figure 53. The SEM micrographs and a Ta line scan of sintered C-TaC composite after coating the fiber.

5.4 DISCUSSION

The carbon fiber reinforced tantalum carbide composites produced in the present study were not dense enough and free of defects to determine the mechanical properties of this composite system. However, some important information, which might be useful to successfully produce similar types of composite materials, could be found from the results of the current study. Two major problems were encountered in processing C-TaC composites. Firstly, because of its high refractoriness, the TaC matrix was very difficult to consolidate to full density. Secondly, during cold compaction and hot processing invariably mechanical damage of carbon fibers was introduced by indentation of hard tantalum carbide powders.

Hot isostatic pressing, which was employed in the present study, is capable of producing C-TaC composites with very high density if all the processing variables are correctly determined. The important variables of the HIP processing include pressure, temperature, initial density of green compacts, material for the container and geometry of the container. The main reason of low density of C-TaC composites obtained in the present investigation is considered due to the brittleness of niobium container at high temperature in the carbonaceous environment of a HIP furnace. The brittle carburized Nb container will be cracked by high gas pressure during the HIP process and the consolidation of the green compact will cease as soon as the container leaks.

The Mo shield used in the third HIP process appears to reduce the caburization of Nb containers, but it was not sufficient to prevent cracking of the containers. The first HIP processed C-TaC composite specimens using tantalum containers were found to be very dense and the containers did not show any cracks after the HIP process. Therefore, tantalum can be considered as the best material for the HIP container under the employed processing conditions. Although the hot pressing technique was not applied for the present processing, this technique may produce C-TaC composites with high density. The advantage of the hot pressing technique is that it requires less complicated preparation steps, for example the encapsulation of the specimen is not necessary.

The results of SEM and AES studies of HIP processed C-TaC composites indicate that no interfacial chemical reaction occurs between carbon fibers and stoichiometric tantalum carbide. This result is consistent with the initial theoretical prediction of compositional stability between carbon and stoichiometric tantalum carbide. The mechanical damage of carbon fibers was observed under various processing conditions. The mechanical damage of carbon fibers is most likely due to indentation of tantalum carbide powders on the surface of the carbon fibers. At room temperature the Mohs' hardness of tantalum carbide is about 9. On the other hand, the Mohs' hardness of graphite is between 0.5 and 1. Because of this large difference in the hardness values, the indentation damage of carbon fibers will occur during cold compaction and hot isostatic pressing. Further, it was also observed that the indentation damage occurred even during sintering process. Thus it can be concluded that the mechanical damage of carbon fibers during

powder processing of C-TaC composites can not be avoided unless a protection of carbon fibers is achieved.

The protection of carbon fibers can be achieved by the coating.The materials for coating should have high hardness and high melting point, and maintain the compositional and thermal stability with carbon fibers and tantalum carbide matrix at elevated temperatures. The other advantages of the coating might be that the coating can tailor the interfacial properties of any particular composite system and help to obtain uniform dispersion of reinforcing fibers. In the present study, it was found that the sputter coating of tantalum carbide on carbon fibers can prevent the mechanical damage of the carbon fiber. Other coating techniques, for example chemical vapor deposition techniques, may be used to produce a protective coatings with uniform thickness and stoichiometric composition.

5.5 SUMMARY

The results of the present study on the fabrication of carbon fiber reinforced tantalum carbide composites can be summarized as follows.

1. The carbon fiber reinforced tantalum carbide matrix composites can be successfully fabricated if some of the following considerations are taken into account.
2. No chemical reaction occurs at the interface between carbon fibers and a stoichiometric tantalum carbide matrix.
3. The damage of carbon fibers occurs by indentation of tantalum carbide powder during cold compaction and hot isostatic pressing.
4. The sintering process alone can cause indentation damage on carbon fibers probably due to the high internal pressure developed during the high temperature sintering process.
5. A tantalum carbide coating on carbon fibers prevents the indentation damage of carbon fibers.
6. A uniform protective coating of carbon fibers is necessary to fabricate C-TaC composites. The materials for coating should have high hardness and high melting point, and provide compatibility with carbon fibers and tantalum carbide matrix.

CHAPTER 6
SUMMARY AND CONCLUSIONS

The results of the current study on the deformation behavior and microstructure of $TaC_{0.99}$, and the processing of C-TaC composites are summarized as follows.

1. Extensive local plastic deformation was observed in $TaC_{0.99}$ deformed by microindentation at room temperature.

2. The dislocation structure of deformed $TaC_{0.99}$ consists almost entirely of long screw dislocations. The wavy character of screw dislocations suggests the existence of a high Peierls stress for screw dislocation motion at room temperature.

3. The lack of edge dislocations suggests that plastic deformation of $TaC_{0.99}$ at room temperature is mainly accomplished by the motion of edge dislocations, leaving long screw dislocation segments behind.

4. Screw dislocations were found to form nodes. Screw dipoles were observed to pinch off, forming dislocation loops during low temperature plastic deformation.

5. Strongly recovered microstructures and evidence of recrystallization were observed in $TaC_{0.99}$ specimens annealed after microindentation. These phenomena strongly resemble those found in metals with high stacking fault energy.

6. From the results on creep tests at intermediate temperatures (1400-1500 °C, ~ 0.4 T_m) and stresses (105-170 MPa), the values of the stress exponent (n) and activation energy (Q_c) for power-law creep of $TaC_{0.99}$ were found to be $n \approx 1.8$ and $Q_c \approx 150$ KJ/mol.

7. The low activation energy and the low stress exponent suggest that the creep of $TaC_{0.99}$ at intermediate temperatures is mainly controlled by grain boundary sliding. This is further supported by observation of void formation.

8. The observation of dislocation interaction in the crystal interior suggests that dislocation glide may act as a minor contributing mechanism during creep. TEM investigation also reveals the formation of subboundaries and dislocation networks.

9. Most dislocations formed during creep of $TaC_{0.99}$ have no preferential orientation, in contrast to dislocations formed at low temperatures. This is probably due to thermally activated dislocation motion at elevated temperatures.

10. The carbon fiber reinforced tantalum carbide matrix composites can be successfully fabricated if some of the following considerations are taken into account:

a) No chemical reaction occurs at the interface between carbon fibers and a stoichiometric tantalum carbide matrix.

b) The damage of carbon fibers occurs by indentation of tantalum carbide powder during cold compaction and hot isostatic pressing.

c) The sintering process alone can cause indentation damage on carbon fibers probably due to the high internal pressure developed during the high temperature sintering process.

d) A tantalum carbide coating on carbon fibers prevents the indentation damage of carbon fibers.

e) A uniform protective coating of carbon fibers is necessary to fabricate C-TaC composites. The materials for coating should have high hardness and high melting point, and provide compatibility with carbon fibers and tantalum carbide matrix.

LIST OF REFERENCES

LIST OF REFERENCES

1. L. E. Toth, Transition Metal Carbides and Nitrides, Academic Press, New York, (1971).

2. E. K. Storm, The Refractory Carbides, Academic Press, New York, (1967).

3. H. H. Hausner and M. G. Bowman, Fundamentals of Refractory Compounds, Plenum Press, New York, (1968).

4. W. S. Williams, "Transition-metal carbides" in Progress in solid state chemistry, Vol. 6, ed. by H. Reiss and J. O. McCaldin, Pergamon Press, New York, (1971).

5. G. E. Hollox, " Microstructure and mechanical behavior of carbides", Mat. Sci. Eng., 3, 121 (1968 / 1969).

6. A. L.Bowman, T. C. Wallace, J.L. Yarnell, R. G. Wenzel and E. K. Storms, "The crystal structures of V_2C and Ta_2C", Acta Cryst. 19, 6 (1965).

7. R. Lesser and G. Brauer, "Carbide phases of tantalum (The system tantalum-tantalum carbide)", Z. Metallkde., 49, [12], 622 (1958).

8. I. Zaplatynsky, "Observations on zeta phase in the system Ta-C", J. Amer. Cer. Soc., 49, [2], 109 (1966).

9. K. Yvon and E. Parthe, "On the crystal chemistry of the closed packed transition metal carbides, I. The structureof the ζ-V, Nb and Ta carbides", Acta Cryst. B26, 149 (1970).

10. D. J. Rowcliffe and G. Thomas, "Structure of non-stoichiometric TaC", Mat. Sci. Eng., 18, 231 (1975).

11. B. I. Markhasev, Yu. M. Shamatov and S. E. Svintsova, "Ordering in nonstoichiometric carbides of niobium and tantalum", Izv. Akad. Nauk. SSSR, Neorg. Mater., 21, 1697 (1985).

12. Ch. H. De Novion and V. Maurice, "Order and disorder in carbides and nitrides", J. Physique Colloq., 38, C7, 211 (1977).

13. J. D. Venables and M. H. Meyerhoff, "Ordering effects in NbC and TaC", Sol. Stat. Chem., Proc. of 5th Mater. Res. Symp., NBS Spec. Publ. 364, 583 (1972).

14. A. L. Bowman, "The variation of lattice parameter with carbon content of tantalum carbide", J. Phys. Chem. 65, 1596 (1961).

15. G. Santoro, "Variation of some properties of tantalum carbide with carbon content", Trans. AIME, 227, 1361 (1963).

16. J. R. Cooper and R. L. Hansler, "Variation of electrical resistivity of cubic tantalum carbide with composition", J. Chem. Phys., 39, [1], 248 (1963).

17. R. Steinitz and R. Resnick, "Electrical and magnetic properties of compositions in the tantalum-carbon system", J. Appl. Phys., 37, 3463 (1966).

18. H. L. Brown, P. E. Armstrong and C. P. Kempter, "Elastic properties of some polycrystalline transition-metal monocarbides", J. Chem. Phys., 45, [2], 547 (1966).

19. J. H. Westbrook and E. R. Stover, "Carbides for high temperature applications" in High temperature technology, ed. by I. E. Campbell and Sherwood, Wiley, New York (1967).

20. G. V. Samsonov, M. S. Kovalchenko, V. V. Dzmelinskii and G. S. Upadayaya, "Temperature dependence of hardness of titanium carbide in the homogeneity range", Phys. Stat. Sol. (a), 1, 327 (1970).

21. J. H. Westbrook, "Note on the temperature dependence of hardness of the transition metal monocarbides", Acta Met., 3, 104 (1955).

22. W. S. Williams, "Influence of temperature, strain rate, surface condition, and composition on the plasticity of transition-metal carbide crystals", J. Appl. Phys., 35, 1329 (1964).

23. R. Steinitz, "Mechanical properties of refractory carbides at high temperatures", in Proc. of Conf. on Nuclear Application of Nonfissionable Ceramics, American Nuclear Society (1966).

24. D. J. Rowcliffe and W. J. Warren, "Structure and properties of tantalum carbide crystals", J. Mat. Sci., 5, 345 (1970).

25. D. J. Rowcliffe and G. H. Hollox, "Hardness anisotropy, deformation mechanisms and brittle-to-ductile transition in carbides", J. Mat. Sci., 6, 1270 (1971).

26. C. A. Brookes, J. B. O'Niel and B. A. W. Redfern, "Anisotropy in the hardness of single crystals", Proc. Roy. Soc. Lond. A, 322, 73 (1971).

27. R. H. J. Hannink, D. L. Kohlstedt and M. J. Murray, "Slip system determination in cubic carbides by hardness anisotropy", Proc. Roy. Soc. Lond. A, 326, 409 (1972).

28. D. J. Rowcliffe and G. E. Hollox, "Plastic flow and fracture of tantalum carbide and hafnium carbide at low temperatures", J. Mat. Sci., 6, 1261 (1971).

29. G. Morgan and M. H. Lewis, "Hardness anisotropy in niobium carbide", J. Mat. Sci., 9, 349 (1974).

30. D. J. Rowcliffe, "Plastic deformation of transition metal carbides" in Deformation of ceramic materials II, ed. by R. E. Tressler and R. C. Bradt, Materials Science Research, Vol. 18, 49 (1983).

31. A. Kelly and D. J. Rowcliffe, "Slip in titanium carbide", Phys. Stat. Sol., 14, K29 (1966).

32. H. Kurishita, K. Nakajima and H. Yoshinaga, "The high temperature deformation mechanism in titanium carbide single crystals", Mater. Sci. Eng., 54, 177 (1982).

33. R. Darolia and T. F. Archbold, "Plastic deformation of polycrystalline zirconium carbide", J. Mat. Sci., 11, 283 (1976).

34. D. W. Lee and J. S. Haggerty, "Plasticity and creep in single crystals of zirconium carbide", J. Amer. Cer. Soc., 52, [12], 641 (1969).

35. P. F. Becher, "Mechanical behavior of polycrystalline TaC", J. Mat. Sci., 6, 79 (1971).

36. J. L. Martin, P. Lacour-Gayet and P. Costa, "Plastic deformation of tantalum carbide up to 2200 °C" in Electron microscopy and structure of materials" ed. by G. Thomas, R. M. Fulrath and R. M. Fisher, University of California Press, Berkeley (1972).

37. G. Das, K. S. Mazdiyasmi and H. A. Lipsitt, "Mechanical properties of polycrystalline TiC", J. Amer. Cer. Soc., 65, 104 (1982).

38. W. S. Williams and R. D. Schaal, "Elastic deformation, plastic flow and dislocations in single crystals of titanium carbide", J. Appl. Phys., 33, 955 (1962).

39. G. E. Hollox and R. E. Smallman, "Plastic behavior of titanium carbide", J. Appl. Phys., 37, 818 (1966).

40. D. K. Chatterjee, M. G. Mendiratta and H. A. Lipsitt, "Deformation behavior of single crystals of titanium carbides", J. Mater. Sci., 14, 2151 (1970).

41. A. Kelly and D. J. Rowcliffe, "Deformation of polycrystalline transition metal carbides", J. Amer. Cer. Soc., 50, 253 (1967).

42. W. S. Williams, "Dispersion hardening of titanium carbide by boron doping", Trans. AIME, 236, 211 (1966).

43. J. D. Venables, "The nature of precipitates in boron-doped TiC", Phil. Mag., 16, 873 (1967).

44. J. D. Venables, D. Kahn and R. G. Lye, "Structure of the ordered compound V_6C_5", Phil. Mag., 18, 177 (1968)

45. H. A. Johansen and J. G. Clearly, "The ductile-brittle transition in tantalum carbide", J. Electr. Chem. Soc., 113, [4], 378 (1968).

46. G. E. Hollox, "Plastic deformation of carbides", NBS Spec. Publ. 303, 201 (1968).

47. J. L. Martin, "Evidence of dislocation dissociation in nearly stoichiometric tantalum carbide using the weak-beam technique", J. Micros., 98, 209 (1973).

48. C. Allison, M. Hoffman and W. S. Williams, "Electron energy loss spectroscopy of carbon in dissociated dislocations in tantalum carbide", J. Appl. Phys. 53, 6757 (1982).

49. J. E. Bird, A. K. Mukherjee and J. E. Dorn, "Correlations between high-temperature creep behavior and structure" in Quantitative relation between properties and microstructure, ed. by D. G. Brandon and A. Rosen, Israel University Press, Jerusalem (1969)

50. W. D. Nix and B. Illschner, "Mechanisms controlling creep of single phase metals and alloys", in Strength of metals and alloys vol. 3, ed. by P. Haasen, V. Gerold and G. Kostorz, Pergamon Press Inc., New York (1979).

51. T. H. Hazlett and R. D. Hansen, "Influence of substructure on the shape of the creep curve", Trans. AIME, 47, 508 (1955).

52. J. Weertman and J. R. Weertman, "Mechanical properties, strongly temperature-dependent" in Physical metallurgy part2, ed. by R. W. Cahn and P. Hassen, North-Holland Physics Publishing, Amsterdam (1983).

53. O. D. Sherby, J. L. Lytton and J. E. Dorn, "Activation energy for creep of high-purity aluminium", Acta Met., 5, 217 (1957).

54. A. K. Mukherjee, J. E. Bird and J. E. Dorn, "Experimental correlations for high-temperature creep", Trans. A.S.M., 62, 155 (1969).

55. O. D.Sherby and P. M. Burke, "Mechanical behavior of crystalline solids at elevated temperatures", Progress in Mat. Sci. 13, 325 (1967).

56. W. R. Cannon and T. G. Langdon, "Creep of ceramics", (a) Part1. Mechanical characteristics, J. Mat. Sci., 18, 1 (1983): (b) Part2. An examination of flow mechanisms, J. Mat. Sci., 23,1 (1988).

57. J. Bardeen and C. Herring, "Diffusion in alloys and kirkendall effect", in Imperfections in nearly perfect crystals", ed. by W. Schockley, J. Hollomon, R. Maurer and F. Seitz, John Wiley and Sons Inc., New York (1952).

58. J. Weertman, "Steady-state creep of crystals", J. Appl. Phys., 28, 1185 (1957).

59. J. P. Poirier, Creep of Crystals, Cambridge University Press, Cambridge (1985).

60. J. Weertman, "Dislocation climb theory of steady-state creep", Trans. A.S.M., 61, 681 (1968).

61. J. Harper and J. E. Dorn, "Viscous creep of aluminium near its melting temperature", Acta Met., 5, 654 (1957).

62. P. Yavari, D. A. Miller and T. G. Langdon, "An investigation of Harper-Dorn creep-I. Mechanical and microstructural characteristics", Acta Met., 30, 871 (1982).

63. P. J. Dixon-Stubbs and B. Wilshire, "Deformation processes during creep of single and polycrystalline CaO", Phil. Mag. A, 45, 519 (1982).

64. T. G. Langdon and P. Yavari, "An investigation of Harper-Dorn creep-II. Flow process", Acta Met., 30, 881 (1982).

65. F. A. Mohamed and T. J. Ginter, "On the nature and origin of Harper-Dorn creep", Acta Met., 30, 1869 (1982).

66. H. Luthy, A. K. Miller and O. D. Sherby, "The stress and temperature dependence of steady-state flow at intermediate temperatures for pure polycrystalline aluminium", Acta Met., 28, 169 (1980).

67. F. R. N. Nabarro, "Deformation of crystals by the motion of single ions", Report of a conference on strength of solids, The Physical Soc., 75 (1948).

68. C. Herring, "Diffusional viscosity of a polycrystalline solid", J. Appl. Phys., 21, 437 (1950).

69. R. L. Coble, "A model for boundary diffusion controlled creep in polycrystalline materials", J. Appl. Phys., 34, 1679 (1963).

70. B. J. Hockey, "Use of the hardness test in the study of the plastic deformation of single crystals" in The science of hardness testing and its research applications, ed. by J. H. Westbrook and H. Conrad, ASM, Ohio (1973).

71. D. Tabor, "The hardness of solids", Rev. Phys. Tech., 1, 145 (1970).

72. V. G. Eremenko and V. I. Nikitenko, "Electron microscope investigation of the microplastic deformation of silicon by indentation", Phys. Stat. Sol. (a), 14, 317 (1972).

73. M. J. Hill and D. J. Rowcliffe, "Deformation of silicon at low temperatures", J. Mat. Sci., 9, 1569 (1974).

74. B. J. Hockey, "Plastic deformation of aluminum oxide by indentation and abrasion", J. Amer. Cer. Soc., 54,[5], 223 (1971).

75. "Standard test method for density of glass by buoyancy", ASTM standard designation: C 693-84, Annual book of ASTM standards, Vol. 15.02, 218 (1989).

76. P. Hirsch, A. Howie, R. B. Nicholson, D. W. Pashley and M. J. Whealan, "Electron microscopy of thin crystals", Robert E. Krieger Publishing Co., Florida (1977).

77. C. H. Hsueh, A. G. Evans and R. L. Coble, "Microstructure development during final/intermediate state sintering- I. Pore/grain boundary separation" Acta Met., 30, 1269 (1982).

78. M. V. Heimendahl, Electron microscopy of materials, Academic Press, New York, p. 137 (1980).

79. R. Hill, The mathematical theory of plasticity, Oxford University Press, London (1950).

80. L. E. Samuels and T. O. Mulhearn, "An experimental investigation of the deformed zone associated with indentation hardness impressions", J. Mech. Phys. Solids, 5, 125 (1957).

81. D. M. Marsh, "Plastic flow in glass", Proc. Roy. Soc. A, 279, 420 (1964).

82. D. Tabor, The hardness of metals, Oxford University Press, London (1951).

83. K. L. Johnson, "The correlation of indentation experiments", J. Mech. Phys. Solids, 18, 115 (1970).

84. R. Peierls, "The size of a dislocation", Proc. Phys. Soc. London, A52, 34 (1940).

85. F. R. N. Nabarro, "Dislocations in a simple cubic lattice", Proc. Phys. Soc. London, A59, 256 (1947)

86. R. A. Foxall and C. D. Statham, "Dislocation arrangements in deformed single crystals of niobium-molybdenum alloys and niobium-9 at% rhenium", Acta Met., 18, 1147 (1970).

87. F. Louchet, L. P. Kubin and D. Versely, "In situ deformation of b.c.c. crystals at low temperatures in a high-voltage electron microscope Dislocation mechanisms and strain-rate equation, Phil. Mag. A, 39, [4], 433 (1979).

88. H. Saka, K. Noda and T. Imura, "Tensile test of foil specimens of iron single crystals at room and low temperatures under observation in high voltage electron microscope", Crystal Lattice Defects, 4, 45 (1973).

89. V. Vitek, "Effect of dislocation core structure on the plastic properties of metallic materials" in Dislocations and properties of real materials, ed. by M. H. Loretto, The Institute of Metals, London (1985),p. 30.

90. É. Y. Gutmanas, É. M. Nadgornyi and A. V. Stepanov, "Dislocation movement in sodium chloride crystals", Soviet Physics-Solid State, 5, [4], 743 (1963).

91. J. Friedel, Dislocations, Pergamon Press, Oxford (1964).

92. R. W. Cahn, "Recovery and recrystallization" in Physical metallurgy part2, ed. by R. W. Cahn and P. Hassen, North-Holland Physics Publishing, Amsterdam (1983).

93. S. Chevacharoenkul, "Kinetics and mechanisms of intermediate and high-temperature creep in niobium carbide single crystals", Ph. D. thesis, North Carolina State University, Raleigh, NC, (1987).

94. F. Keihn and R. Kebler, "High-temperature ductility of large-grained TiC", J. Less-Common Metals, 6, 484 (1964).

95. I. I. Spivak, R. A. Andrievskii, V. N. Rystsov, and V. V. Klimenko, "Creep of titanium monocarbide in its homogeneity range", Poroshkovaya Met., 139,[7], 69 (1974)

96. J. Chermant, G. Leclerc and B. L. Mordike, "Deformation of titanium carbide at high temperatures", Z. Metallkde, 71, 465 (1980).

97. M. H. Leipold and T. H. Nielson, "Mechanical properties of hot-pressed zirconium carbide tested to 2600 °C", J. Amer. Cer. Soc., 47, [9], 419 (1964).

98. D. W. Lee and J. S. Haggerty, "Plasticity and creep in single crystals of zirconium carbide", J. Amer. Cer. Soc., 52, [12], 641 (1969).

99. L. N. Dement'yev, P. V. Zubarev, V. N. Kruglov, V. N. Turchin and YE. D. Kharkhadin, "High-temperature creep of monocrystalline niobium carbide", Phys. Met. Metall., 46,[3], 142 (1978).

100. R. D. Nixon, S. Chevacharoenkul and R. F. Davis, "Steady-state creep behavior of hot isostatically pressed niobium carbide", Mat. Res. Bull., 22, 1233 (1987).

101. S. Chevacharoenkul and R. F. Davis, "Dislocation mechanisms, diffusional processes and creep behavior in NbC_x", Acta Met., 37, 417 (1989).

102. R. Resnick, R. Steinitz and L. Seigle, "Determination of diffusivity of carbon in tantalum and columbium carbides by layer-growth measurements", Trans. AIME, 233, 1915 (1965).

103. R. A. Andriyevskiy, V. V. Klimenko and Yu. F. Khromov, "Carbon self-diffusion in carbides of IV and V transition metals", Fiz. Metal.Metalloved., 28, [2], 293 (1969).

104. R. D. Gifkins, "A mechanism for the formation of intergranular cracks when boundary sliding occurs", Acta Met., 4, 98 (1956).

105. C. W. Chen and E. S. Machlin, "On the mechanism of intercrystalline cracking", Acta Met., 4, 655 (1956).

106. H. C. Chang and N. J. Grant, "Mechanism of intercrystalline fracture", Trans. AIME, 206, 544 (1956).

107. E. M. Passmore, R. H. Duff and T. Vasilos, "creep of dense polycrystalline magnesium oxide", J. Amer. Cer. Soc., 49, [11], 594 (1966).

108. S. U. Din and P. S. Nicholson, "Creep of hot-pressed silicon nitride", J. Mat. Sci., 10, 1375 (1975).

109. L. E. Poteat and C. S. Yust, "Creep of polycrystalline Thorium dioxide", J. Amer. Cer. Soc., 49, [8], 410 (1966)

110. T. G. Langdon and R. B. Vastava, "An evaluation of deformation models for grain boundary sliding" in Mechanical testing for deformation model development, ed. by R. W. Rohde and J. C. Swearengen, ASTM STP no. 765, 435 (1982).

111. G. C. Wei and P. F. Becher, "Development of SiC-whisker-reinforced ceramics", Amer. Ceram. Soc. Bull., 64, 298 (1983).

112. R. A. J. Sambell, A. Briggs, D. C. Phillips and D. H. Bowen, "Carbon fibre composites with ceramic and glass matrices", J. Mat. Sci., 7, 676 (1972).

113. J. F. Bacon, K. M. Prewo and E. R. Thompson, "Research on graphite reinforced glass matrix composites", NASA Contract Report 158946 (1978).

114. K. M. Prewo and J. J. Brennan, "High-strength silicon carbide fiber-reinforced glass-matrix composites", J. Mat. Sci., 15, 463 (1980).

115. R. W. Rice, "Mechanisms of toughening in ceramic matrix composites", Ceram. Eng. Sci. Proc., 2 [7-8], 661 (1981).

116. D. C. Phillips, "Fibre reinforced ceramics" in Fabrication of composites, ed. by A. Kelly and S. T. Mileiko, Elservier Science Publishers, (1983) P 373.

117. J. A. Cornie, Y. M. Chiang, D.R. Uhlmann, A. Mortensen and J. M. Collins, "Processing of metal and ceramic matrix composites, Amer. Ceram. Soc. Bull., 65, 293 (1986).

118. R. W. Rice, "Ceramic composites-Processing challenges", Ceram. Eng. Sci. Proc., 2 [7-8], 493 (1981).

119. R. A. J. Sambell, "The technology of ceramic-fibre ceramic-matrix composites, Composites, September, 276 (1970).

120. E. S. Hodge, "Hot isostatic pressing improves powder metallurgy parts", Mater. Des. Eng., 61, 92 (1965).

121. P. E. Price and S. P. Kohler, "Hot isostatic pressing", in Powder metallurgy, Metals Handbook 9th ed. Vol 7, American Society for Metals, (1984), P 419.

122. T. Fujikawa, "Hot isostatic pressing(HIP) of ceramics and HIP equipment for ceramics", in Fine ceramics, ed. by S. Sato, Elservier Science Publisher, (1988).

123. L. Björk and L. A. G. Hermannsson, "Hot isostatically pressed alumina-silicon carbide whisker composites", J. Am. Ceram. Soc., 72 [8], 1439 (1989).

124. G. Pezzotti, I. Tanaka, T. Okamoto, M. Kozumi and Y. Miyamoto, "Processing and mechanical properties of dense Si_3N_4-SiC-whisker composites without sintering aids", J. Am. Ceram. Soc., 72 [8], 1461 (1989).

125. A. J. Caputo and W. J. Lackey, "Fabrication of fiber-reinforced ceramic composites by chemical vapor infiltration", Ceram. Eng. Sci. Proc., 5 [7-8], 654 (1984).

126. B. Capdepuy and P. Lespade, "Study of ceramic-fibre/ ceramic-sol-gel based matrix composites", in Technical ceramics, ed. by H. Nosbusch and I. V. Mitchell, Elservier (1986) P 233.

127. J. O. Gibson, R. L. Schumacher and K. L. Myler, U. S. Patent 3 736 159, May 29 (1973).

128. J. O. Gibson, R. L. Schumacher and K. L. Myler, U. S. Patent 3 776 000, October 16 (1973).

129. J. O. Gibson and M. G. Gibson, U. S. Patent 4 196 230, April 1 (1980).

130. J. B. Donnet and R. C. Bansal, Carbon fibers, Marcel Dekker, Inc. (1984) P 27.

131. G. Betz and G. K. Wehner, "Sputtering of multi component materials", in Sputtering by particle bombardment II, ed. by R. Behrisch, Springer-Verlag (1983).

MICHIGAN STATE UNIV. LIBRARIES
31293008857116